ELSEVIER

Contents lists available at ScienceDirect

Coordination Chemistry Reviews

journal homepage: www.elsevier.com/locate/ccr



Review

Metal-organic frameworks and their derivatives for electrically-transduced gas sensors



Ming-Shui Yao a,b, Wen-Hua Li a, Gang Xu a,c,*

- ^a State Key Laboratory of Structural Chemistry, Fujian Institute of Research on the Structure of Matter, Chinese Academy of Sciences, Fuzhou, Fujian 350002, China ^b Institute for Integrated Cell-Material Sciences (WPI-iCeMS), Kyoto University Institute for Advanced Study, Kyoto University, Yoshida Ushinomiya-cho, Sakyo-ku, Kyoto
- ^cUniversity of Chinese Academy of Sciences, Chinese Academy of Sciences, Beijing 100039, China

ARTICLE INFO

Article history: Received 19 May 2020 Received in revised form 2 July 2020 Accepted 8 July 2020 Available online 7 September 2020

Keywords:
Metal-organic frameworks
Conductive coordination polymer
Metal-organic frameworks derivatives
Electrical device
Gas sensors

ABSTRACT

Metal-organic frameworks (MOFs) and the MOF derived materials are porous solid materials with broad application prospect. As for electrically-transduced gas sensors, the application barrier of the signal transducer has been overcome by development in fields of conductive MOFs, the MOF based composites, dynamic MOFs, and/or the MOF derived materials. Currently, it is moving towards a critical development stage from usability to ease of use, of which great challenge remains unsolved. To address this issue, we give our perspective on the basic principles, material design, sensor performances, and worthwhile directions based on recently published works, focusing on five primary types of electrically-transduced gas sensors (chemiresistors, field-effect transistors (FETs), electrochemical gas sensors, chemical diodes, and chemicapacitors).

© 2020 Published by Elsevier B.V.

Contents

1.	Intro	duction .		
2.			principles of electrically-transduced gas sensors	
۷.	2.1.		ion	
	2.2.		ensing principles	
	2.2.	2.2.1.	Basic components of electrically-transduced gas sensors	
		2.2.1.	Basic sensing performance parameters	
		2.2.2.	Basic sensing mechanisms	
_	3.6	2.2.4.	Typical examples of different types of electrically-transduced gas sensors	
3.			c frameworks (MOFs) and their derivatives for chemiresistive gas sensors	
	3.1.		as active materials for chemiresistive gas sensors	
		3.1.1.	Neat MOFs for moderate temperature chemiresistive gas sensing	
		3.1.2.	Neat MOFs for room temperature chemiresistive gas sensing	13
		3.1.3.	MOF-on-MOFs for chemiresistive gas sensing	17
	3.2.	MOFs a	as functional materials in composites for chemiresistive gas sensors	18
		3.2.1.	MOFs-polymer or MOFs-organic molecule composites	18
		3.2.2.	MOFs-metals composites	19
		3.2.3.	MOFs-carbon composites.	20
		3.2.4.	MOFs-metal oxides composites	20
	3.3.	MOFs	derived materials for chemiresistive gas sensors	
		3.3.1.	MOx and their composites.	
		3.3.2.	Carbon materials and their composites.	

E-mail address: gxu@fjirsm.ac.cn (G. Xu).

^{*} Corresponding author at: State Key Laboratory of Structural Chemistry, Fujian Institute of Research on the Structure of Matter, Chinese Academy of Sciences, Fuzhou, Fujian 350002, China.

4.	Metal-organic frameworks (MOFs) for field-effect transistor (FET) gas sensors	. 25
5.	MOFs and their derivatives for chemical diodes type gas sensors	. 26
	5.1. MOFs for chemical diodes type gas sensors	. 26
6.	MOFs and their derivatives for electrochemical gas sensors	. 28
7.	MOFs and their derivatives for capacitive type gas sensors	. 29
8.	Conclusions and outlook	. 30
	Declaration of Competing Interest	. 30
	Acknowledgments	. 30
	References	. 31

1. Introduction

Sensing is the art of seeing things invisible [1]. Because of simplicity and compatibility with standard electronic technologies, electrically-transduced gas sensors help human beings collect chemical or physical information on gas analytes, and produce signals that can be efficiently acquired, processed, stored, and analyzed [2–8]. To realize next-generation transformation in electrically-transduced gas sensors, conductive/capacitive materials with ultra-sensitivity toward physical and chemical stimuli generated by gaseous analytes, as well as feasible techniques for their integration into sensing devices, are urgently needed to be developed.

Metal-organic frameworks (MOFs), also well-known porous coordination polymers (PCPs), are crystalline polymeric microporous inorganic-organic hybrid materials composed of inorganic nodes bridged by organic ligands [9-13]. Since the successful preparation of MOFs/PCPs with permeant porosity reported in the late 1990s [14,15], they have been utilized and studied for a wide range of potential applications, such as gas storage and separation [16-20], chemical sensors [21-28], catalysis [29-31], and drug release [32], owing to the ultra-high porosity and framework tunability. Especially, the ultra-high surface areas, tunable electronic structures, and gas adsorption/separation capability of conductivity or permittivity (dielectric constant) sensitive MOFs and the MOF based composites are well matched with requirements for new generation electrically-transduced gas sensors mentioned above. In the early stage of MOFs based chemical gas sensors, optical and mass transducer sensors are the emphasis of research in this area [33-36]. The electrically-transduced gas sensors have received little attention until recently, with the boosting developments in fields of ion/proton conductive MOFs (IC/PC-MOFs) [37– 40], electronically conductive MOFs (electrically conductive MOFs, EC-MOFs) [39,41-44], the MOF based composites [45-50], as well as dynamic states and more fundamental understanding of MOFs [20,51–54]. Although such an area is rather new, great achievements in both material design and device integration have been gained, revealing the great potential of MOFs applied to high performance electrically-transduced gas sensors [3,55-58].

Alternatively, MOFs are also ideal precursor materials, and high-performance MOF derived sensing materials such as metals, metal compounds, carbon materials, or their composites, have also been extensively studied [59–63]. These MOF-derived materials exhibited remarkable advantages toward application in electrically-transduced gas sensors owing to their high porosity and chemical tunability originating from MOF precursors [64,65].

Researches on MOFs and their derivatives based electrically-transduced gas sensors are now entering a critical development stage from usability to ease of use, while great challenges of materials design and device integration remain unsolved. This calls for a comprehensive overview and outlook based on the latest related literature. Despite a number of reviews on sensing devices (e.g. MOFs chemical sensors [5,34,66], MOFs for chemiresistive gas sensors [2,3,67]), and active materials (e.g. conductive MOFs

[37,42,55]), a review on MOFs and the MOF derived materials based electrically-transduced gas sensors is not yet reported. In this review, firstly, we describe the basic sensing principles of electrically-transduced gas sensors. Then, with respect to the materials design and sensing performances, the progress on MOFs and the MOF derived materials based chemiresistors, field-effect transistors (FETs), electrochemical gas sensors, chemical diodes and chemicapacitor gas sensors are reviewed based on the available literature. Finally, we summarize main achievements and propose an encouraging outlook with worthwhile directions that remain to be pursued in terms of both materials design and device integration.

2. Basic sensing principles of electrically-transduced gas sensors

As mentioned in aforementioned part, the significance of the MOF and the MOF derived materials has boosted the development of plenty of different approaches for applying them as electrically-transduced gas sensors. The electrically-transduced gas sensors based on MOF and MOF derived materials are classified into five categories (Fig. 1) and are discussed in this section with representative examples.

2.1. Definition

According to the recommendations of International Union of Pure and Applied Chemistry (IUPAC), the definition of MOF materials is a coordination network (framework) with organic ligands containing potential voids [68]. Typically, MOF can be described by the crystalline framework constructed by the coordination of functional organic ligands with metal sites (complex metal sites also called as second building units, SBUs). The topology, channel shape, functionality of ligands/metal sites, coordination bonds can be rationally designed, and thus tuning the gas diffusion/adsorption capability, catalytic ability, and electrical properties of

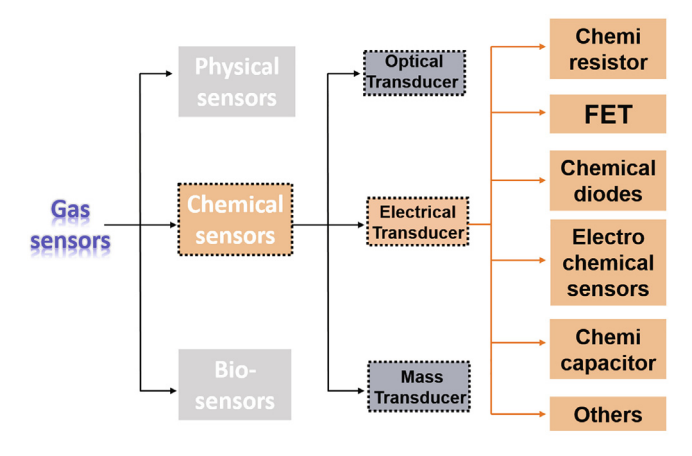


Fig. 1. The category of electrically-transduced gas sensors.

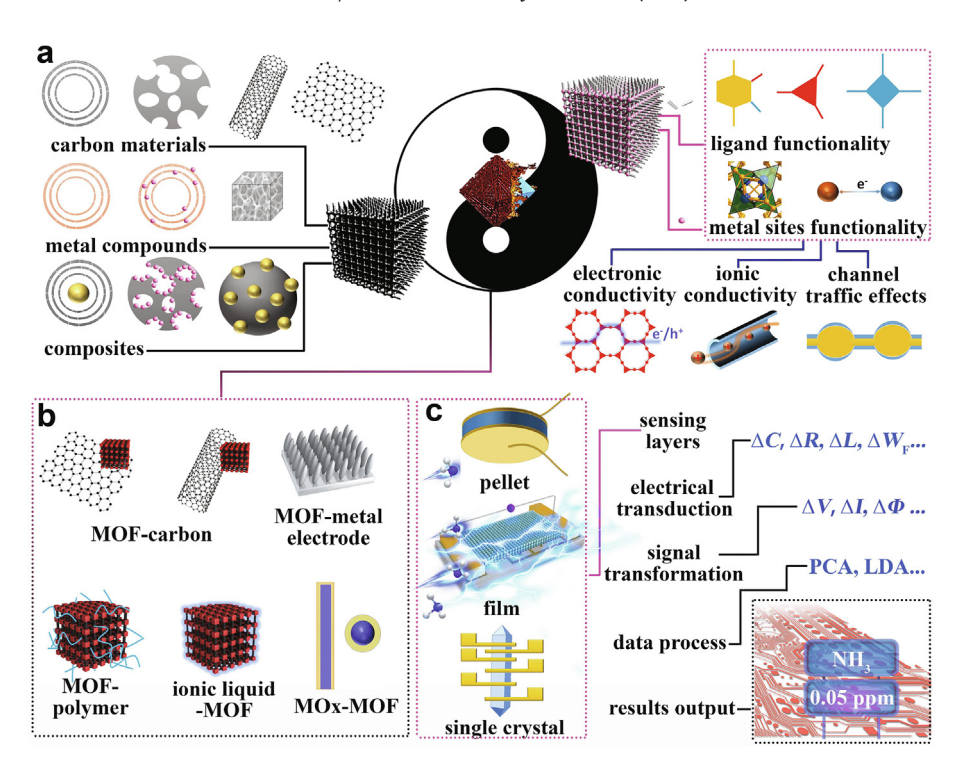


Fig. 2. (a) MOF and MOF derived materials, (b) MOF based composites, and (c) the gas sensing processes: gas diffusion, sensing layers (pellet, film, single crystal), electrical transduction (C is capacitance, C is inductance, and C is resistance C, work function C0, signal transformation (C1 refers current, C2 refers voltage, C3 refers electrical potential, and the measurable changes in capacitance presented in magnitude, frequency (C4), and phase (C4), data process (PCA, LDA, C4.), and result outputs (type of gas, concentration).

the final MOF (the right part of Fig. 2a). Based on this, the controlled transformation conditions can further modulate the composition, phase, porosity and electrical properties of MOF derived materials, such as carbon materials (e.g. amorphous carbon, carbon nanotubes (CNTs), graphene (G)), metal compounds (e.g. metal oxides (MOxs), metal sulfides (MSs)), composites (e.g. metal/carbon, MOx/carbon, MS/carbon, noble metal (NM)/MOx), and so on (the left part of Fig. 2a).

Different from gas sensors with optical or mass transducer, electrically-transduced gas sensors normally required semiconductive/conductive ability or other sensitive electrical properties of the active materials [2,8]. Limited by the insulating nature of most developed MOFs, they usually need to mix with a second material, named the MOF based composites (Fig. 2b), to combine advantages of both to meet the requirements of practical applications. Such composites include but not limited to MOF-carbon, MOF-metal electrode, MOF-polymer, MOF-ionic liquids (ILs), MOF-MOx, and MOF-on-MOFs.

The "Cambridge definition" of chemical sensors is copied as follows: Chemical sensors are miniaturised devices that can deliver real time and on-line information on the presence of specific compounds or ions in even complex samples [69,70]. Generally, a chemical sensor consists of both a chemical recognition element and a transducing element, which are able to combined to detect the chemical environmental changes and transform them to a readable signal [2,71]. Since this review focuses on gaseous detection and the electrical transducer, sensors for non-gaseous detection, as well as those based on optical/mass transducers will be excluded.

2.2. Basic sensing principles

2.2.1. Basic components of electrically-transduced gas sensors

As shown in Fig. 2c, basic components of electrically-transduced gas sensors include sensing layer, electrical transduction, signal transformation, the data process and result output.

The sensing layer incorporates three types: the powder pellet, the thin/thick film, and the single crystal.

In the recognition process, the sensing layer composed of active materials or their composites interacts with gaseous analytes, resulting in electrical parameter changes of the sensing material. The electrical parameters include electrical conductivity (σ) /resistivity (ρ) , the permittivity (ε) , the dielectric constant), and the work function (ϕ) , which are then converted by the electrical transducer into a measurable electrical signal, including the current (I), the voltage (V), electrical potential (E), resistance (R)/impedance (Z), or capacitance (C). These signals subsequently undergo data processing, including amplification, filtering, principle component analysis (PCA), and linear discriminant analysis (LDA), etc. After this, the output results, containing information about the identity of the analytes as well as their concentration, can be displayed on a specific screen (wired or wireless connection), saved as files and exchanged with the analysis center (if available) [72].

2.2.1.1. Sensing layers. Electrical properties of the sensing layers strongly rely on the composition and architecture of active materials and their composites, since they are directly connected with all three gas sensing processes: the gas diffusion/molecule capture unit, the surface/bulk reaction unit (the material-analyte interactions), and the transport of electrical parameter change unit.

For the gas diffusion/molecule capture unit, the sensing layers are required to possess diffusion-facilitated pathways and high accessible surface areas. Gas diffusion in macro-, meso- and micro-pores remarkably differ from each other [73–78]. In practical cases, pore distributions are more complicated because many of them cover pores ranging from micro-pores to macro-pores. Considering the capability of the mixed pore networks to modulate the channel traffic effects, the gas diffusion inside the pores of the sensing layers can be sensitively and selectively controlled.

For the surface/bulk reaction unit (the material-analyte interactions), abundant active sites of active materials for interactions

with gas molecules are expected, which require not only high surface areas but also high-density active sites on exposed surface areas. The additional catalytic effects brought by doping or catalyst loading can further enhance the efficiency of the sensing reaction.

In terms of the transport of the electrical parameter change unit, the high-quality connected network of the active materials is required. In this respect, the high-quality single crystal seems to be the best choice. However, slow mass transport resulting from the kinetic issues of gas diffusion in pores of the porous single crystal, or small surface areas of the non-porous single crystal should be considered, both of which will offset benefits or even degrade the whole sensing performances.

Therefore, in practical cases, researchers need to consider the overall effects of positive and negative factors. Owing to a balance on all sensing processes, high-quality thin films constructed by well inter-connected nanocrystals with the thickness in nanometer scale normally show overall optimal effects.

2.2.1.2. Electrical transducers. Electrical transducers convert sensing changes into electrical signals by integrating sensing active materials with electrodes that can be either two-/three-/four-probes or interdigital electrodes (IDEs) by conductive paste coating, sputtering, thermal evaporation or photolithography to form electrical devices. Normally insulating substrates like polycrystalline Al₂O₃, Si/SiO₂, glass, sapphire, and polymers will be utilized. In some specific cases (e.g. chemical diodes), conducting or semiconducting substrates will be adopted. More details will be discussed with reported works in the following sections.

The electrical parameters sensitively affected by gaseous analytes include electrical conductivity (σ) /resistivity (ρ) , the work function (ϕ) , and permittivity (ε) , the dielectric constant). For better understanding of them, basic definitions are briefly provided as follows.

The electrical conductivity (σ) /resistivity (ρ) can be divided into two sorts, namely electronic conductivity (EC) and ionic conductivity (IC). For electronic conductivity, both the charge carrier mobility (μ) and density (n) of electrons (e) and holes (h) contribute to its value. Thus, modulation of either density of the carriers and mobility (band transport or hopping transport) by interactions with gas analytes can result in the changes in electronic conductivity value.

For semiconductors and insulators, the Fermi level lies between conduction band (E_c) and valance band (E_v) . In pristine semiconductors, the Fermi level located in the center of the band gap (E_g) , while doping or defects usually shifts the Fermi level up-/down to either the conduction band or the valence band to form n-type or p-type semiconductors (Fig. 3). The activation energy (E_a) is defined by the energy difference between the Fermi level and the valence band (E_V) or the conduction band (E_C) .

The work function (W_F) can be changed by the bias potential applied to the material (Fig. 3) [79]. Considering externally applied potentials (V), it can be calculated by Eq. (1), from which one can

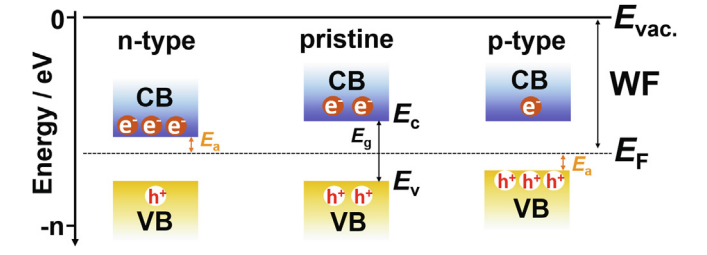


Fig. 3. Scheme showing the energy diagram of the pristine, n-type and p-type semiconductor.

comprehend phenomena like Schottky barriers and band-bending [80].

$$\varphi = V - W_F/e \tag{1}$$

where φ is the electrostatic potential.

The permittivity (ε , the dielectric constant) of a material, directly related to the vacuum permittivity ($\varepsilon_0 \approx 8.854187817 \times 1$ 0^{-12} F m⁻¹) and the relative permittivity (ε_r), is a measure of the electric polarizability of a dielectric, that is, how easily electromagnetic radiation can travel through it [81].

The interaction of the sensing material with gaseous analytes may induce changes in one or more aforementioned electrical parameters. Depending on the types of electrical devices, one of the electrical parameter changes will be transduced into a readable electrical signal and sent to the data processing component.

2.2.1.3. Data processing. Despite the direct use of raw electrical signals in some commercial electrically-transduced gas sensors for simple alarming or detection, further treatment of readout signals (data processing) is increasingly common in recent researches. It is a good method to analyze and improve the sensing performances of gas sensors without changing their components or architecture. The algorithm used for data processing can vary from simple filtering/amplifying to Statistical methods (e.g., Principal component analysis (PCA), Linear discriminant analysis (LDA), hierarchical cluster analysis (HCA), principal component regression (PCR), discriminant factor analysis (DFA), and clustering algorithms) and AI techniques (e.g., artificial neural networks (ANN), multi-layer perceptrons (MLP), radial basis function networks (RBF), selforganizing maps (SOM), and learning vector quantization (LVQ)). Moreover, the data processing will deal with readout signals from the single device, electronic nose (E-nose), or grouped sensor arrays in line with the application scenario.

2.2.2. Basic sensing performance parameters

The most important aspect of investigation of a variety of sensors is 4 'S', *i.e.* sensitivity (response), selectivity, speed (response/recovery time) and stability. In addition, some commonly used sensing parameters, including the limit of detection (LOD), reproducibility, repeatability, *etc.*, will also be discussed in this section. Details of small differences in specific parameters will be discussed in Section 2.2.4.

The response is defined as the value obtained by sensor electrically-transduced signal changes in detected gas and purging gas (Δ (saturated signal change in gaseous analytes)/(signal baseline in purging gas)). For example, the response of an n-type chemiresistor toward NH₃ in air can be obtained by Eq. (2) (Fig. 4).

Response =
$$\Delta I/I_{air} = (V/R_{air} - V/R_{gas})/(V/R_{air}) = R_{air}/R_{gas} - 1$$
 (2)

where *I* is current, *V* is the DC voltage, *R* is resistance.

The sensitivity is defined as the ratio of response and concentration (response/concentration). However, sensitivity and response

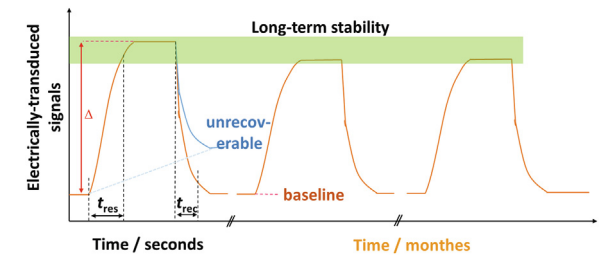


Fig. 4. A typical response-recovery curves of a n-type chemiresistor toward NH₃ for the illustration of basic sensing performance parameters.

are not fully distinguished, which sometimes have the identical meaning in a few works.

The response time ($t_{\rm res}$) and recovery time ($t_{\rm rec}$) are commonly defined as the time required for the electrically-transduced signals of the sensor to change to 90%, sometimes reduced to 80%, of the saturation/baseline value after exposure to the target/purging gas. If the continuous and significant drifting baseline or recovery is far lower than 80–90%, it will be classified as unrecoverable devices because of their failure to meet the repeatability and long-term stability of sensors in practical applications.

The long-term stability is a key factor to indicate how reliable the sensor is. Researchers usually describe the remaining percentage of sensing performances after a certain time. The long-term stability of a sensor also provides information about the optimal time required for aging process and performance reduction calibration.

The repeatability of a sensor is used to evaluate the signal change upon exposure to a certain concentration of the gaseous analytes. The reproducibility is evaluated by different devices fabricated from different batches. The coefficient of variation (*CV*) can be employed to represent either the repeatability of responses or the reproducibility of sensors, which is defined as

$$CV = R_{SD}/R_{average} \times 100\% \tag{3}$$

where $R_{\rm SD}$ refers to the standard deviation (SD), and $R_{\rm average}$ is average value of responses.

The limit of detection (LOD) of the sensors can be obtained by two methods, the IUPAC standard method and simple 10% response method.

According to IUPAC, LOD is acquired when the signal is over three times of the noise level in the system. The root-mean-square (RMS) deviation at the baseline and the slope of the response curve have been utilized to calculate the noise level and theoretical LOD of a sensor [82–84].

The simple 10% response method requires the linear relationship of response vs. concentration. A class of sensors show linear relationship of response vs. concentration, while the other class of sensors present that of log–log plots of response vs. concentration (details seen in Section 2.2.4). Based on the linear fitting line, the theoretical LOD is calculated to be the concentration with the response of 10% in line with the empirical assumption that $3RMS_{Noise}$ is normally lower than 10%. The LOD value obtained by this method is equal to or larger than that obtained by the IUPAC method, depending on the real value of $3RMS_{Noise}$ for the specific devices.

2.2.3. Basic sensing mechanisms

Although the principles of most electrically-transduced gas sensors are differing from each other, they share three similar basic mechanisms, that is, the gas diffusion before contacting, the material-analyte interactions and electrical transduction and transformation. It covers basic components of the sensing layer, electrical transducer and signal transformation mentioned in Section 2.2.1.

The gas diffusion in porous solid-phase has been discussed in Section 2.2.1. Since electrochemical sensors using liquid or solid electrolytes are not involved in the state-of-the-art MOF and MOF derived materials based electrochemical sensors, the corresponding gas diffusion will not be discussed in this review.

The interactions of gaseous analytes with sensing materials can be divided into physical and chemical interactions, in accordance with the value of the binding energy. The reversible requirements of gas sensors clearly suggest that too strong materials-analyte interactions should be avoided. Normally, the materials-analyte interactions cover van der Waals forces, hydrogen bonding, coordi-

nation bonding, reversible acid-base interactions, π - π interactions, etc

For neat MOFs, current works on chemiresistors, FET, chemical diodes, chemicapacitors and electrochemical sensors reveal that the active sites for interactions can be open metal sites, defects, adsorbed guest molecules, functional organic ligands, and MOF-electrode interfaces (non-ohmic contacts). The result of subsequently charge transfer, coordination, hydrogen bonding, acid-base interactions, π - π interactions, or redox reaction can affect one or multi-electrical parameters, which will then be transformed into readable electrical signals.

For MOF derived materials, similar active sites are observed for most of them, except that pre-adsorbed oxygen species for metal compounds, spill-over effects, and/or lattice insertion for catalytic metal-containing materials should require additional consideration.

To better understand the materials-analyte interactions and their resulting effects, fundamental mechanisms of the grain boundary for non-single-crystal forms, n/p type doping effects on fermi levels, and sensing material-electrode interface will be introduced. Minor differences or some exceptional examples depend on different types of sensors will be found in Section 2.2.4.

For both pellet- and film-type sensors, grain boundaries formed in the interfaces between neighboring grains play an essential role in the surface states and electrical transduction. As shown in Fig. 5, the potential barrier formed by the formation of grain boundaries and gas adsorption induced depletion layer for both n- and ptype semiconductors. The adsorption of gas molecules will significantly change the potential barrier height due to the formation of the dipole layers that extract/inject charge carriers from/to semiconductors during the polarization or ionization of the gaseous analytes, which then affects one or more electrical parameters. Generally, for n-type (or p-type) semiconductors and air as carrier/purging gas, the potential height will decrease (or increase) when exposed to reducing gas like NH3. Reversal behaviors will be observed when the gaseous analytes are changed to be oxidizing gas such as NO₂. In these cases, the change of the potential height depends on the concentration, binding energy and redox activity of the gaseous analytes compared with adsorbed oxygen species. The redox activity determines the increase or decrease of the potential height toward gas analytes, which determines the decrease (or increase) of the conductivity. The concentration and the binding energy result in the increase or decrease value of the conductivity and the reversibility of sensing curves, respectively.

Compared with grain boundaries formed by the same semiconductors, semiconductor heterojunctions are similar to but more complicated. Fig. 6 shows the formation of potential barriers between different semiconductor heterojunctions.

For n-n or p-p junctions, band bending occurs due to the electron/hole migration from CB/VB of one material to the other. The formation of electron/hole accumulation and the depletion layer result in the potential barriers. As for p-n junctions, the recombina-

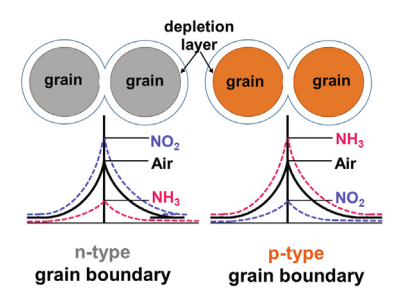


Fig. 5. The potential barrier height changes of n-/p-type semiconductor grain boundary upon exposure to air, reducing gas and oxidizing gas.

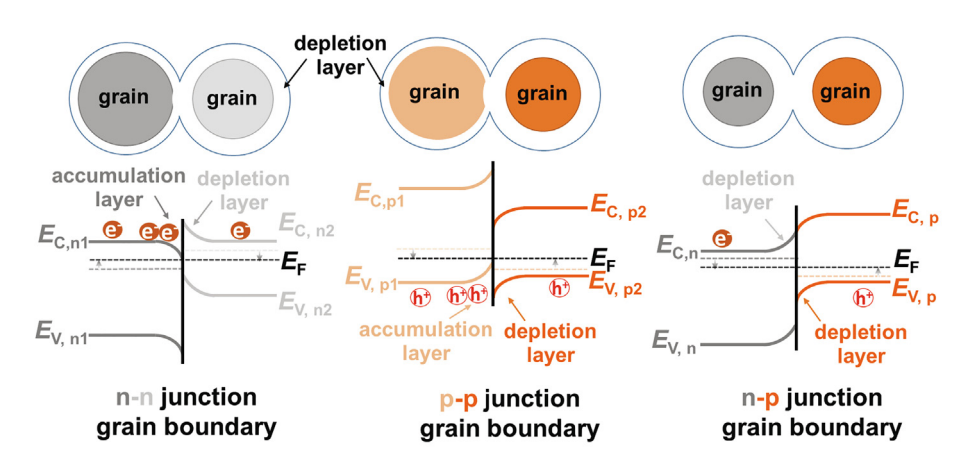


Fig. 6. Formation of a potential barrier between semiconductor heterojunctions: n-n, p-p, and n-p junctions. e⁻ denotes electron in conduction band; h⁺ denotes donor ions in valance band.

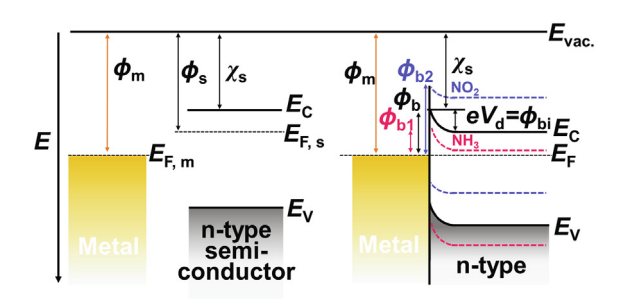


Fig. 7. Formation of a Schottky barrier between metal electrodes and n-type semiconductors ($\phi_{\rm m} > \phi_{\rm s}$): the energy diagram before contact (left) and the band alignment and energy diagram after contact (right).

tion of electrons from CB of n-type semiconductor with holes from VB of p-type semiconductor will form the depletion layers in the contacting area. Normally, the proper design of the composition and structure of heterojunctions can help such barriers or depletion layers facilitate additional oxygen adsorption and thus enhance the sensing properties.

For non-ohmic contact devices (e.g. chemical diodes, chemica-pacitors), the interfaces between the sensing layer and metal electrodes are also pivotal in determining the sensing performances. In cases of metal–semiconductor junctions (e.g. chemical diodes), Fig. 7 shows the energy diagram of metal electrodes and n-type semiconductors before and after contact, of which the work function of the semiconductor $(\phi_{\rm s})$ is smaller than that of the metal $(\phi_{\rm m})$.

In case of electrical contact of the metal and the semiconductor, the two Fermi levels are forced to coincide with electrons passing from the semiconductor into the metal ($\phi_m > \phi_s$). Besides, the corresponding potential barrier height is also well-known as Schottky barrier height (ϕ_b). According to the Mott-Schottky model, for an ideal contact between a metal and an n-type semiconductor, the height of the barrier ϕ_b measured relative to the Fermi level is given by Eq. (4).

$$\phi_{b=}\phi_m - \chi_s \tag{4}$$

where χ_s refers to the electron affinity of the semiconductor, defined as the difference in energy between an electron at rest outside the surface and that at the bottom of the conduction band just inside the surface.

Fig. 8 shows the other three types of metal–semiconductor contact. In the case of $\phi_{\rm m} < \phi_{\rm s}$ or $\phi_{\rm m} > \phi_{\rm s}$ for the n- or p-type semiconductor, the contact is ohmic, countering no barriers. In the case of $\phi_{\rm m} < \phi_{\rm s}$ for p-type semiconductor, holes transport from the semi-

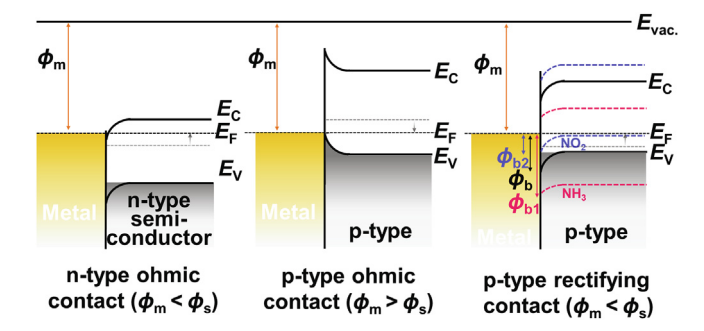


Fig. 8. The band alignment and energy diagram after contact: ohmic contact of metal with n-type semiconductor (left, $\phi_{\rm m} < \phi_{\rm s}$), ohmic contact of metal with p-type semiconductor (middle, $\phi_{\rm m} > \phi_{\rm s}$), and formation of a Schottky barrier between metal electrodes and p-type semiconductors (right, $\phi_{\rm m} < \phi_{\rm s}$).

conductor to the metal, resulting in the depletion layer in the semi-conductor. The Schottky barrier height (ϕ_b) of p-type semiconductor is given by

$$\phi_b = E_g - (\phi_m - \chi_s) \tag{5}$$

When the metal–semiconductor junction is exposed to reducing (or oxidizing) gas, the Schottky barrier height (ϕ_b) can be lowered in consideration of the charge state change at the interfaces of metal electrode and n-type (or p-type) semiconductor, otherwise contrary behaviors will be observed.

As a secondary effect, the metal–semiconductor junctions can also be applied to host sensing materials to improve performances of other electrically-transduced gas sensors. Typical examples are noble metal decorated MOx chemiresistors, MOF derived metal/CNT chemiresistors, and so on.

Concerning metal-insulator junctions, details of sensing mechanisms can be found for examples of chemicapacitors in Section 2.2.4.

Above basic mechanisms can be applied to pristine materials, second phase doping and heterojunctions of neat MOFs, MOFs based composites and MOF derived materials. For cases involved in lattice doping, additional considerations on doping energy states induced shifts of Fermi levels, changes of carrier density and mobility, and possible catalytic effects should be taken to understand the complicated mechanism.

2.2.4. Typical examples of different types of electrically-transduced gas

2.2.4.1. Chemiresistors. Chemiresistive gas sensors are the simplest and most widely applied devices among various gas sensors due to

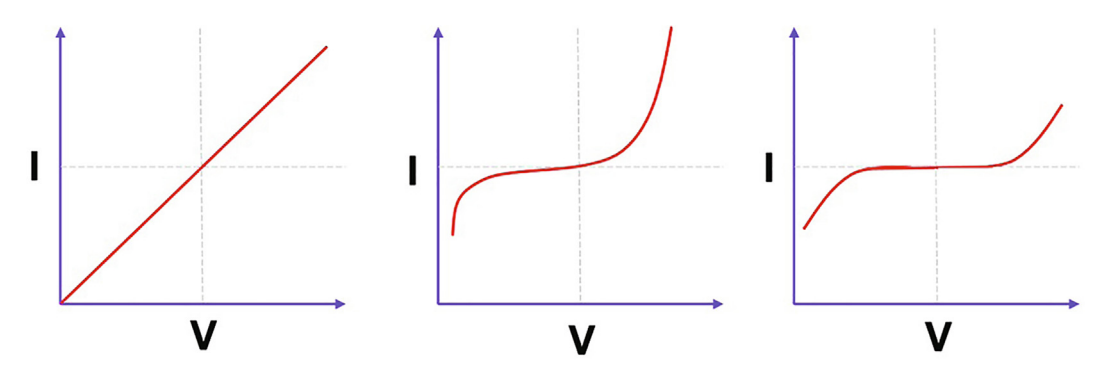


Fig. 9. I-V curves under DC bias: chemiresistors (left), chemical diodes (middle), proton/ions types (right). Reproduced with permission [85].

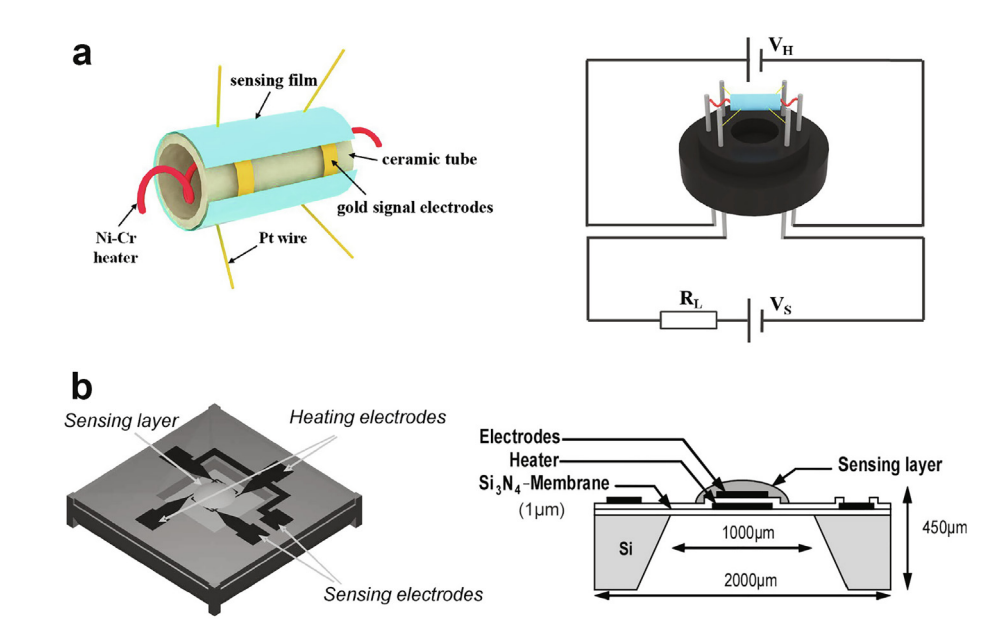


Fig. 10. Typical chemiresistive sensing elements: (a) the indirect-heated type derived from the well-known Figaro-Taguchi type (TGS) sensor and its test circuit. Reproduced with permission [98]. Copyright 2018, Elsevier. (b) 3D view and side view of microelectromechanical system (MEMS) type. Reproduced with permission [99]. Copyright 2007, Wiley-VCH Verlag GmbH & Co. KGaA, Weinheim.

its inherently simple in concept (resistance change), low cost, portability, real-time operability and ease of use [4,74,85–88]. Great efforts have been devoted to further improving the sensing performances by studies on both sensing materials and devices. However, their long-term bottlenecks of poor selectivity and high operating temperature are still great challenges posed to researchers.

The first practical chemiresistor, which can be traced back to the early 1960s [89], is a simple semiconudctor device containing an active MOx sensing layer with two electrodes. Such research also gives birth to the first commercial sensor producer (Figaro Engineering Inc., Japan), which started mass production and sale of the TGS in 1968. At that time, the name of this type was called as the semiconductor type gas sensor, which is well consistent with the MOx semicondcutor sensing materials used in the device. Then the name of chemiresistors started to be used in the late 1970s [90] and was gradually accepted by more and more researchers in 1980s [91,92]. There are two reasons: one is that sensing materials were further extended to conducting/semiconductive polymers, the other is the more accurate matching with the resistance changes of such devices induced by chemical interactions with gaseous analytes (redox reactions). Sometimes, terms of the "chemoresistor" or the "chemi-resistor" will also be adopted [5,93-97].

The architecture of sensing materials with two metal electrodes with/without insulating substrate has kept unchanged so far, while the sensing materials now cover either semi-conductive or metallic sensing materials that show the resistance change upon exposure to the gaseous analyte. Considering the history and current status of gas sensors of this kind, the name of the "chemiresistor" or the "chemiresistive gas sensor" is recommended to be used. However, to better distinguish from other sensors, we will recommend the definition that requires the ohmic contact of sensitive materials and electrodes. In other words, a chemiresistor is an ohmiccontacting resistor with two electrodes, the resistance change of which is dominated by chemical interactions of sensing materials with gaseous analytes. The ohmic contact can be easily confirmed by good linearity of I-V curves under DC bias (Fig. 9). The definition also avoids confusions with other sensors containing two electrodes but showed nonlinear I-V curves under DC bias, such as chemical diodes, proton/ions types (impedance-type electrochemical sensors, proton/ions assisted resistors), which will be introduced in other sections.

For chemiresistors, their output signals are based on different methods: i). measuring the resistance of the device directly; ii). measuring the current under a constant DC bias voltage; iii). measuring the partial voltage on the device in parallel with a constant resis-

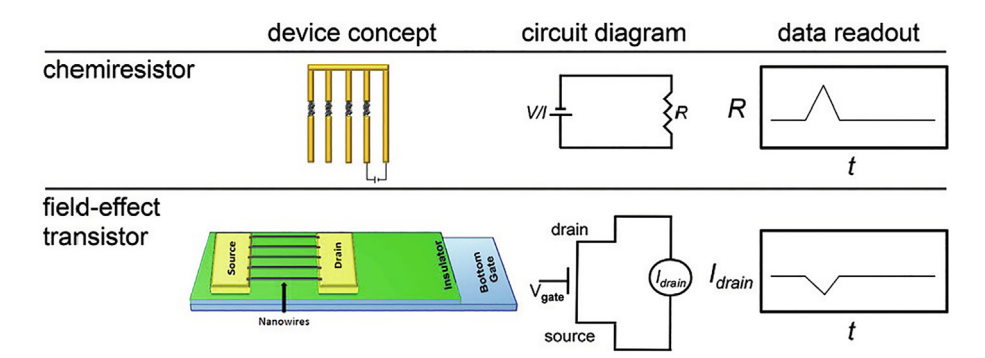


Fig. 11. Graphical representation of the differences between chemiresistor and FET devices and corresponding circuit diagrams and typical data readouts. Reproduced with permission [131]. Copyright 2016, Wiley-VCH Verlag GmbH & Co. KGaA, Weinheim.

tance when the resistance and device is applied a constant DC bias voltage.

The chemiresistive sensing elements can either be the pellet-, film-type or the single crystal-type, which can be seen in Fig. 2. Film-type chemiresistors are most common form for both fundamental research and commercial devices. Besides the simple two-electrodes thin/thick film on plat substrates (Fig. 2c), Fig. 10 shows another two types: the indirect-heated type derived from Figaro-Taguchi type (TGS) sensor [98] and microelectromechanical system (MEMS) type sensor [99]. The indirect-heated type chemiresistor normally composed sensing film, an insulating tube with a pair of metal electrodes, and a Ni–Cr heating wire inserted into the tube. Nano-micro technologies generate the quite small MEMS type in comparison with the indirect-heated chemiresistor.

The complicated sensing mechanisms of chemiresistors may comprise one or more mechanisms, such as catalytic effects [100–108], charge transfer [109–113], charge carrier transport pathway modulation [114–116], manipulation/construction of heterojunctions [117,118], and molecular binding/sieving [119–124]. However, from the fundamental understanding of the resistance change toward gaseous analyte adsorption, we can try using some formula to illustrate a few common issues.

The resistance of the device is mainly determined by the resistance of sensing materials and the electrode-materials contact. For grain-based gas sensors, the depletion layer based on the adsorbed polarization or ionization gas molecules induced the dipole layers allows the formation of the intergranular potential/Schottky barrier (Figs. 5–8 in Section 2.2.3). With aspect to it, two famous material-analyte interaction models based on the MOx chemiresistor that show good consistencies with many semi-conductive chemiresistors have been proposed, namely the *Ionosorption Model* (oxygen ionosorption: molecular (O_{ads}^2) and atomic (O_{ads}^-) , O_{ads}^{2-}) ions)

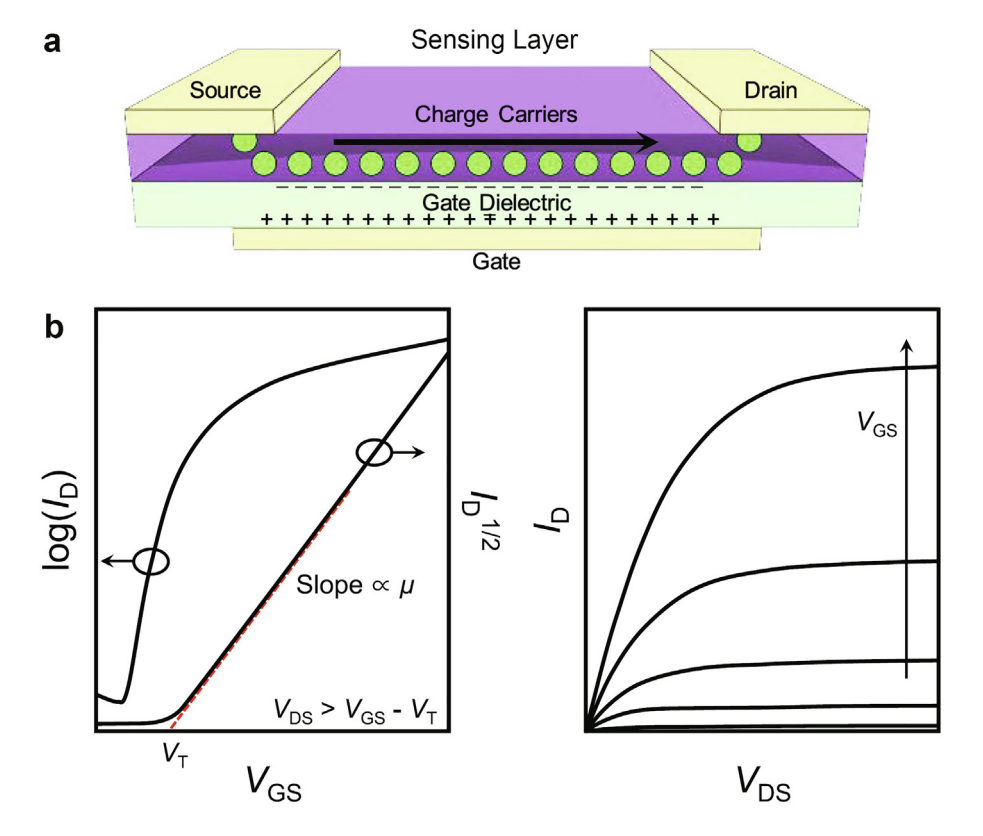


Fig. 12. (a) Schematic diagram of a p-type FET with bottom-gate top-contact structure and hole (h^*) as charge carriers. (b) The transfer (left) and output (right) curves of FETs operated in a saturation regime ($V_{DS} > V_{CS} - V_T$). Reproduced with permission [132]. Copyright 2017, Elesvier.

and *Oxygen-Vacancy Model* (reduction–reoxidation mechanism). According to the conductance model limited by the electron transport across the intergranular potential/Schottky barrier [125,126], the response of grain based gas sensors can be explained by using Eq. (6) (for resistance increase) [125,127–129]

Response =
$$(\sigma_{gas} - \sigma_{air})/\sigma_{air} = R_{air}/R_{gas} - 1 = A_g p_g^{\beta}$$
 (6)

where $\sigma_{\rm air}$ refers to the conductance without the gaseous analytes, $p_{\rm g}$ is the gaseous analytes partial pressure, $A_{\rm g}$ is a prefactor, and the exponent β is the response order. It can be rewritten as

$$\log Response = \log(R_{air}/R_{gas} - 1) = \log A_{g} + \beta \log p_{\sigma}$$
 (7)

It is conspicuous that there is a good linear relationship between response and gaseous analyte partial pressure (proportional to the concentration, c). By fitting the log–log plots of the response vs. concentration, one can easily estimate the LOD value (Section 2.2.2) and the microstructure. According to the report, when β is equal to 0.5, a fully regular microstructure of the nanoparticles is indicated [128], whereas that value is expected to exceed 0.5 in the case of disordered microstructure. Furthermore, there is a reduction of β below this value because of local agglomeration or zones of the structure [127,130].

Above formula can be used for most chemiresistors, while there is some exception due to the new adoption behaviors or mixed

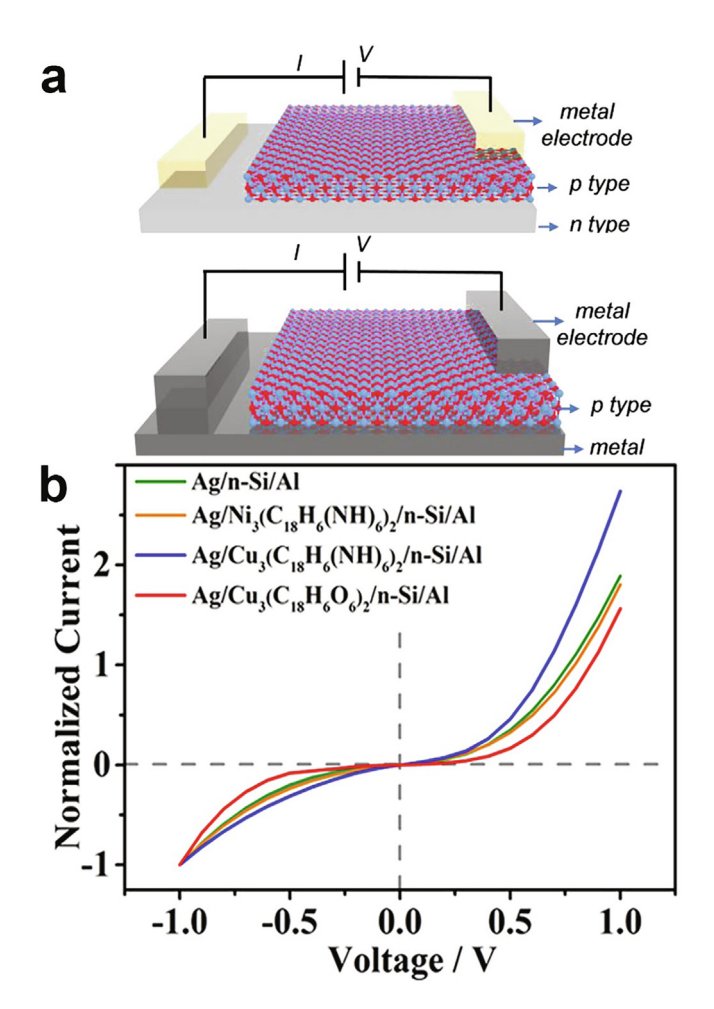


Fig. 13. (a) Scheme diagram of a typical p-n junction diode sensor (upper) and a typical Schottky barrier diode sensor (lower). Reproduced with permission. Copyright 2019 [2], American Chemical Society. (b) I-V plot of Ag/n-Si, Ag/Ni₃(C₁₈H₆(NH)₆)₂/n-Si, Ag/Cu₃(C₁₈H₆N₆)₂/n-Si, and Ag/Cu₃(C₁₈H₆O₆)₂/n-Si devices. Reproduced with permission [133]. Copyright 2020, Royal Society of Chemistry.

mechanisms for new sensing materials such as carbon, certain types of MOFs, metals (e.g. Pd for H_2) and their composites.

2.2.4.2. Field-effect transistors (FETs). Field-effect transistors (FETs) are three-terminal semiconductor devices with a gate terminal controlling the channel current between the source and the drain terminals.

Fig. 11 shows the differences between chemiresistor and FET-type gas sensors on device structure, circuit diagram and data readout [131]. A typical FET-type gas sensor consists of similar two electrodes (source and drain), sensing film and insulating layers (dielectric layers, e.g. SiO₂, GaN, and MOx), while an additional gate electrode is used as a valve to modulate sensing film's interfacial properties and electrical parameters such as mobility, carrier density, etc. Accordingly, the circuit diagram and data readout of the FET-type gas sensor are changed. Besides, the gate electrode can be either in the bottom of the device or parallel to source/drain electrodes with/without the electrolyte.

To understand the data readout of FETs, that is, the drain current, $I_{\rm DS}$, working principles should be taken into consideration. Generally, $I_{\rm DS}$ is controlled by modulating the voltage of a gate-source terminal ($V_{\rm GS}$), where there is transportation of charge carriers (holes (h⁺) and/or electrons (e⁻)) in the channel region near the interface between the semiconductive sensing layer and dielectric layers (Fig. 12a) [132]. Depending on energy-level relationships between the semiconductor and the source/drain electrodes, the device exhibits n-channel, p-channel, and ambipolar operating behaviors. As shown in Fig. 12b [132], depending on the relative applied voltages of the electrodes, current–voltage (*I-V*) characteristics of FETs in saturation regime or linear regime (Ohm's law) are given in Eqs. (8) and (9), respectively.

$$I_{DS} = 1/2 W/L\mu C_i (V_{CS} - V_T)^2, V_{DS} > V_{CS} - V_T$$
 (8)

$$I_{DS} = W/L\mu C_i(V_{GS} - V_T)V_{DS}, V_{DS} < V_{GS} - V_T$$
 (9)

where $I_{\rm DS}$ refers to the drain current, W/L is the ratio of width-to-length of the channel, μ refers to the charge carrier mobility in the channel, $C_{\rm i}$ refers to the capacitance of the gate insulator/dielectric per unit area, $V_{\rm T}$ refers to the threshold voltage of the transistor, $V_{\rm GS}$ and $V_{\rm DS}$ represents the applied voltage between drain-source and gate-source, respectively.

Basic sensing mechanisms of the FET-type gas sensor are similar to chemiresistors with the primary differences of additional conductivity/resistivity changes attributed to gate electrode modulation, metal-semiconductor contact (Fermi-level shift) and capacitance of the insulating layer upon exposure to gaseous analytes. At the given $V_{\rm DS}$ and $V_{\rm GS}$, the response of FET-type gas sensor with n-type channel toward reducing gaseous analytes is

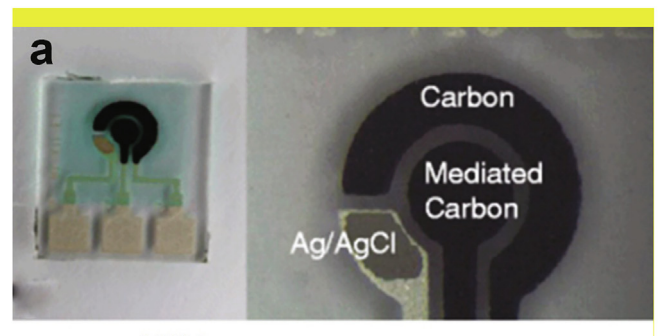
Response =
$$\Delta I_{DS}/I_{DS,air} = (I_{DS,gas} - I_{DS,air})/I_{DS,air}$$

= $I_{DS,gas}/I_{DS,air} - 1$ (10)

2.2.4.3. Chemical diodes. A chemical diode is a two-electrode sensor that merely allows the current to flow in one direction. The key resistance-dominated element is the p-n junction (Fig. 6) or metal-semiconductor Schottky junction (Figs. 7 and 8), the basic device schematic diagrams of which are shown in Fig. 13a [2]. The performances of chemical diodes are bound up with p-n junctions or height of Schottky barrier (Φ_B). The height of potential or Schottky barrier (Φ_B) can be estimated by Eq. (4) for n-type or Eq. (5) for p-type semiconductor.

The I-V response of these diodes is modelled using the ideal diode equation [134,135]:

$$I = I_{sat}[exp(eV/(hkT)) - 1]$$
(11)



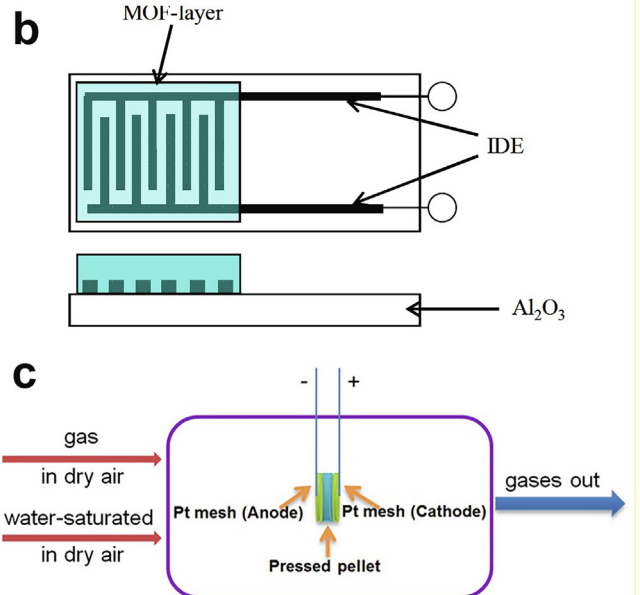


Fig. 14. (a) Co-phthalocyanine mediated screen-printed three electrodes for electrochemical impedance spectroscopy (EIS). Reproduced with permission [140]. Copyright 2014, Springer. (b) top view and cross sectional view of MOF paste screen-printed on laser-patterned interdigital electrodes (IDE). Reproduced with permission [138]. Copyright 2009, MDPI. (c) Illustration of the gas-sensing measurement system for two electrodes MOF pellet electrochemical gas sensors. Reproduced with permission [139]. Copyright 2018, Wiley-VCH Verlag GmbH & Co. KGaA, Weinheim.

where e refers to the electronic charge, V refers to the applied voltage, k refers to the Boltzmann constant, η refers to the ideality factor expressed as $\eta = (e/kT)$ ($dV/d(\ln I_{sat})$), and I_{sat} refers to the reverse saturation current.

For p-n junctions, by taking the natural log of Eq. (11), the ideal diode equation of the linear region of the forward bias is represented as:

$$ln I = eV/(\eta kT) + ln I_{sat} = V/\eta V_t + ln I_{sat}$$
 (12)

where $V_{\rm t}$ is the thermal voltage (e/kT, 0.026 V at RT). The slope and intercept of the fitted line to the linear region give the values of η and $I_{\rm sat}$. The ideality factor is a figure of merit that describes the recombination behavior of the device. A p-n junction diode governed purely by diffusion current will have n=1 (ideal diode), while a device dominated by recombination will have n=2.

The reverse saturation current, $I_{\rm sat}$, is a value to measure the number of carriers that can overcome the energetic barrier generated by the p-n junction or Schottky barrier in the reverse bias direction, which should be minimized to enhance the overall rectification of the diodes.

The current-voltage (I-V) or current density-voltage (J-V) plot is widely utilized to describe the characteristics of a diode (Fig. 13b) [133]. The response can be the gas-induced voltage

shifts at a given diode current I (or current density J), ΔV ; or current changes at a given diode voltage, ΔI [133,136]; or rectification ratio (defined as the forward current divided by the reverse current, I_F/I_R) changes [137].

As can be seen from above formulas, the sensing performances of chemical diodes can be modulated by altering the Schottky barrier height, modifying the built-in voltage, varying energy states of semiconductors or tuning the interfaces.

2.2.4.4. Electrochemical sensors. As gas sensors with broad application, electrochemical sensors show promising performances in both fundamental researches and commercial applications, including environment detection, food safe, medical diagnostics, and chemical treat detection. Detection strategies of electrochemical sensors include potentiometry, voltammetry, impedance spectroscopy, and conductometry. Major researches on MOFs and MOF derived materials based electrochemical gas sensors have been electrochemical impedance spectroscopy (EIS) strategy so far. There is plenty of room for exploring potential applications as the sensing/functional materials for other types of electrochemical gas sensors.

EIS is conducted by measuring the impedance, a frequency (typically 10⁶ to 10⁻⁴ Hz) dependent resistance, after an electrical stimulation (the voltage or the current) in the AC mode. Unlike the three-electrode configuration for electrochemical sensors working in solutions or solid electrolytes (WE refers to the working electrode; CE refers to the counter electrode; RE refers to the reference electrode, Fig. 14a), reported MOFs and MOF derived materials based electrochemical gas sensors adopt two electrodes (e.g. the thin/thick film on insulating substrates with IDEs, pressed pellets with two electrodes) and work under gas/vapor atmosphere (Fig. 14b and c) [138,139]. Generally, impedance data can be represented utilizing either the Nyquist plot or the Bode plot. The former is frequently-used and consists of the negative imaginary part of the impedance -Z'' (the y axis) vs. real part of the impedance Z'(x axis). After mathematical calculations based on an equivalent electrical circuit (e.g. resistors, capacitors and/or inductors), the electrochemical characteristics of a studied system can be accessible, including conductivity, dielectric constants, reaction rates, and mass transport. Moreover, there is a need to extract information regarding frequency (f) from the Bode plot, the log-log plots of the double Y axis (the impedance Z and the phase shift φ) vs. frequency.

EIS exhibits ultra-sensitive capability to changes caused by either surface or bulk phenomena, which is an ideal method to study ionic/protonic involved gas sensing performances and a promising gas sensor for practical applications.

2.2.4.5. Chemicapacitors. A chemicapacitor is a sensor device made up of two electrodes separated by an insulating layer (the dielectric layer, e.g., air, N_2 , ceramic, mica, and MOFs), which shows the capacitance change caused by the interactions of the dielectric layer with gaseous analytes under the AC voltage. From the definition, one can easily figure out that the sole difference of the components of a chemicapacitor and a chemiresistor is active materials, which means that all pellets, thin/thick films and single crystal forms can be applied to the chemicapacitor as well. The capacitance (C, farads (F)) of a chemicapacitor can be given by Eq. (13) (Section 2.2.1.2).

$$C = \varepsilon A/d = \varepsilon_r \varepsilon_0 A/d \tag{13}$$

where ε_r is the relative static permittivity (the dielectric constant) of the material between the plates, A is the area of each plate/electrode (m²), and d is the separation distance (m) of the two plates/electrodes.

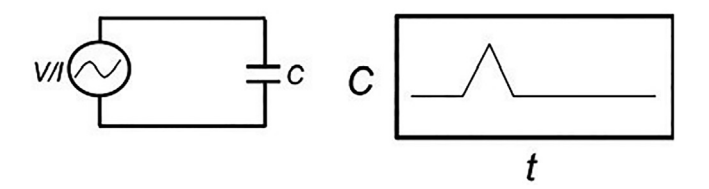


Fig. 15. Graphical representation of the circuit diagrams (left) and typical data readouts (right) of chemicapacitors. Reproduced with permission [131]. Copyright 2016, Wiley-VCH Verlag GmbH & Co. KGaA, Weinheim.

Based on Eq. (13), the capacitance is determined by the dielectric constant $\varepsilon_{\rm r}$ and the separation distance d. In general, changes of the dielectric constant $\varepsilon_{\rm r}$ are not prominent because of the similar relative permittivity of most inorganic gas. In contrast, the separation distance d is more sensitive to capacitive gas sensing. However, H₂O is an exception that may change the dielectric constant, the separation distance and the area of plates/electrodes. At the given V, the response of chemicapasitive gas sensor with increased capacitance toward gaseous analytes is

Response =
$$\Delta C/C_{air} = (C_{gas} - C_{air})/C_{air} = C_{gas}/C_{air} - 1$$
 (14)

Fig. 15 shows the simplified circuit diagrams and typical data readouts of chemicapacitors [131]. The simple and low cost configuration enables its miniaturization and integration with other devices. The success of commercial capacitive humidity sensors is a solid example for its low energy consumption, low cost, long-term stability and ease of integration [27,28,141,142]. However, for gaseous analytes except water, the selectivity still poses a great challenge for the chemicapacitor.

2.2.4.6. Others. Besides five main categories of electrically-transduced gas sensors, there are some new families of sensors

reported. For example, Kelvin probe gas sensors are principally based on the work function changes toward gas interactions [143], detailed discussions on which will not be included in this review because work function change normally can be transformed to the common current/voltage signal in practical applications. In addition, complicated electrically-transduced gas sensors with combined basic working principles that cannot be clearly classified as a category will be discussed in the section of the major working principle.

3. Metal-organic frameworks (MOFs) and their derivatives for chemiresistive gas sensors

3.1. MOFs as active materials for chemiresistive gas sensors

MOFs have attracted significant attention in the area of gas sensing because of two reasons. One is that their ultra-high surface areas, regular porosity and tunable structures will not only improve the sensitivity by providing plenty of accessible active sites for gas adsorption, but also enhance the selectivity toward targeted gaseous anlaytes by modulated channel traffic effects. The other is that, the new subfamily of ionic-/protonicconductive and electronic-conductive MOFs (IC/PC-MOFs and EC-MOFs) will provide additional room temperature sensing activity, which provides the possibility of cascading sensitivity, selectivity and room working temperature into a single device. Recent progress on MOF-on-MOF, the MOx/MOF, and the MOF-polymer, MOFs are more promising as active or functional materials for gas sensing. Due to the electrical characteristic of ions/protons, IC-MOFs and IC-MOF composites will be discussed in sections corresponding to FET, electrochemical sensors and chemicapacitors.

3.1.1. Neat MOFs for moderate temperature chemiresistive gas sensing Since the report on neat MOF electrochemical gas sensor by Achmann *et al.* in 2009, researchers have started to ponder on the appli-

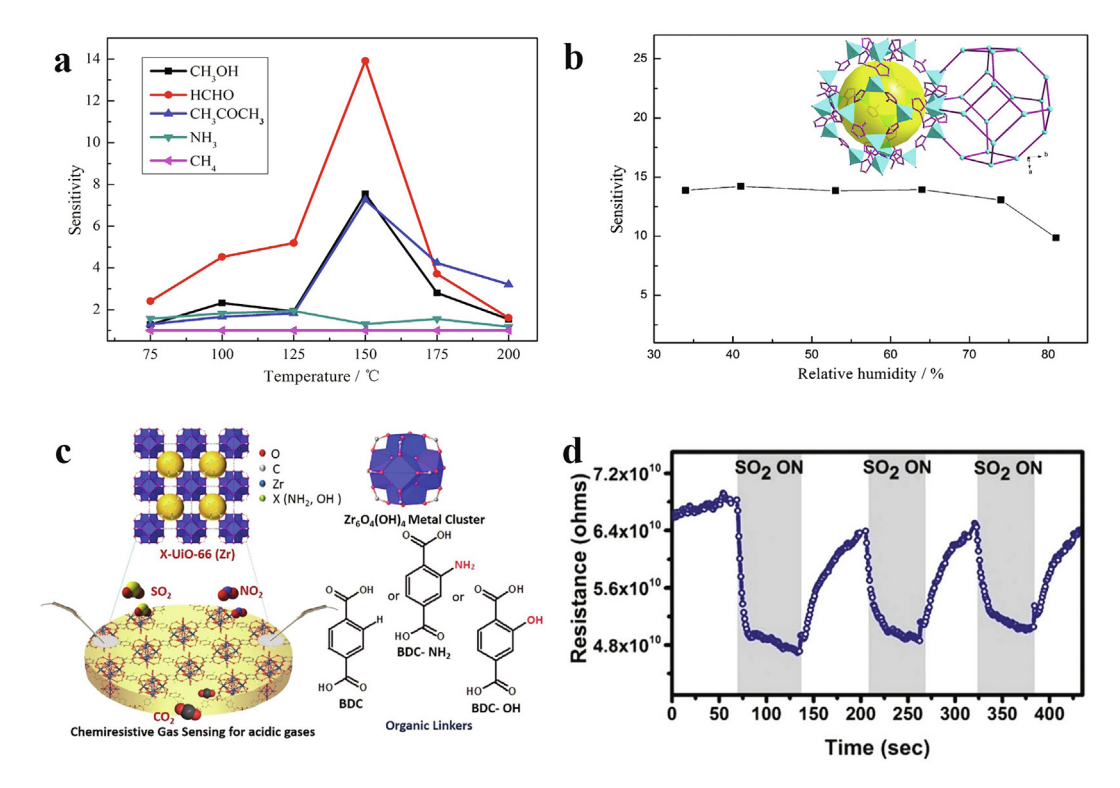


Fig. 16. (a) Sensitivity of the ZIF-67 sensor to different 100 ppm gaseous measured between 75 and 200 °C; (b) Effect of environmental humidity on ZIF-67 sensor sensitivity (inset: SOD-type structure of ZIF-67). Reproduced with permission [144]. Copyright 2014, American Chemical Society. (c) Illustration of chemiresistive sensing of acidic gaseous by the modulation of organic linker in UiO-66 MOF; (d) Gas sensing performance of NH₂-UiO-66(Zr) toward 10 ppm of SO₂ at an operating temperature of 150 °C. Reproduced with permission [147]. Copyright 2019, The Royal Society of Chemistry.

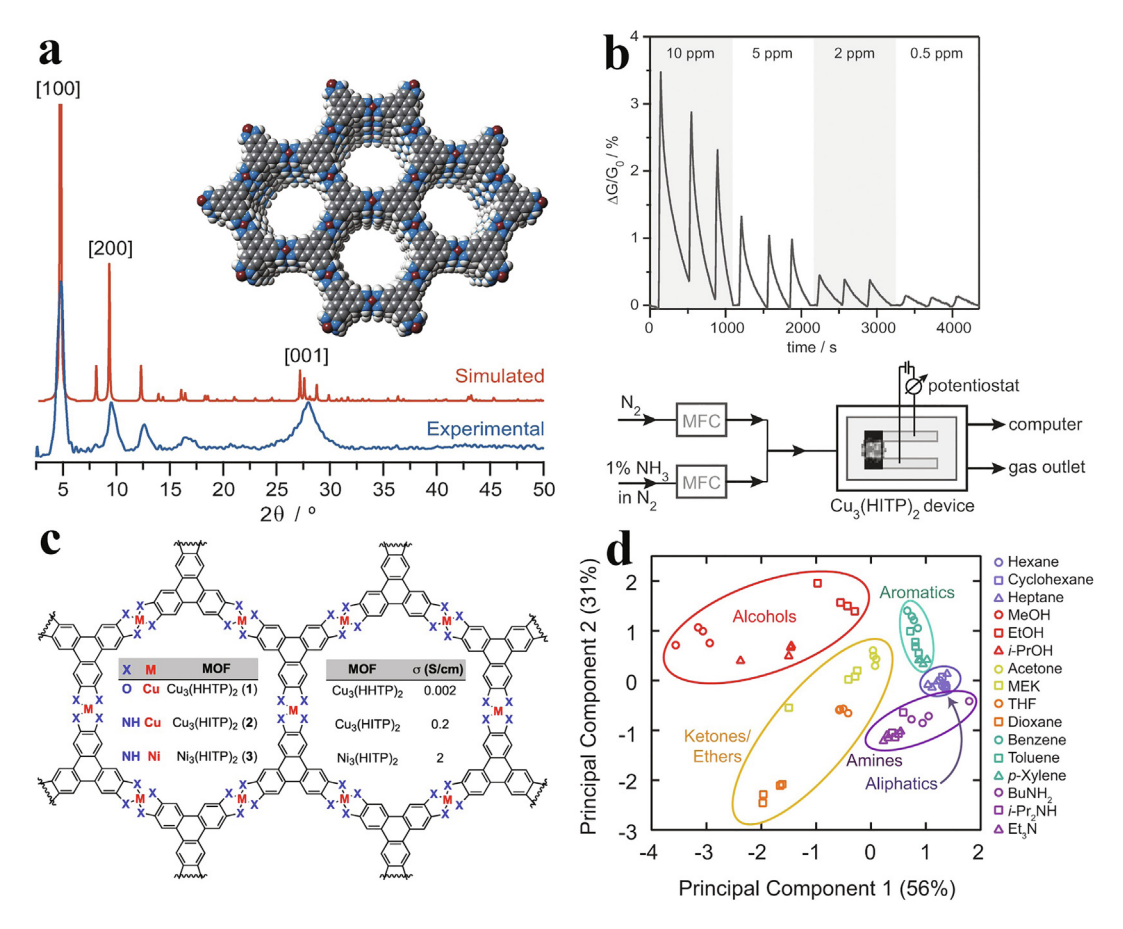


Fig. 17. (a) Experimental and simulated PXRD pattern for Cu₃(HITP)₂ with a slipped-parallel packing structure of the 2D sheets. The inserted image presented the simulated structure of Cu₃(HITP)₂ (along *c* axis) (gray: carbon, white: hydrogen, blue: nitrogen, red: copper); (b) Relative responses of a Cu₃(HITP)₂ device to ammonia with variable concentrations (including 0.5, 2, 5, and 10 ppm) with nitrogen gas. The below image is the schematic of experimental apparatus; MFC refers to the mass flow controller. Reproduced with permission [22]. Copyright 2015, Wiley-VCH Verlag GmbH & Co. KGaA, Weinheim. (c) Chemical structures of the isostructural conductive 2D MOFs with respective electrical conductivities (two-probe, pressed pellet, RT).; (d) Principal component analysis of the response to VOCs of these 2D conductive MOF sensor array's responses to VOCs. Reproduced with permission [149]. Copyright 2015, American Chemical Society.

Table 1Room-temperature gas-sensing properties toward NH₃ of various chemiresistive gas sensors working at RT. (1. Experimental LOD, 2. IUPAC method, 3. 3RMS with simulated equation, 4. 10% response).

Material	Structure	Conc.	R	t _{res} /min	$t_{\rm rec}/{ m min}$	LOD/ppm	σ /s cm $^{-1}$	$\mathrm{BET}/\mathrm{m}^2~\mathrm{g}^{-1}$	Refs.
CuTCNQ	thin film	50 ppm	~0.1%	~4	N.A.	10 ¹	0.2ª	N.A.	[264]
CuTCNQF ₄	thin film	99 ppm	4.34%	~5	N.A.	10^{1}	N.A.	N.A.	[241]
Cu ₃ (HHTP) ₂	thick film	80 ppm	0.7%	N.A.	N.A.	2^1	0.002^{a} [149]	540[263]	[150]
Ni ₃ (HHTP) ₂	thick film	80 ppm	0	N.A.	N.A.	0	0.1 ^a [266]	N.A.	[150]
Cu ₃ HITP ₂	thick film	10 ppm	3%	N.A.	N.A.	0.5^{1}	0.2^{a}	N.A.	[22]
Ni ₃ HITP ₂	thick film	10 ppm	0	N.A.	N.A.	0	2^{a} , 40^{c}	690	[22]
Cu ₃ (HHTP) ₂	thin film	100 ppm	129%	1.36	9.11	0.5^{4}	0.02 ^d	N.A.	[162]
NiPc-Ni	thick film	80 ppm	~45%	>10	Irrev.	$0.05 - 0.31^2$	$\sim 7.2 \times 10^{-4b}$	101	[166]
NiPc-Cu	thick film	80 ppm	~45%	>10	>10	$0.16 - 0.33^2$	$\sim\!1.4\times10^{-2b}$	284	[166]
Cu-HHTP-THQ	thick film	100 ppm	~20%	1.65	2.57	0.35^2 , 0.02^3	$\sim\!\!2.5\times10^{-5a}$	441.2	[168]
Cu-BTC@GO-25	thick film	100 ppm	4%	>10	>10	100 ¹	N.A.	916	[199]
Ni ₃ (HHTP) ₂ -on-SLG	thin film	100 ppm	~6.75%	N.A.	N.A.	0.01 1	$\sim 4 \times 10^{4d}$	N.A.	[200]

a two probe pellet,

cation of such promising materials on simpler and cheaper devices, chemiresistors. Unfortunately, their insulating nature of most reported MOFs at that time hindered them from using as active materials of chemiresistors. Fortunately, for semi-conductive MOFs, the electrical conductivity increases with increments on temperature due to the additional thermal activated chare carriers. Based on this, Zhang's group reported two semiconductive MOFs with

good thermal stability, cobalt 2-methylimidazolate $Co(mim)_2$ (ZIF-67, 150 °C) [144] and cobalt imidazolate $[Co(im)_2]_n$ (75 °C) [145], which exhibited selective response to targeted gas free from interference of cross-sensitive humidity (Fig. 16a and b). Similarly, later in 2019, NH₂-UiO-66(Zr), a famous subfamily MOF firstly developed by the Professor Karl Petter Lillerud at the Department of Chemistry, University of Oslo [146], is reported to exhibit ideal chemiresistive

^b four probe,

c van der Pauw,

^d two probe thin film, irrev. is irreversible.

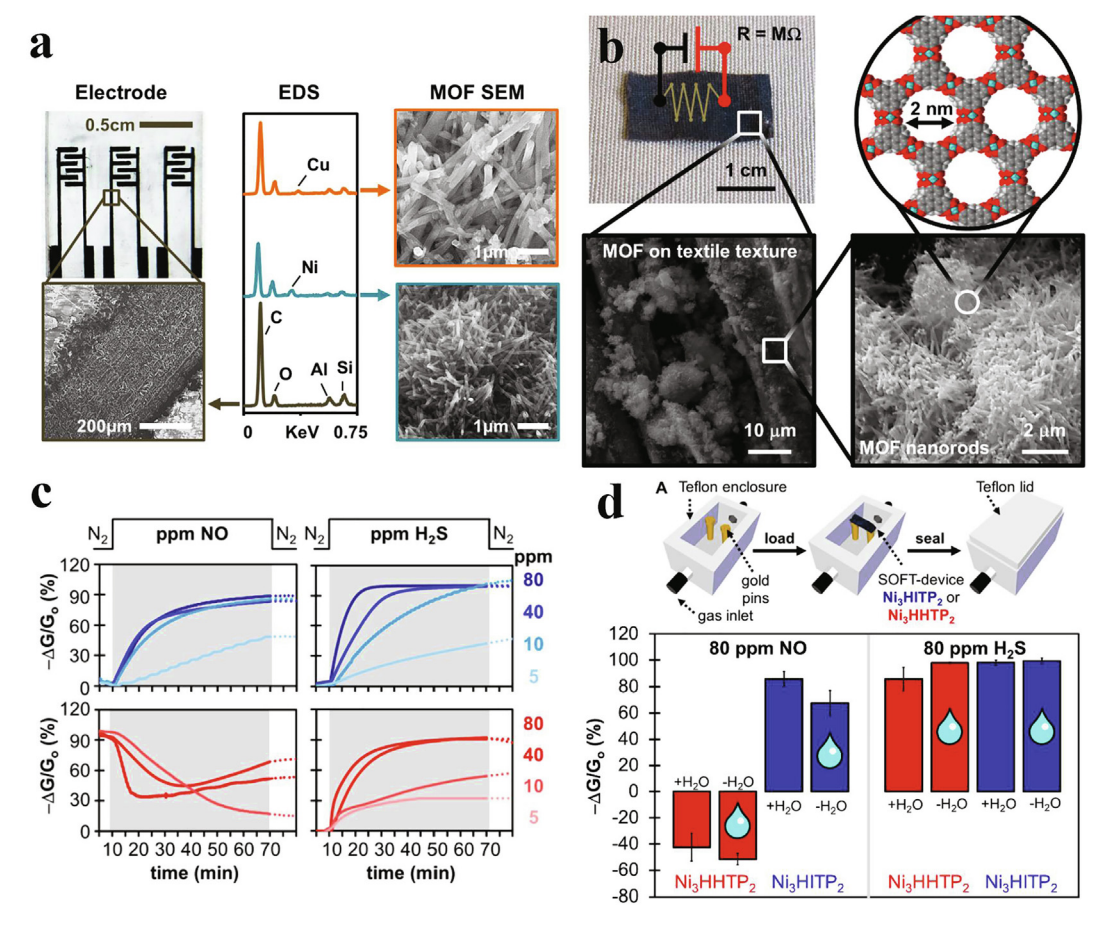


Fig. 18. (a) Characterization of MOF-based chemiresistors with EC-MOF nanowires directly grown on shrinkable polymeric substrates. Photograph of a typical triplicate device after shrinking, SEM images and localized EDS of MOF films (blue and orange traces) incorporated into devices and of graphite composite electrodes (bottom trace). Reproduced with permission [150]. Copyright 2016, American Chemical Society. (b) Digital photo and SEM images of EC-MOFs SOFT devices (inset: space-filling model of MOF). (c) The sensing performance of Ni₃HITP₂ (blue) and Ni₃HITP₂ (red) SOFT-sensors towards NO or H₂S; (d) Custom enclosure for dosing SOFT-sensors with analytes and Summarized saturation sensor response for Ni₃HHTP₂ (red) and Ni₃HITP₂ (blue) towards 80 ppm of NO and H₂S in dry nitrogen (solid bars) and in the presence of 5000 ppm water (with water droplet) with consistent function between dry and humid (18% RH) environments. Reproduced with permission [151]. Copyright 2017, American Chemical Society.

Table 2Room-temperature gas-sensing properties toward NO of various chemiresistive gas sensors working at RT. (1. Experimental LOD, 2. IUPAC method, 3. 3RMS with simulated equation, 4. 10% response).

Material	Structure	Conc.	R	t _{res} /min	$t_{\rm rec}/{ m min}$	LOD/ppm	σ /s cm $^{-1}$	$\mathrm{BET}/\mathrm{m}^2~\mathrm{g}^{-1}$	Refs.
Cu ₃ (HHTP) ₂	thick film	80 ppm	~1.8%	N.A.	Irrev.	2^1	0.002 ^a [149]	540[263]	[150]
$Ni_3(HHTP)_2$	thick film	80 ppm	~1.7%	N.A.	Irrev.	2^{1}	0.1 ^a [266]	N.A.	[150]
$Ni_3(HHTP)_2$	thick film	80 ppm	~49%	N.A.	Irrev.	1.4^{2}	0.1 ^a [266]	N.A.	[151]
Ni ₃ HITP ₂	thick film	10 ppm	~81%	N.A.	Irrev.	0.16^2	2^{a} , 40^{c}	690	[151]
NiPc-Ni	thick film	1 ppm	~657%	>10	Irrev.	$0.06 - 1.06 \times 10^{-3}$ ²	$\sim 7.2 \times 10^{-4b}$	101 ^b	[166]
NiPc-Cu	thick film	1 ppm	~397%	>10	Irrev.	$0.13-1 \times 10^{-3}$ ²	$\sim\!\!1.4\times10^{-2b}$	284	[166]

^d two probe thin film, irrev. is irreversible.

sensing properties toward SO_2 at 150 °C in Ar ($R_{10ppm} = 21.6\%$, Fig. 16c and d) [147].

The above works indicate that MOFs are rather promising to be chemiresistive gas sensing materials with specific selectivity. However, since their large bandgap generates insulating behavior at room temperature, MOF fail to provide enough thermal energy to activate charge carriers. Consequently, the heating component is still needed.

3.1.2. Neat MOFs for room temperature chemiresistive gas sensing

There are two methods to realize the required activity of neat MOFs for room temperature (RT) chemiresistive sensing. One is replacing thermal energy by photo energy for photo-active MOFs, the other is the intrinsic active properties based on redox-active ligands and their good orbital overlapping with metal nodes. While the former method can effectively realize excellent RT sensing activity, additional photo energy supplying components should

a two probe pellet,

^b four probe,

c van der Pauw

Table 3
Room-temperature gas-sensing properties toward H_2S of various chemiresistive gas sensors working at RT. (1. Experimental LOD, 2. IUPAC method, 3. 3RMS with simulated equation, 4. 10% response).

Material	Structure	Conc.	R	t _{res} /min	t _{rec} /min	LOD/ppm	σ /s cm $^{-1}$	$BET/m^2 g^{-1}$	Refs.
Cu ₃ (HHTP) ₂	thick film	80 ppm	~0.5%	N.A.	N.A.	2 ¹	0.002 ^a [149]	540 [265]	[150]
Ni ₃ (HHTP) ₂	thick film	80 ppm	~4.2%	N.A.	Irrev.	2^1	0.1 ^a [266]	N.A.	[150]
Ni ₃ (HHTP) ₂	thick film	80 ppm	~98%	N.A.	Irrev.	0.23^{2}	0.1 ^a [266]	N.A.	[151]
Ni ₃ HITP ₂	thick film	10 ppm	~97%	N.A.	Irrev.	0.52^{2}	2^{a} , 40^{c}	690	[151]
NiPc-Ni	thick film	80 ppm	~68%	~5	Irrev.	$0.002 - 0.032^2$	$\sim 7.2 \times 10^{-4b}$	101	[166]
NiPc-Cu	thick film	80 ppm	~100%	~3	Irrev.	$0.001-0.018^2$	$\sim\!1.4\times10^{-2b}$	284	[166]
ZnO@ZIF-8	thin film	10 ppm	52.1%	7	>10	0.05^{1}	N.A.	145.5	[208]

^d two probe thin film, irrev. is irreversible.

c van der Pauw.

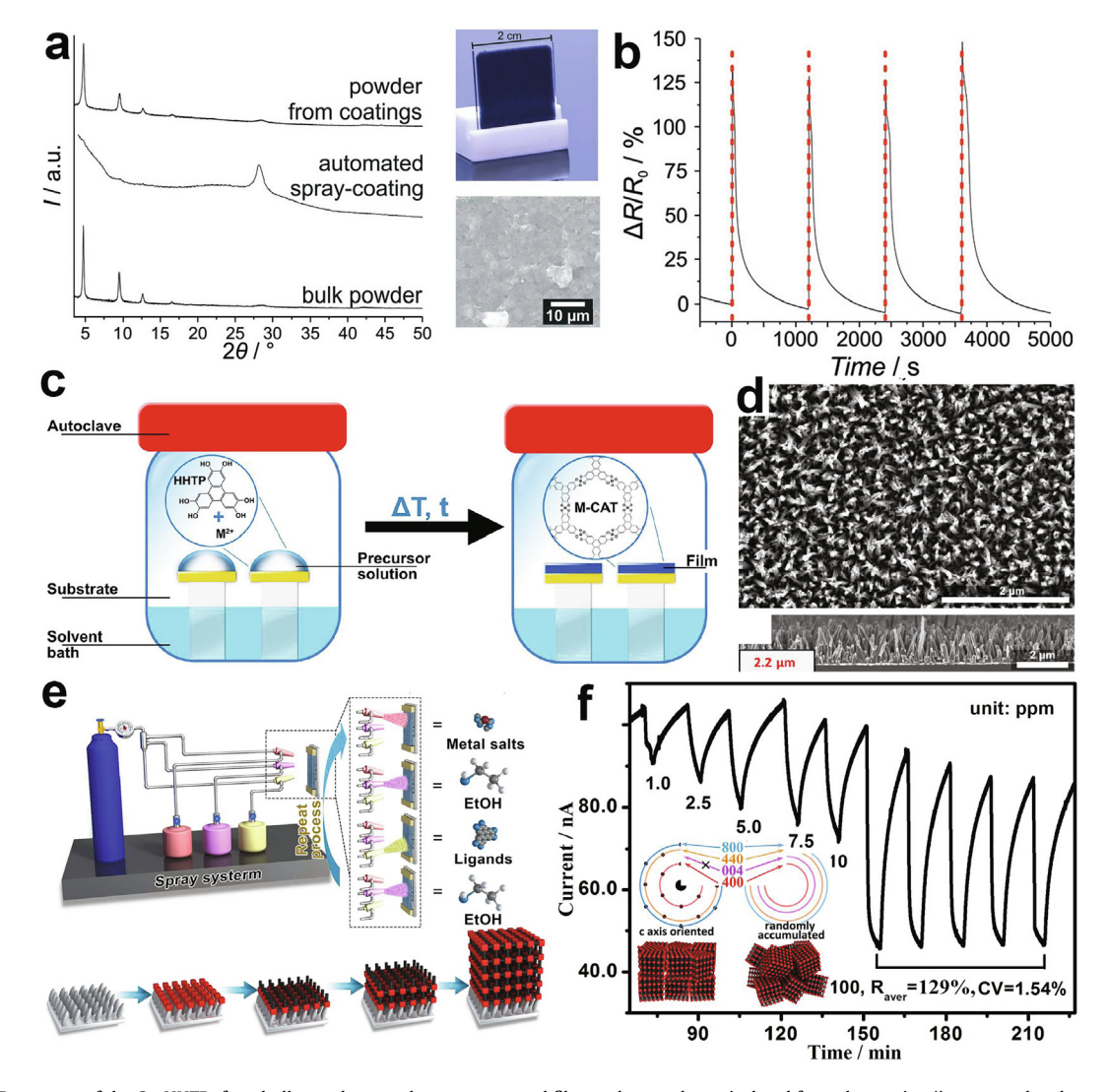


Fig. 19. (a) PXRD patterns of the Cu₃HHTP₂ for a bulk powder sample, a spray-coated film, and a powder re-isolated from the coating (insets are the photography of a spray-coated layer and the SEM image of the surface of the coating. (b) Response-recovery curve toward methanol. The red line represents the injection time points. Reproduced with permission [158]. Copyright 2018, The Royal Society of Chemistry. (c) Scheme of the vapor-assisted conversion (VAC) setup. (d) Top-view and cross-section SEM micrographs of Cu₃HHTP₂films, respectively. Reproduced with permission [159]. Copyright 2019, American Chemical Society. (e) Illustration of the preparation of Cu₃HHTP₂ thin-film gas sensors, and the corresponding (f) Measured changes of current of the MOF film sensor towards NH₃ with various concentrations. The inset showed the simulated SAED patterns of oriented and disordered MOF films. Reproduced with permission [162]. Copyright 2017, Wiley-VCH Verlag GmbH & Co. KGaA, Weinheim.

be taken into consideration. As to the latter method, the promising overall high performances are shown by cascading sensitivity, selectivity and room working temperature into a single device free of heating components.

Since the stable and porous EC-MOFs, Cu[Cu(pdt)₂] (pdt = 2,3-pyrazinedithiolate), synthesized by H. Kitagawa *et al* in 2009 [148], dozens of porous EC-MOFs have been developed, with excellent electrical properties [2], In 2015, the EC-MOF chemiresistive

a two probe pellet,

^b four probe,

Table 4Room-temperature gas-sensing properties toward other gases of various chemiresistive gas sensors working at RT. (1. Experimental LOD, 2. IUPAC method, 3. 3RMS with simulated equation, 4. 10% response).

Material	Structure	Conc.	R	t _{res} /min	t _{rec} /min	LOD/ppm	$\sigma/\mathrm{s}~\mathrm{cm}^{-1}$	$BET/m^2 g^{-1}$	Refs.
Cu₃HHTP₂	thin film	saturated Methanol water	~140% ~370%	N.A.	N.A.	N.A.	0.002 ^a [149]	540[265]	[158]
Cu ₃ HHTP ₂	thick film	Methanol 200 ppm	~9%	N.A.	N.A.	N.A.	0.002 ^a [149]	540[265]	[149]
Cu ₃ HITP ₂	thick film	Methanol 200 ppm	~1.8%	N.A.	N.A.	N.A.	0.2 ^a [149]	N.A.	[149]
Ni ₃ HITP ₂	thick film	Methanol 200 ppm	~4%	N.A.	N.A.	N.A.	2^a , 40^c	690	[149]
Cu ₃ (HHTP) ₂	thin film	Methanol 100 ppm	~30%	N.A.	N.A.	N.A.	0.02 ^d	N.A.	[162]
ZIF-8/MWCNT/AgNPs	thick film	Methanol 10000 ppm	~8.05%	<2	<0.1	18470 ²	N.A.	1176	[197]
ZnO@ZIF-8@POM	thick film light	methanol 100 ppm	72%	N.A.	N.A.	N.A.	N.A.	432.4	[210]
ZIF 8/MWCNT/AgNPs	thick film	ethanol 10000 ppm	~12.16%	<2	<0.1	3990^{2}	N.A.	1176	[197]
Cu ₃ HHTP ₂	thick film	ethanol 200 ppm	~2.3%	N.A.	N.A.	N.A.	0.002 ^a [149]	540[265]	[149]
Cu ₃ HITP ₂	thick film	ethanol 200 ppm	~0.8%	N.A.	N.A.	N.A.	0.2 ^a [149]	N.A.	[149]
Ni ₃ HITP ₂	thick film	ethanol 200 ppm	~4%	N.A.	N.A.	N.A.	2^a , 40^c	690	[149]
Cu ₃ (HHTP) ₂	thin film	ethanol 100 ppm	~40%	N.A.	N.A.	N.A.	0.02 ^d	N.A.	[162]
Cu-HHTP-THQ	thick film	ethanol 533 ppm	~10%	N.A.	N.A.	N.A.	$\sim\!\!2.5\times10^{-5a}$	441.2	[168]
nO@ZIF-8@POM	thick film light	ethanol 100 ppm	~30%	N.A.	N.A.	N.A.	N.A.	432.4	[210]
Cu[Ni(pdt) ₂]	pellet	Acetylene 72 ppm	~0.5%	N.A.	N.A.	N.A.	2.6×10^{-6a}	426	[167]
$MIL\text{-}101(Cr)\supsetPEDOT$	pellet	NO ₂ 1/10 ppm	~4%/46%	0.5-2.5	Irrev.	0.06^{2}	$10^{-8} - 10^{-3a}$	803-3100	[178]
Pd/ZIF-8	Thick film	H ₂ 10000 ppm	~3.5%	~0.12	~0.17	$\sim 600^2$	N.A.	N.A.	[182]
Au/ZIF-8	Thick film	NO ₂ 1/10 ppm	~4%/46%	~0.12	>10	$\sim 0.19^{2}$	N.A.	1164.5	[196]

^b four probe,

gas sensor based on $\text{Cu}_3(\text{HITP})_2$ (HITP = 2, 3, 6, 7, 10, 11-hexaiminotriphenylene, 0.2 S cm⁻¹, pellet, two-probe) was successfully fabricated by the cooperation of Dincă and Swager's groups (Fig. 17a) [22]. The thick film of $\text{Cu}_3(\text{HITP})_2$ chemiresistor shows reversible p-type sensing behaviors, that is, decreased conductivity (~3%) toward 10 ppm reducing gas NH₃, with an experimental LOD of 0.5 ppm (Fig. 17b, Table 1).

The isostructural Ni₃(HITP)₂ chemiresistor, with high conductivity of 2 S cm⁻¹ (pellet, two-probe), failed to respond to NH₃, signifying the direct influence of rational synthetic variation of EC-MOFs on functionality like chemiresistive sensing. Based on it, they subsequently and systematically studied the discrimination between different categories of VOCs of chemiresistive gas sensor arrays consisted of a family of structurally analogous 2D MOFs constructed by the ligands of HHTP (2,3,6,7,10,11-hexahydroxytriphe nylene) or HITP, and metal centers of Cu or Ni (Fig. 17c) [149]. The corresponding results indicate that multiple sensing mechanisms are operative with high degrees of orthogonality, which can discriminate different categories of VOCs by PCA method (Fig. 17d). Such works reveal that rational designing of the MOF's chemical and electronic structures can be an effective method to improve sensor materials with selective detection and identification.

To overcome the poor grain contacts in the thick film, Mirica's group later reported the direct growth of $\text{Cu}_3(\text{HHTP})_2$ and $\text{Ni}_3(\text{-HHTP})_2$ nanorods on shrinkable polymeric films equipped with

miniaturized graphitic electrodes (Fig. 18a) [150]. According to the results, the high response and reversal conductivity change toward oxidizing gas NO are predicted, and Ni centers were expected to be more favorable for sensing of H₂S (Tables 1-3). For better electrical contact, they changed the substrate to textiles, on which two Ni-based EC-MOFs, Ni₃(HHTP)₂ and Ni₃(HITP)₂ are directly grown. Thus, it is called self-organized frameworks on textiles (SOFT, Fig. 18b) [151]. The Ni₃(HHTP)₂ and Ni₃(HITP)₂ showed high response toward both NO and H₂S, with a LOD down to the sub-ppm level. It is interesting to observe opposite responses of two different sensors toward NO (Fig. 18c), indicating that besides charge transfer, MOF-NO interaction induced n/p type doping depending on energy states of the EC-MOFs may contribute to the resistance changes. While both sensors show irreversibility toward NO or H₂S, they can be recovered simply by water washing. Anti-humidity tests showed that the sensors can work reliably up to 18 RH%.

Through the direct growth method, both the large grain size and bad grain contact hinder the effective transport of the electron and the mass in aforementioned electrical devices with powders, thick films or loosely interconnected nanocrystals. Further improvement of the performances of these devices requires the high-quality EC-MOF thin film [152–156]. The significance of the MOF thin film has boosted the development of plentiful different strategies for fabricating it on solid substrates [157], including top-down and bottom-up methods.

a two probe pellet

c van der Pauw.

d two probe thin film, irrev. is irreversible.

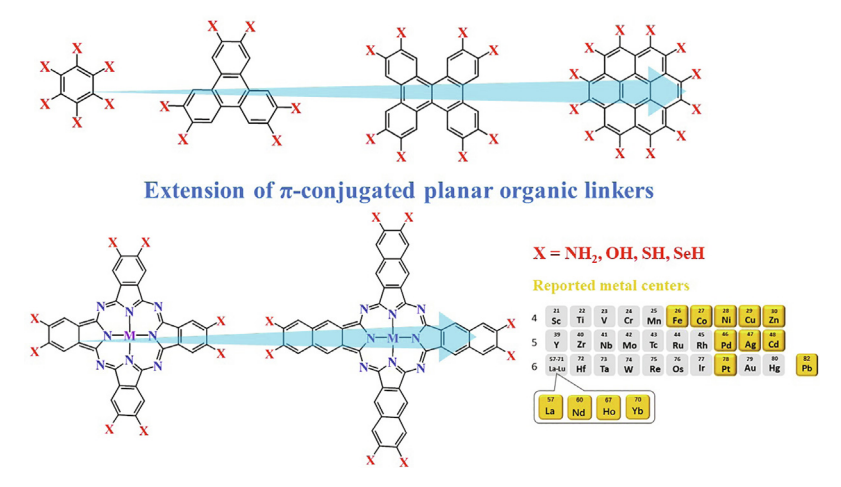


Fig. 20. Typical organic linkers and metal centers in conductive MOFs with planar multidentate linkers. Reproduced with permission [42]. Copyright 2020, Elsevier.

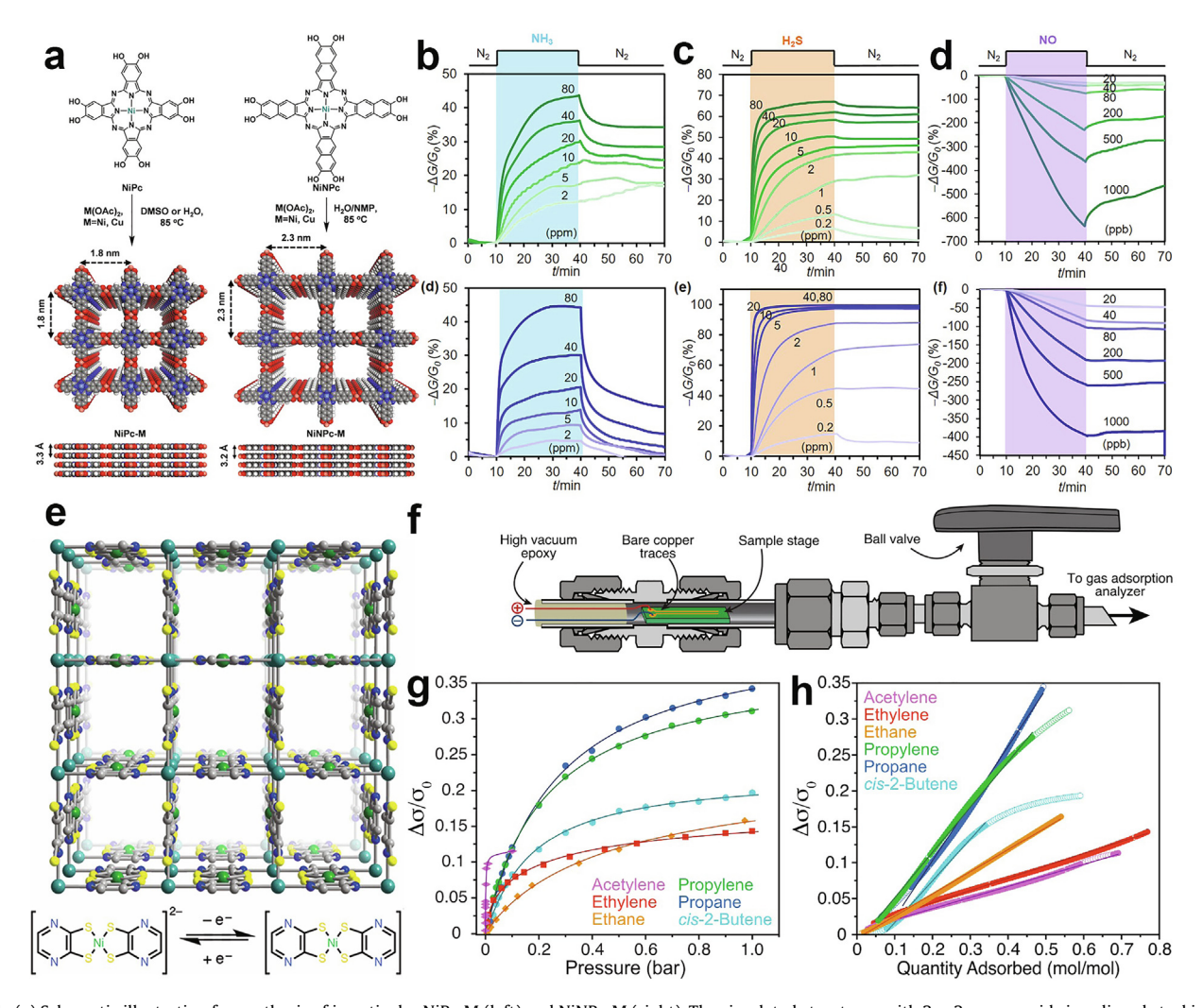


Fig. 21. (a) Schematic illustration for synthesis of isoreticular NiPc-M (left) and NiNPc-M (right). The simulated structures with 2×2 square grids in eclipsed stacking mode from top and side view. Chemiresistive response of NiPc-Ni MOF (top) and NiPc-Cu MOF (bottom) to (b) NH₃, (c) H₂S, and (d) NO at different concentrations. Reproduced with permission [166]. Copyright 2018, American Chemical Society. (e) Single crystal structure of $Cu[Ni(pdt)_2]$ with one-dimensional pore channel and three dimensional structure. The bottom showed its redox-active NiS₄ unit. The Cu, Ni, S, N, and C atoms are represented in teal, green, yellow, blue, and gray spheres, respectively. The hydrogen atoms are omitted for clarity. (f) The conductivity testing cell utilized for in situ conductance measurements on a gas adsorption analyzer. (g) Room temperature conductivity isotherms as a function of absolute pressure for acetylene (purple diamonds), ethylene (red squares), ethane (orange diamonds), propylene (green circles), propane (blue circles), and cis-2-butene (teal circles). (h) Conductivity-composition profiles of different gaseous. Reproduced with permission [167]. Copyright 2019, American Chemical Society.

For example, Cu₃HHTP₂ ultrathin nanosheets (<10 nm) were fabricated firstly and then assembled into thin film by spray method (Fig. 19a) [158]. The corresponding chemiresistor showed 370% and ~140% of resistance change toward saturated water and methanol, respectively (Fig. 19b, Table 4). T. Bein, D. Medina and their co-workers developed the vapor-assisted conversion (VAC) method for the in-situ growth of EC-MOFs on various substrates (Fig. 19c) [159]. The substrates are fixed on top of the glass spacers above the solvent bath in a sealed reaction container, on which a precursor liquid layer comprising the redox-active organic linker (HHTP), metal precursor (M^{II} = Ni^{II}, Co^{II}, or Cu^{II}), and further additives like modulators is deposited. After the sealed vessel is then heated for the adjusted time, the liquid precursor layer is converted into a thin film of EC-MOFs covering the whole surface (Fig. 19d), the sensor application of which is not reported in their work. Another effective method to fabricate MOF thin film is the Laver-by-Laver (LbL) method [160,161].

M. Yao, G. Xu and their co-workers firstly reported the controlled preparation of the high quality thin film of EC-MOF on -OH functionalized substrates with the spray LbL assembly method (Fig. 19e) [162]. The prepared Cu₃HHTP₂ thin films possess good crystallinity, high orientation, large crystal domain size, dense packing, smooth surface and well controlled thickness, which are indicated by the RT sensing measurements to have p-type semiconductor behaviors. Moreover, compared with other chemiresistor sensors working at room temperature, the thin film with 20 nm thickness exhibited selectively ultrahigh response to NH₃ ($R_{100 \text{ ppm}}$ = 129%, Fig. 19f) among 12 typical interference gas (SO₂, acetone, butanone, benzene, toluene, ethylbenzene, CO, H2, CH4, etc.), as well as fast response speed of 1.36 min, noticeable stability and excellent reproducibility with 88.4% response retention after 3 months. The up-shift of Fermi level of Cu₃HHTP₂ upon exposure to NH₃ was observed by ultraviolet photoelectron spectroscopy (UPS) measurements, similar to an ntype doping in a p-type semiconductor.

Besides metal nodes and active film architecture, designs of size, functional groups and shapes on redox-active ligands can significantly affect the sensing performances (Fig. 20) [42]. Functional group effects can be found in Dincă and Mirica's works mentioned above (Figs. 17 and 18). Based on the typical the square-planar building unit, MX₄, the trigonal ligand can be replaced by square ligands to construct new 2D EC-MOFs [163–166]. Such square ligands based 2D EC-MOFs can be applied as active materials for chemiresistors.

For instance, Mirica's group used two square ligands to synthesize isoreticular phthalocyanine and naphthalocyanine-based MOFs (Fig. 21a) [166]. Simulations showed that both EC-MOFs are consistent with the P4/mmm space group with eclipsed cofacial AA-stacking mode. The conductivity of NiPc-M (M = Ni or Cu, 10^{-4} – 10^{-2} S cm $^{-1}$) is lower than that of NiNPc-M (M = Ni or Cu), while their BET surface areas are similar to each other (101–284 m 2 g $^{-1}$). Fig. 21b–d indicate that NiPc-Cu and NiPc-Ni have reversible responses toward NH $_3$ and H $_2$ S/NO, respectively. Moreover, LOD values of them toward NH $_3$ are in the sub-ppm level

(Tables 1–3). Interestingly, their work provides a chance to gain an insight into the possible sensing mechanism of these materials by XPS and EPR. Briefly, the reduction/oxidation of ligands and/or metals, and the reduction/enhancement of the unpaired radicals are observed by interaction of the MOF with reducing gas (H₂S)/oxidizing gas (NO). Both changes are essential factors determining the conductivity of an EC-MOF, which may contribute to further experimental and computational works on sensing mechanisms of 2D EC-MOFs.

The square ligand can be shortened to 2,3-pyrazinedithiolate (pdt). Due to the formation of two different square-planar building units of MX₄, the final coordination network, Cu[Ni(pdt)₂], shows a 3D framework constructed by sulfur coordinated square planar nickel(II) pyrazine-2,3-dithiolate units (NiS₄) linked by nitrogencoordinated square planar copper(II) centers (CuN₄) (Fig. 21e) [167], similar to that of Cu[Cu(pdt)₂. By using a homemade instrument for in situ conductance measurements on a gas adsorption analyzer (Fig. 21f), J. R. Long's group successfully obtained the insitu conductivity-adsorption data on an ohmic contact of the MOF pellet with electrodes. After converting to resistance changes, the response *vs.* pressure curves can be acquired (Fig. 21g and Table 4). Calculated by Fig. 21g and absorption capacity at different pressure, the curves of response *vs.* quantity of adsorbed gas molecules demonstrate good linearity for almost all gas (Fig. 21h).

Based on the single redox-active organic ligand systems, above works can be further extended to the dual redox-active organic ligand systems to possibly provide more choices on conductivity, topology and functions. By the proper choice of the binary trigonal organic linkers, the electron transport in "through-bond" or "through-space" pathways can be effectively modulated, which varies their conductivity and porosity via electron delocalization efficiency and channel shapes, respectively. Accordingly, M. Yao, S. Kitagawa and coworkers reported a novel 2D π -conjugation EC-PCP, Cu₃(HHTP)(THQ) (THQ = tetrahydroxy-1,4-quinone), with regular trigonal crystal structure constructed by uniform hybrid of two trigonal organic ligands (Fig. 22a) [168]. Because of the strong chelation between Cu^{II} and ethylenediamine (en), en has been chosen as the modulator to balance the coordination capability of HHTP and THQ with Cu^{II} via a competing bond formation mechanism. The dramatically modulated electronic conductivity $(\sim 2.53 \times 10^{-5} \text{ S cm}^{-1})$ and high porosity (with BET value of ~441.2 m² g⁻¹) of Cu₃(HHTP)(THQ) nanowires provide the low conductivity baseline and highly accessible areas, facilitating the outstanding room temperature chemiresistive sensing properties. The corresonding thick film sensor presented noticeable discrimination to low concentration of NH₃ with fast speed and distinguished LOD down to $\sim 0.02 - 0.35$ ppm.

$3.1.3.\ MOF-on-MOFs\ for\ chemiresistive\ gas\ sensing$

Proposed by S. Furukawa, O. Sakata, and S. Kitagawa in 2008 and 2009 for the core-shell single crystal or sandwich-type A-B-A MOFs (Fig. 23a) [169,170], such a concept of MOF-on-MOF or

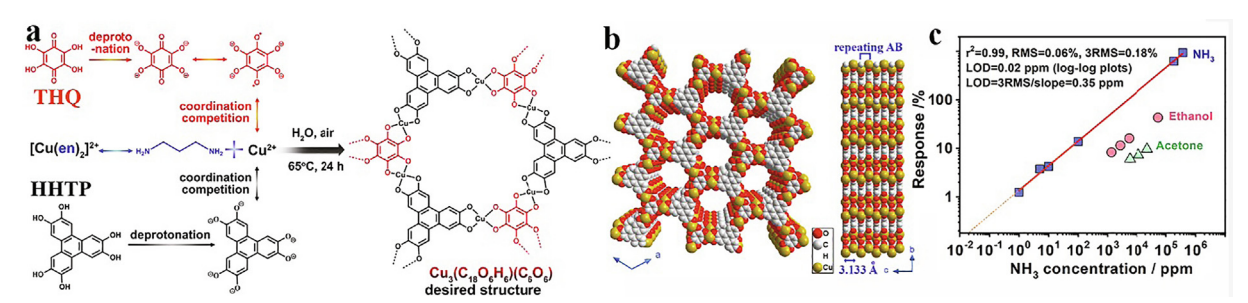


Fig. 22. (a) Schematic illustration of the synthesis of the dual-ligand Cu₃(HHTP)(THQ); (b) the simulated crystal structure presented in space filling model; and (c) room temperature response-concentration log–log plots toward NH₃. Reproduced with permission [168]. Copyright 2020, Wiley-VCH Verlag GmbH & Co. KGaA, Weinheim.

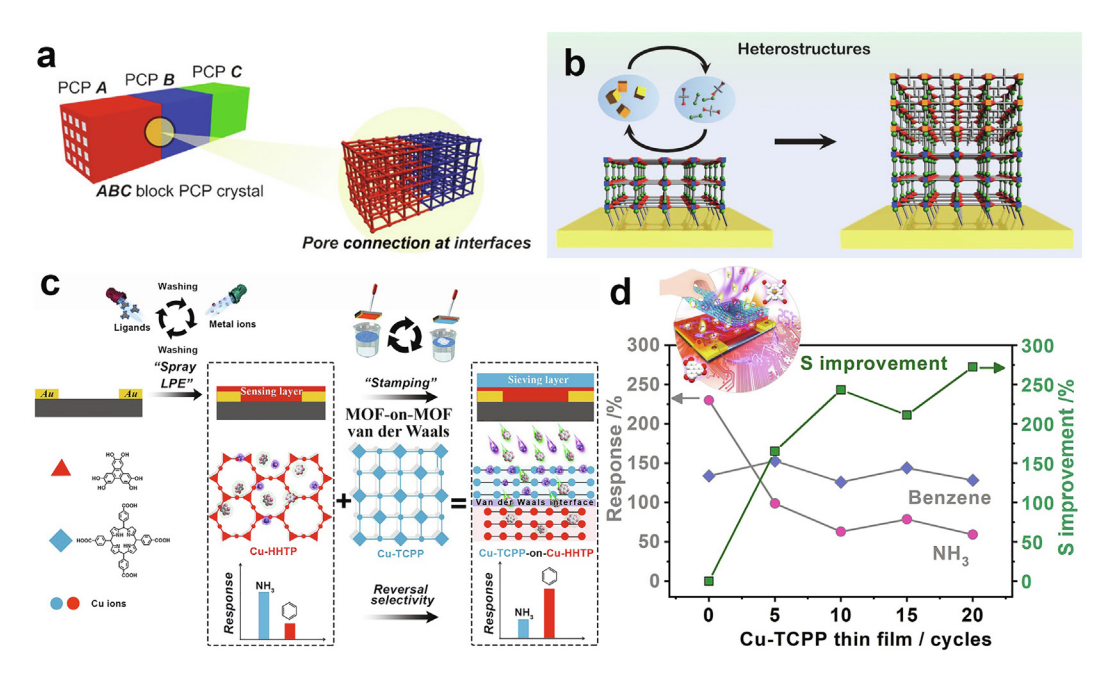


Fig. 23. (a) Schematic illustration of the block PCP concept, that is, MOF-on-MOF or PCP-on-PCP. Reproduced with permission [169]. Copyright 2009, Wiley-VCH Verlag GmbH & Co. KGaA, Weinheim. (b) Schematic illustration of LbL growth experiments of MOF-on-MOF thin films on SAMs functionalized substrates. Reproduced with permission [173]. Copyright 2011, Wiley-VCH Verlag GmbH & Co. KGaA, Weinheim. (c) Illustration of the preparation of Vdw MOF-on-MOF thin films, and (d) selectivity improvements of Cu-TCPP-xC-on-Cu-HHTP-20C (x = 0, 5, 10, 15 and 20, inset is a schematic illustration of the selective detection mechanism of the chemiresistive sensor working at RT). Reproduced with permission [58]. Copyright 2019, Wiley-VCH Verlag GmbH & Co. KGaA, Weinheim.

PCP-on-PCP was predicted by C. Wöll's group in 2009 to be used for MOF-on-MOF thin films [171]. At the same time in 2011 (Fig. 23b), it was realized by the successful fabrications of hetero-structured MOF thin films or hetero-structured Sur-MOFs, reported by groups including O. Shekhah, C. Wöll, R. A. Fischer, S. Furukawa, and S. Kitagawa [172,173].

With the potential to cascade various characteristics of different MOF layers in sequence to integrate multifunctions that can not be acquired by single MOF layers [174–177], hetero-structured MOF-on-MOF thin films typically require one-to-one coordination bonding at the interface, less lattice mismatch and similar topology, which limits the preparation of the MOF hetero-structure with distinct crystal structures in different MOF layers.

The van der Waals integration method, which can overcome the limits on lattice matching and topology similarity, was utilized by G. Xu's group to deposit molecular sieving MOFlayer (Cu-TCPP, TCPP = 5, 10, 15, 20-tetrakis (4-carboxyphenyl) porphyrin) onto semiconductive MOF layers (Cu-HHTP) to get highly oriented MOF-on-MOF thin films (Fig. 23c) [58]. By this means, the functions in both MOF layers have been cascaded in the proper order to synergistically produce an enhanced device performance. Cu-TCPP-on-Cu-HHTP not only realized high response to benzene ($R_{100\ ppm}$, 153%), but also reversed the selectivity of Cu-HHTP toward benzene and its strongly interfering molecule, NH₃ (Fig. 23d). Further PCA treated data collected with Cu-TCPP-xC-on-Cu-HHTP-20C showed well discriminability of 5 typical human breath biomarkers (NH₃, benzene, hexane, carbon monoxide and acetone).

3.2. MOFs as functional materials in composites for chemiresistive gas sensors

3.2.1. MOFs-polymer or MOFs-organic molecule composites

Composites incorporating MOFs within polymeric matrices have potential as functional components for several technologies. MOFs-polymer composites used as chemiresistive gas sensing materials, instead of high-performance gas separation membranes

[45], are encountered with challenges of poor conductivity and insufficiency of sensing activity. Accordingly, a hybrid method combining both high-porosity MOFs and sensing activity of the conducting polymer has been developed for MOFs-polymer composites based chemiresistors. For example, S. Kitagawa, T. Uemura and their coworkers reported a facile method to obtain a series of conductive MOFs-polymer composites by the controlled polymerization of certain amounts of 3,4-ethylenedioxythiophene (EDOT) in the cavities of the host framework of MIL-101(Cr) (Fig. 24a) [178], a famous stable and highly porous sub-family MOFs developed by G. Férey's group in 2005 [179]. The obtained MIL-101(C $(x) \supset PEDOT(x)$, where x is the mass fraction of PEDOT in the composite (determined from the S/Cr ratio by XRF), showed a reasonable electronic conductivity (x = 57, $1.1 \times 10^{-3} \text{ S cm}^{-1}$) while maintaining high porosity (x = 57, BET, 803 m 2 g $^{-1}$, Fig. 24b). The conductivity of PEDOT, a p-type semiconductor can be modified by the presence of oxidizing analytes due to the shift of its Fermi level, which can be used for chemiresistors. Compared with low sensitivity of pristine PEDOT sensor (BET, 2 m² g⁻¹, R_{10} $_{\rm ppm}$ = 0.8%), MIL-101(Cr) \supset PEDOT (45) showed 23 times higher sensitivity toward NO₂ due to the highly accessible surface areas (BET, 1038 m² g⁻¹, $R_{10 \text{ ppm}}$ = 46%, Fig. 24c). Also, LOD value of ~60 ppb was estimated from linear relationship of response vs. concentration points.

Inspired by the pioneer work on the TCNQ@HKUST-1 conductive composite (7, 7, 8, 8-tetracyanoquinodimethane), the organic semiconductor tetrathiafulvalene (TTF) was introduced to Co-MOF-74 to form the Guest@MOF type MOFs-organic molecule composites by I. Strauss and J. Caro (Fig. 24d) [180,181]. Compared with Co-MOF-74, the obtained Co-MOF-74-TTF nanocomposite exhibited increased electrical conductivity but diminished CO₂ adsorption because part of the blockage of its partial pores by infiltrating TTF (Fig. 24e). Primary results of the conductivity change upon exposure to different gas are reported, from which slight differences can be observed but further improvement is still in need (Fig. 24f).

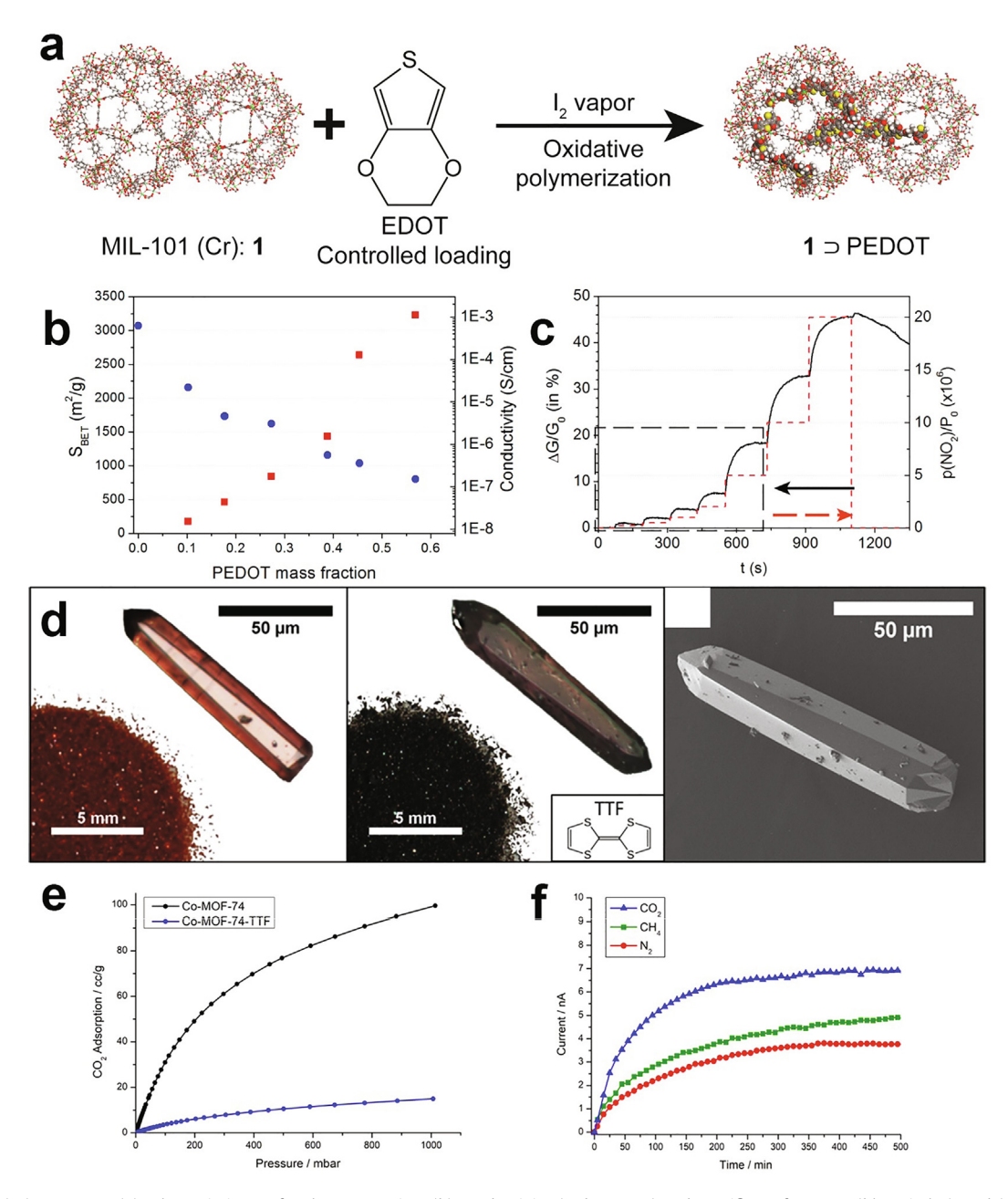


Fig. 24. MIL- $101(Cr) \supset PEDOT$: (a) schematic image for the preparation, (b) conductivity (red squares) and specific surface area (blue circles), and (c) time-dependent variations of conductivity of a chemiresistive sensor prepared using MIL- $101(Cr) \supset PEDOT$ (45) (plain line, left axis) under different partial pressures of NO_2 (dashed, right axis). Reproduced with permission [178]. Copyright 2016, American Chemical Society. (d) The optical images of Co-MOF-74 (left) and Co-MOF-74-TTF (middle) with morphologies of powder and single crystals, and the SEM image of Co-MOF-74-TTF (right); (e) CO_2 adsorption isotherms of the pristine Co-MOF-74 and the composite Co-MOF-74-TTF at 25 °C; and (f) long-term conductivity measurements of Co-MOF-74-TTF under N_2 , CH_4 , and CO_2 atmospheres with a bias of 10 V. The atmosphere was changed from vacuum to $N_2/CH_4/CO_2$ at 0 min. Reproduced with permission [180]. Copyright 2019, American Chemical Society.

3.2.2. MOFs-metals composites

MOFs-metal composites are popularly applied as high-performance catalysts owing to their unique combination of high surface areas, catalytic effects, size-narrowed distribution, *etc.* As for chemiresistor, the most representative example is the Pd/ZIF composites combining selective and sensitive Pd nanowires with the molecule sieving MOF [182]. The selective detection of Pd toward $\rm H_2$ is relying on the specific resistance change resulted from the formation of a solid solution of Pd/H (α -phase) or palladium hydride (β -phase). As of the first example on Pd-Ni alloy reported by Hughes and Schubert [183], thin films [184], nanodots [185], mesowires [186], nanotubes [187], and specific patterns [188] of Pd have been developed to reach the selective and sensi-

tive detection of H_2 . Among them, the high surface area and the well-formed interconnection of Pd nanotubes enabled highly sensitive response toward H_2 at RT ($R_{1000~ppm} = 1000\%$), while showing a response time of ~3.17 min due to slower speed of Pd/H (α -phase) comparision with that of β -phase occurred in the range of 1–2% at RT [189]. ZIF-8/MAF-4 is a subfamily of MOFs with excellent chemical and thermal stability, as well as flexible channels for gas adsorption and separation [190,191]. Accordingly, I.-D. Kim's group and R. M. Penner's group fabricated Pd/ZIF-8 NW bilayered thick film (Fig. 25a) [182]. Interestingly, the acceleration effect of highly porous ZIF-8 gives rise to excellent response (~0.22 min) and recovery speed (~0.10 min) of Pd/ZIF-8 sensors toward 1000 ppm of H_2 . In addition, the micropores (0.34 nm) of ZIF-8

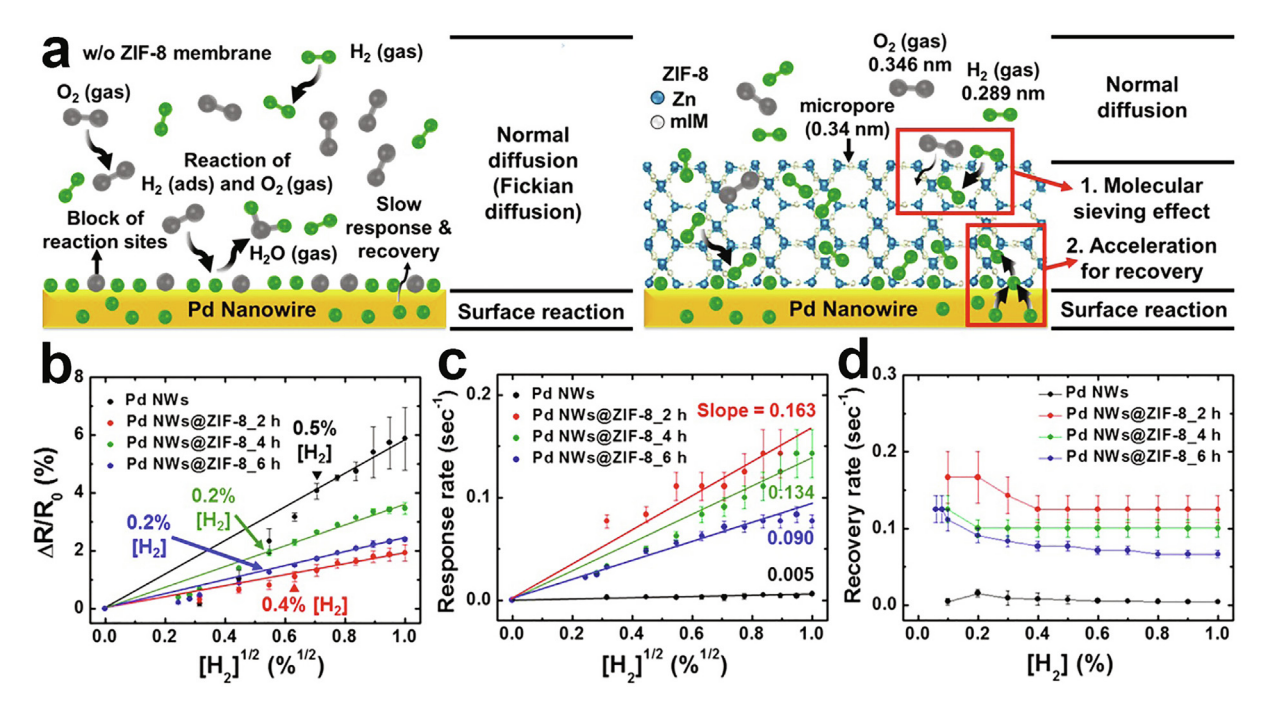


Fig. 25. (a) Sensing model for Pd NWs without ZIF-8 membrane and Pd NWs/ZIF-8. (b) Response versus $[H_2^{1/2}]$ in air, (c) response rate versus $[H_2^{1/2}]$ in air, and (d) recovery rate versus $[H_2]$. Reproduced with permission [182]. Copyright 2017, American Chemical Society.

can act as a molecule sieving layer from the viewpoints of kinetic factors. The kinetic diameter difference between H_2 (0.298 nm) and interfering O_2 (0.346 nm) significantly facilitates the faster diffusion of H_2 than O_2 in ZIF-8. However, it should be noted that, ZIF-8 cannot separate gaswith the kinetic diameter smaller than 0.7 nm from the viewpoint of thermodynamic factors because the flexibility of its framework [192,193]. Some related works on MOF-metal composites such as Pt@Cu-HHTP and Au@ZnO@ZIF-8 were also designed for the detection of other gaseous NO_2 and HCHO [194–196], respectively. Assisted by visible light irradiation, the Au@ZnO@ZIF-8 sensor with catalytic Au and porous MOF shell showed not only selective response to HCHO, but also good anti-interference properties against gases like H_2O and toluene.

3.2.3. MOFs-carbon composites

Carbon materials are a class of crystalline or amorphous materials with excellent conductivity ranging from semiconductor to conductor. They can be adopted as the host materials or additives to facilitate the charge transfer and transport with MOFs, which can thus change the conductivity and sensing activity of the MOFs-carbon composites [197].

A typical example is to use HKUST-1 ($Cu_3(BTC)_2$ (BTC = benzene tricarboxylic) [198], as the gas concentration component in chemiresistive graphene oxide (GO) or aminated GO (GOU) [199]. The resultant HKUST-1/GO (25 wt% of GO) showed reversible response towards NH₃ at room temperature ($R_{100ppm} = 4\%$, Fig. 26a and b), as along with the high Brunauer-Emmett-Teller (BET) surface areas of 916 m² g⁻¹. Additionally, systematic studies also confirm that, the chemical bonding of HKUST-1 with GO facilitates the reduced acidity of GO, effective analyte-material interaction and the subsequent charge transfer. The chemiresistive properties of HKUST-1/GO were attributed to the collapse of MOF (Fig. 26c).

Another example of MOFs-carbon composites is using EC-MOFs as sensing materials, while carbon materials as the enhanced additives for charge transfer and transport. H. Deng's group deposited polycrystalline Ni₃(HHTP)₂ on single-layer graphene (G) to obtain

a transparent chemiresistor with an electrical conductivity up to 4.0×10^4 S m⁻¹ (two probes, thin film; transparency, 95.7%; Fig. 26d) [200]. The Ni₃(HHTP)₂/G sensor can detect NH₃ in the range of 0.01–500 ppm at RT (Fig. 26e). The response-concetration plots follow well with the first-order kinetic. Besides, a heterojunction structure between G and Ni₃(HHTP)₂ (thickness, 15 nm) was fabricated to study the electron transfer mechanism as shown in Fig. 26f. The Kelvin probe force microscope (KPFM) and Raman spectra revealed the possible electron charge transfer scheme, as illustrated in the lower part of Fig. 26f. Upon contacting, the electrons moved from Ni₃(HHTP)₂ to the p-doped G until they reached an equilibrium at the Fermi level. The introduced NH₃ molecules mainly interacted with Ni₃(HHTP)₂, which transferred more electrons to G and thus increased the resistance.

3.2.4. MOFs-metal oxides composites

Metal oxides (MO_{Xs}) semiconducting materials, such as ZnO, SnO_2 , In_2O_3 and WO_3 , have aroused extensively interests in the field of chemiresistive gas sensor. Due to the low cost, portability, real-time operability and ease of operation, the MOx-based gas sensor has been used in numerous industrial and domestic applications on detecting gaseous analytes, including fields of medical care, food industry, environment monitoring, public security affairs, and agricultural production. However, lack of selectivity and relatively high working temperature are still the notable bottlenecks that limit the further applications of MO_X sensors.

To address the above-mentioned issues, plenty of research has been conducted to enhance the performance of chemiresistive gas sensor on detecting gaseous analytes by coating ZIFs/MAFs onto MOx to form core-sheath or core-shell architectures in the form of either thin films or powders [192,201–208]. These works indicate that, the construction of MO_X@MOF core-sheath/shell architectures is a promising material design strategy for high perfomance chemiresistors by combining the high sensitivity of MOx with the excellent selectivity, catalytic effects and additional functions of MOFs. As for powders used in thick film sensor, ZnO@ZIF-8 core-sheath NRs were prepared according to the hydrothermal

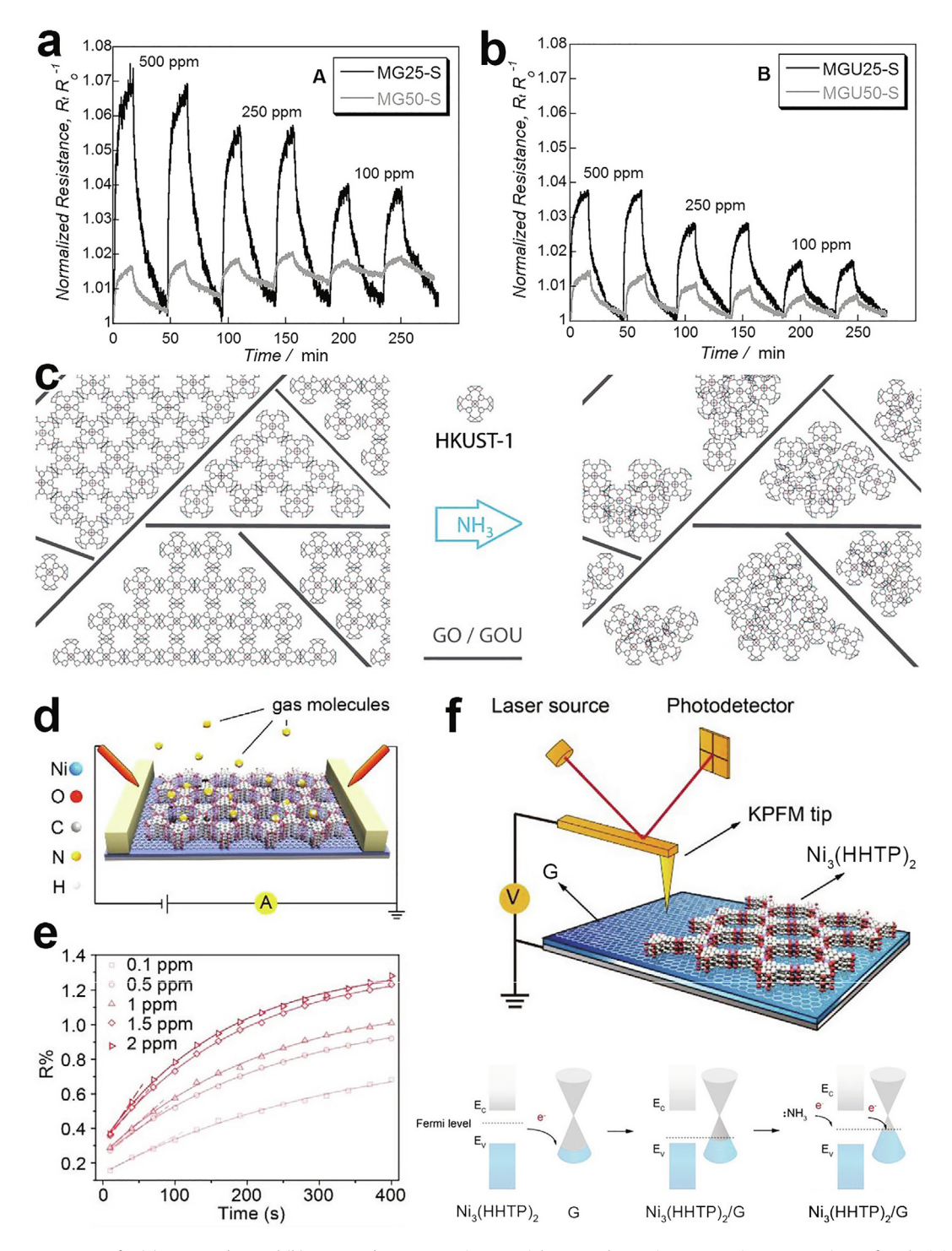


Fig. 26. Typical response curves for (a) HKUST-1/GO and (b) HKUST-1/GOU composite materials exposed to various ammonia concentrations, after the initial stabilization; and (c) crystal structure of HKUST-1 and changes in the texture of the hybrid materials upon exposure to NH₃. Reproduced with permission [199]. Copyright 2015, The Royal Society of Chemistry. (d) Illustration of the device composed of Ni₃(HHTP)₂/G; (e) time-resolved adsorption curves of NH₃ with different concentration detected by this device; (f) electron transfer mechanisms: illustration of the KPFM test and the band diagram of Ni₃(HHTP)₂/G and the electron transfer mechanism during ammonia adsorption. Reproduced with permission [200]. Copyright 2020, WILEY-VCH Verlag GmbH & Co. KGaA, Weinheim.

method via the self-template strategy by H. Fan's group (Fig. 27a) [201]. As a result, the chemiresistive gas sensor prepared based on the thick film of ZnO@ZIF-8 hybrids exhibited excellent sensitivity and response time towards 100 ppm formaldehyde, even with the interfering humidity (Fig. 27b).

A typical example for thin film sensor is the core-sheath MO_X@-MOFs nanowire arrays chemiresistive sensor fabricated by Yao *et al.* to detect acetone under interfering humidity, which is

achieved through coating a layer of hydrophobic and thermally catalytic ZIF-CoZn thin film onto ZnO (Fig. 27c) [192]. In addition to hydrophobic channels, the bimetallic ZIF-CoZn MOF sheaths also showed both noticeable thermal stability of ZIF-8(Zn) and outstanding thermally catalytic ability of ZIF-67(Co) on ZnO. In this work, the as-prepared ZnO@ZIF-CoZn showed good selectivity between acetone and humidity with low CV (7.4%, 0–90 RH%, Fig. 27d). Moreover, compared with the MOx sensor without

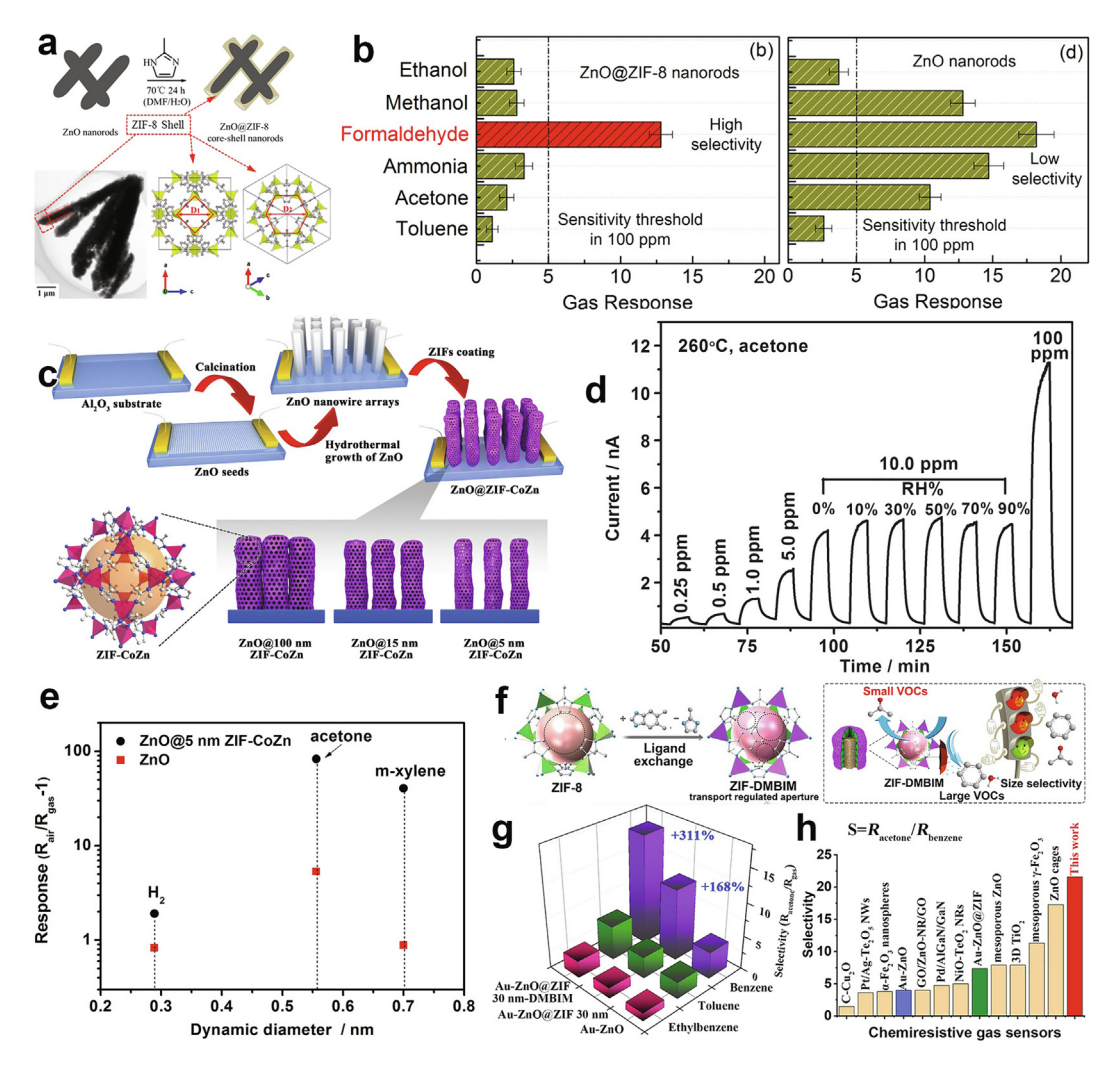


Fig. 27. (a) Schematic illustration of the ZnO@ZIF-8 NRs prepared using ZnO NRs as a template; and (b) gas sensing performance of the ZnO NRs and ZnO@ZIF-8 NRs sensor towards 100 ppm of different VOCs at 300 °C. Reproduced with permission [201]. Copyright 2016, American Chemical Society. (c) Schematic diagram of ZnO@ZIF-CoZn coresheath NWAs sensor; (d) response-recovery curves towards acetone at various concentrations in dry air and in 10 ppm acetone under different relative humidity and at 260 °C; and (e) responses of ZnO and ZnO@5 nm ZIF-CoZn to different gases (100 ppm, 260 °C). Reproduced with permission [192]. Copyright 2016, Wiley-VCH, WILEY-VCH Verlag GmbH & Co. KGaA, Weinheim. (f) Schematic illustration of the preparation of Au–ZnO@MOF; Au–ZnO@ZIF 30 nm–DMBIM: (g) selectivity comparison of acetone towards three kinds of benzene-derives anlaytes; and (d) selectivity comparison among various sensing active materials. Reproduced with permission [205]. Copyright 2019, The Royal Society of Chemistry.

MOF sheath, the prepared ZIF-CoZn MOF realized significantly improved performances in terms of responses (enhanced $\sim\!\!20$ times), LOD (improved by $\sim\!\!100$ times, the response and recovery behaviors (accelerated by 48% and 470%, respectively) as well as the operating temperature (reduced by $\sim\!\!125$ °C).

It is found in experiment that, gaseous analytes with similar sensing responses show different kinetic diameters (D_k) , which thereby enhance its selectivity of MO_X core by modulating the channel traffic of analytic molecules in MOF sheath based on their D_k difference. Similar to the situation mentioned for the Pd/ZIF-8 sensors [182], the flexibility of ZIF-8/MAF-4 framework is thermodynamically unfavorable for the sieving effects of gas molecules on the chemiresistive gas sensors. According to the sensing measurements towards other gases, ZnO@ZIF-CoZn almost responded to all the tested gases, with the differences in responses originating from the cross-sensitivity of ZnO towards these gases (Fig. 27e). Similar problems on traffic control of the gas molecules works on other ZIFs or MIL-125 as the sheathes/shells, which is due to their drawback of the dynamically open and/or oversized aperture [192,201,209]. Therefore, the essential issue to be addressed is how to control the channel flexibility, functionalization and/or size in the MOF sheaths, thus realizing the modulated selectivity by controlling the channel traffic of gaseous anlaytes. Accordingly, the Au-ZnO@ZIF-8-DMBIM with the traffic control ability of acetone and benzene series was prepared by G Xu's group through the *in-situ* post-synthetic modification of ZIF-8 sheath with DMBIM ligands (Fig. 27f) [205]. The ZIF-8-DMBIM sheath showed much more rigid and smaller aperture than that of the pristine ZIF-8 sheath, which promoted the selective penetration of acetone due to its smaller D_k . Consequently, vapor sorption measurements and chemiresistive sensing results displayed the good selectivity toward acetone against benzene series are ($S_{acetone/benzene}$ = 21.6, Table 5, Fig. 27g and h). By employing the linear discriminant analysis (LDA) method, the Au–ZnO@ZIF 30 nm–DMBIM achieved high accuracy in classifying 90 trials with a small standard deviation.

In a different way, the channel traffic effects can be modulated using RHO-type ZIF-71 instead of SOD-type ZIF-8 in the MOF-MOx composites, which can be ascribed to the different topology and functional groups of organic ligands [204]. Notably, ZIF-71, a zeolite MOF constructed by Zn ions with 4,5-dichloroimidazole (dcIm), possessed larger pore size (4.8 Å) and cavities (16.8 Å) in its framework than those of ZIF-8. Moreover, the sensing results showed

Table 5Gas-sensing properties toward different gases of various MOF composites based chemiresistive gas sensors. (1. Experimental LOD, 2. IUPAC method, 3. 3RMS with simulated equation, 4. 10% response).

Material	Structure	Conc.	R	t _{res} /min	t _{rec} /min	LOD/ppm	T/°C	S	Refs.
ZnO@ZIF-8	thick film	HCHO 100 ppm	~12.5	~0.27	~0.15	$\sim 5.6^{2}$	300	4 ethanol	[201]
ZnO@ZIF-8	thick film	Acetone 100 ppm	~3	N. A.	N. A.	N. A.	300	~0.9 ethanol	[201]
								2 toluene	
ZnO@CoZn-ZIF 5 nm	thin film	Acetone 100 ppm	82.97	0.72	1.02	0.0019^4	260	~2.1 m-xylene	[192]
Au-ZnO@ZIF-DMBIM 5 nm	thin film	Acetone 100 ppm	231	~3	~1	0.0034^4	275	21.6 benzene	[205]
								~3.7 m-xylene	
ZnO@ZIF-8	thin film	H2 50 ppm	1.62	N. A.	N. A.	10^{1}	300	2.8 benzene	[202]
ZnO@ZIF-8	thin film	H2 50 ppm	2.28	N. A.	N. A.	5 ¹	250	~3.3 CO	[203]
ZnO@ZIF-8	thin film	Propene/ethene 250 ppm	~50/~13	N. A.	N. A.	N. A.	350	N.A.	[207]
								Anti-humidity	
ZnO@ZIF-8	thin film	H ₂ S 10 ppm	~1	N.A.	N.A.	N.A.	125	N.A.	[208]
ZnO@ZIF-8@POM	thick film	НСНО	4.4	0.25	0.27	0.387^{4}	RT, light	14.7 ethanol	[26]
		100 ppm					, 0	12.6 toluene	
ZnO@ZIF-71	thin film	Ethanol	13.4%	3.24	7.37	0.021^{2}	150	Anti-humidity	[204]
		10 ppm						•	
ZnO@ZIF-71	thin film	Acetone	38.9%	3.27	8.92	0.003^2	150	~6.5 ethanol	[204]
		5 ppm						Anti-humidity	
ZnO@ZIF-71	thin film	Ethanol	~8	N. A.	N. A.	10^{1}	250	~30 benzene	[206]
		100 ppm						~4 H ₂	
ZnO@ZIF-71	thin film	Acetone	~2.5	N. A.	N. A.	10^{1}	250	~25 benzene	[206]
		50 ppm						~3.1 H ₂	

^a two probe pellet, ^b four probe, ^c van der Pauw, ^d two probe thin film.

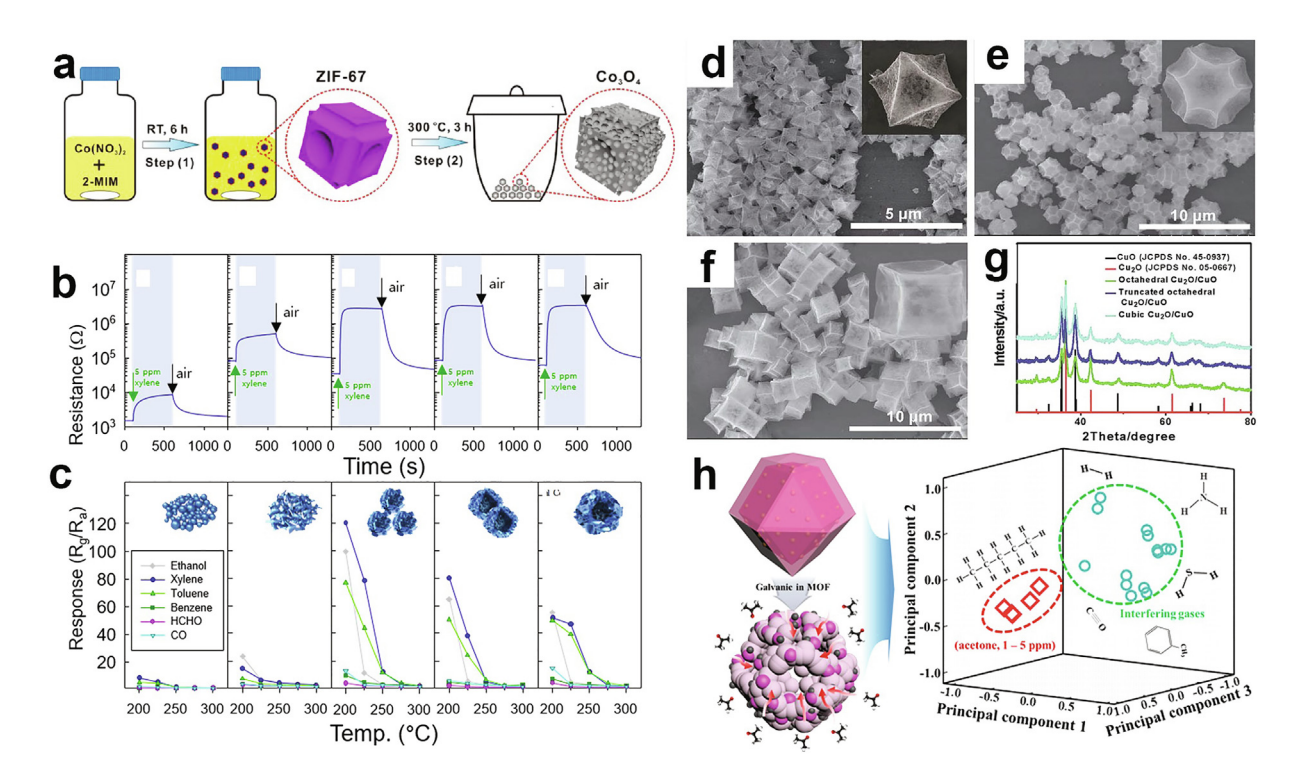


Fig. 28. (a) Schematic diagram of the synthesis of ZIF-67-derived porous Co_3O_4 particles. Reproduced with permission [211]. Copyright 2014, American Chemical Society. (b) Dynamic sensing transients towards 5 ppm of p-xylene at 225 °C and (c) gas responses towards 5 ppm of ethanol, p-xylene, toluene, benzene, formaldehyde, and carbon monoxide at 200–300 °C of different ZIF-67 derived monodisperse hollow hierarchical Co_3O_4 nanocages. Reproduced with permission [212]. Copyright 2018, American Chemical Society. SEM images of as-prepared Co_2O_4 coages with different morphologies: (d) octahedra, (e) truncated octahedra, (f) cubes; insets in (a)–(c) show magnified images; (g) XRD patterns of the three Co_2O_4 coages. Reproduced with permission [213]. Copyright 2015, The Royal Society of Chemistry. (h) Schematic diagram of prepared process for the n-SnO₂ HNCs functionalized with Co_3O_4 and PdO and the pattern recognition based on PCA using sensor arrays (Co_3O_4 loaded n-SnO₂ HNCs and Co_3O_4 -PdO loaded n-SnO₂ HNCs). Reproduced with permission [214]. Copyright 2017, American Chemical Society.

that it had enhanced selectivity towards ethanol against benzene and H_2 .

Different from ZnO@ZIFs used for sensors that work at moderate temperatures (100–350 $^{\circ}$ C), two methods can be used to enable the RT sensing detection for MOF-MOx composites. Of them, one method is based on the resistance change induced by the reversible

phase change. A representative example is the formation of metal sulfides (MSs) for MOx containing the sensing materials upon the exposure to H₂S, a dangerous toxic gas with high activity [118,208]. The other method is to introduce the photocatalytic components to realize RT sensing activity via photogenerated charge carriers [195,210]. MOFs act as the gas pre-concentration

and selective adsorption/rejection components in both cases. For instance, G. Zhu's group integrated the photo activity of ZnO, the electron capture of polyoxometalate (POM), and the hydrophobicity and high porosity of ZIF-8 into one material [210]. Assisted by a Xe lamp, the resultant ZnO@ZIF8@POM sensor showed good response, fast speed and selectivity towards HCHO at RT (Table 5).

3.3. MOFs derived materials for chemiresistive gas sensors

3.3.1. MOx and their composites

The regular metal nodes and functional organic ligands located in MOFs, along with additional cavities, are well matched with the precursors required for porous MOx and their composites. Inspired by excellent works on MOF derived materials in other areas, Q Kuang's group prepared the ZIF-67 derived porous Co₃O₄ particles for chemireisitive gas sensors in 2014 (Fig. 28a) [211]. To improve the sensing performances, J. H. Lee's group further obtained the ZIF-67 derived monodisperse hollow hierarchical Co₃O₄ nanocages in combination with intermediate solvothermal treatment of ZIF-67 self-sacrificial templates [212]. The sensing characteristics are closely related to the size, thickness of the shell, meso-pores, as well as hollow/hierarchical morphology. As a result, the optimal sample with the highly gas accessible areas/sites and good gas diffusion exhibited high responses to 5 ppm p-xylene (78.6) and toluene (43.8) at 225 °C (Fig. 28b and c).

The mixed phases of $\text{Cu}_2\text{O}/\text{CuO}$ cages, which have hierarchical structure and high surface areas (~150 m² g⁻¹), can be obtained with HKUST-1 polyhedra as the precursors (Fig. 28d-g). Through controlled oxidizing pyrolysis, the metal ions-loaded MOFs or MOFs with heterostructure, ZnO porous nanosheets [215], porous p-n/n-p (e.g. $\text{Zn}_x\text{Co}_{3-x}\text{O}_4$, $\text{ZnO-Co}_3\text{O}_4$, Co_3O_4 - In_2O_3 , LaFeO_3/α -

 Fe_2O_{31} [216–220], bimetallic MOx (e.g. NiFe₂O₄) [221], or noble metal decorated MOx (e.g. Ag-In₂O₃, PdO-Co₃O₄-SnO₂) [214,222], can be obtained when replacing the precursors by the bimetallic MOF. To take an example, I. D. Kim's group reported a MOFs derived n-type SnO₂ porous structures based on the p-n transition in MOF-templated p-type Co₃O₄ by galvanic replacement reaction (GRR) [214]. Eventually, the catalytic Pd catalysts in MOF precursors formed the porous PdO-Co₃O₄-SnO₂ with the residual Co₃O₄ clusters during GRR (Fig. 28h). Notably, the PdO-Co₃O₄-SnO₂ sensor exhibited good sensitivity, fast speed and excellent selectivity towards acetone at 450 °C, which was attributable to the highly gas accessible surfaces and effective modulation of the electron depletion layer assisted by the abundant p-n junction (Table 5). In addition, the PCA results showed good discrimination of 8 gas molecules, and the concentration variations ranged from 1 to 5 ppm SnO_2 (Fig. 28h).

3.3.2. Carbon materials and their composites

The extensively investigated MOF derived carbon materials represent a famous class of active materials, which have widely applied in lots of areas, like energy storage/conversion, environmental remediation, and catalysis [59,223–225]. Inspired by the excellent RT sensing activity of semiconductor-carbon composites, the porous MOF derived carbon materials can also serve as the promising active materials for chemiresisitors based on the semiconductor-carbon composites [226,227].

Using MOFs pre-loaded with active material as the precursors is an effective synthetic method for the MOF derived semiconductor-carbon. As shown in Fig. 29a, when the WS₂-loaded ZIF-67 is used as the precursor, the well distributed 2D few-layered WS₂ confined within the porous carbon composites can be acquired [227]. More-

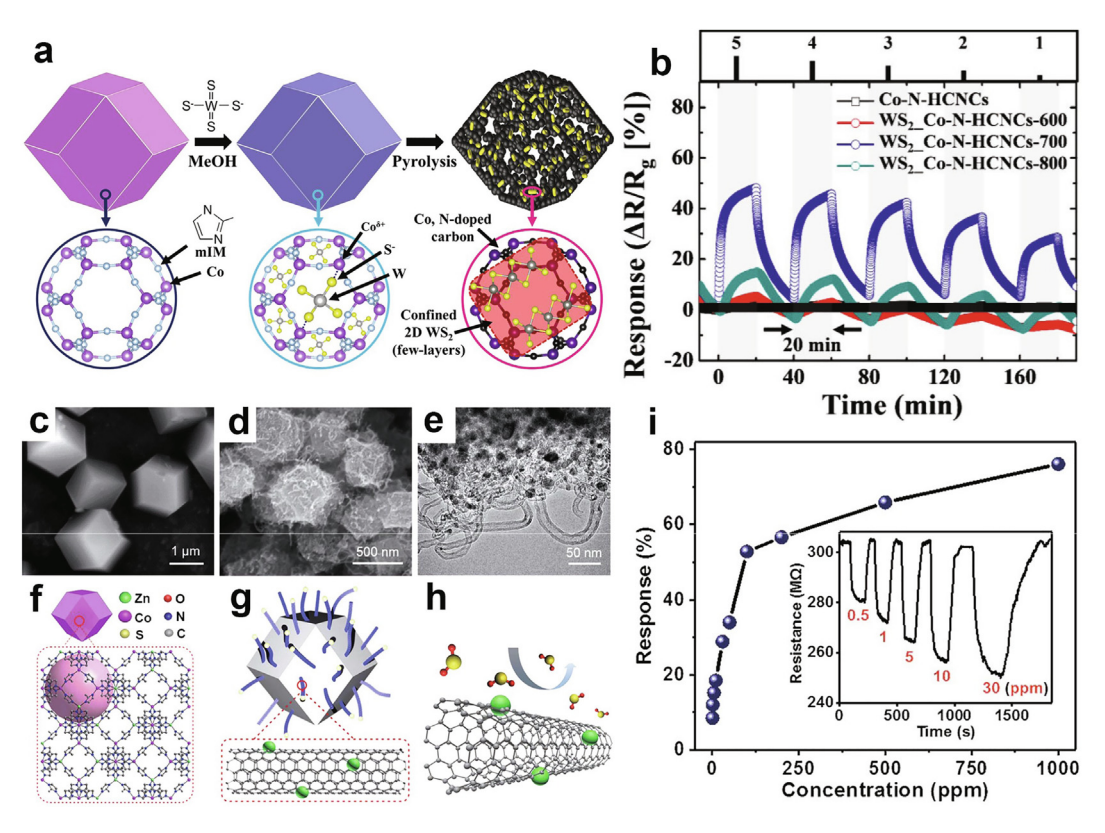


Fig. 29. (a) A schematic illustration of preparation process of WS $_2$ -Co-N-HCNCs derived from MOF based precursor; (b) dynamic response transitions of the sensors toward 1–5 ppm of NO $_2$ measured at RT. Reproduced with permission [227]. Copyright 2018, WILEY-VCH Verlag GmbH & Co. KGaA, Weinheim. SEM image of (c) polyhedral particles of ZnZIF-67 and (d) CoZn-NCNTs, respectively; (e) TEM image of the Medusa-hair-like structure on the surface of CoZn-NCNT particles; Schematic representations of the structures of (f) ZnZIF-67 and (g) CoZn-NCNTs, respectively; (h) Schematic of the adsorption of SO $_2$ molecules assisted by Zn doping atoms on the nanotubes. Reproduced with permission [226]. Copyright 2019, The Royal Society of Chemistry.

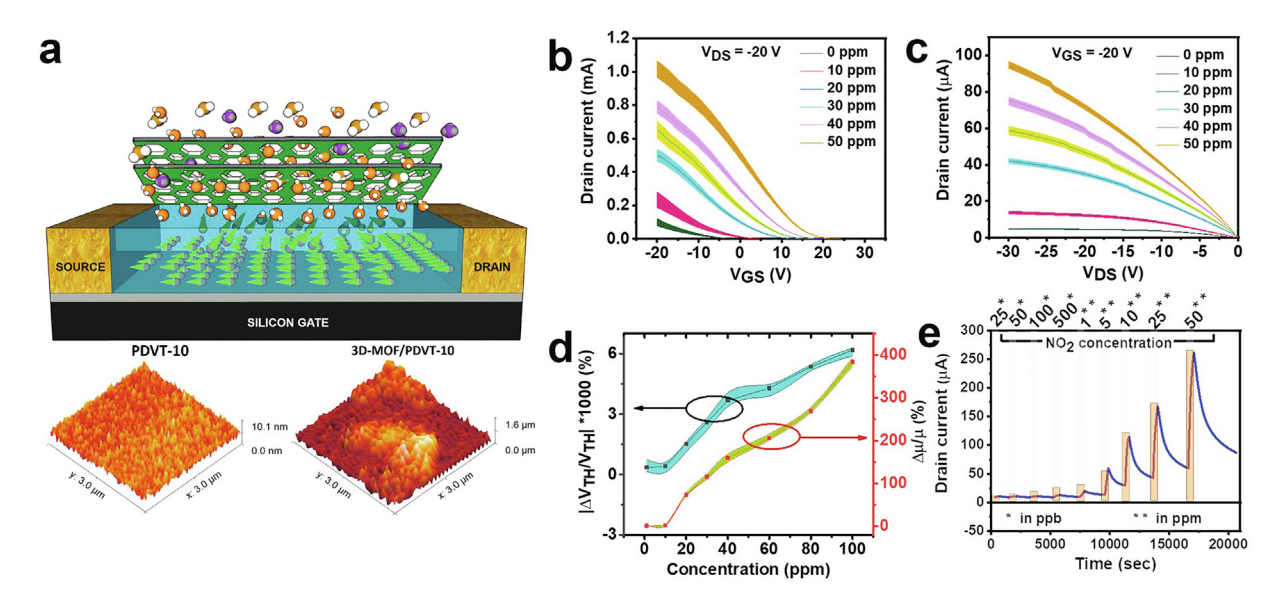


Fig. 30. (a) Schematic diagram of gas molecules interaction process in a bottom-gate bottom-contact [Ni(TPyP)(TiF₆)]_n/PDVT-10 OFET and the AFM topography images of PDVT-10 and [Ni(TPyP)(TiF₆)]_n/PDVT-10 layers; (b) Transfer and (c) output characteristics of PDVT-10/MOF-A OFET toward different gas concentrations from 0 to 50 ppm; (d) relation between threshold voltage (V_T) and charge carrier mobility (μ) toward different gas concentrations from 1 to 100 ppm; (e) transient analysis for different concentrations from 25 ppb to 50 ppm. Reproduced with permission [232]. Copyright 2020, American Chemical Society.

over, the N-rich 2-methlyimidazole ligand further provides active N dopants for the carbon materials. During the pyrolysis process, the ZIF-67 framework has effectively suppressed the growth of WS₂. Note worthily, the successful introduction of the highly active few-layered WS₂ has remarkably enhanced the NO₂-sensing properties of carbon materials at RT (Fig. 29b, R5ppm = \sim 48.2%), and excellent selectivity against interfering gases is also achieved. As indicated by the authors of this work, the value of responses to NO₂ at RT is not satisfied compared with those of the well-studied non-TMD materials, further improvements are warranted.

Due to the catalytic effects of metal ions in the process of pyrolysis, the resultant in-situ growth of CNTs forms the porous metal-CNT composites. Consequently, in this study, the CoZn-N doped CNT composites (CoZn-NCNTs) were synthesized via the controlled calcination of CoZn-ZIF (isostructural to ZIF-8/ZIF-67) precursors (Fig. 29c-h) [226]. As a result, the CoZn-NCNTs particles possessed a porous polyhedral morphology with rich interconnecting CNTs on the surface showing outstanding sensitivity ($R_{100ppm} = 53\%$) and fast speed (response/recovery time; 1.3/0.53 min) towards SO₂ at room temperature.

4. Metal-organic frameworks (MOFs) for field-effect transistor (FET) gas sensors

Compared with conventional sensors composed of simply two electrodes, the FET-type gas sensor can control the applied voltage on the gate electrode, finally enabling the easy amplification and fine-tuning of detected electrical signals. Therefore, it can be used as a promising electrically-transduced gas sensor for high performance detection. In addition, FET devices is capable of microminiaturization, as a result, they can be easily integrated with other electrical devices. However, advanced techniques are required to integrate materials into FET device, such as lithography, precise control over material morphology and interfaces with insulating layers.

Up to now, only a few reports involve the study of MOF-based FETs. Similar to chemiresistors, the conductivity requirement of active materials of FET devices also represents an obstacle for most reported MOFs, which is because of their poor conductive nature. Consequently, the insulating MOFs are generally used as the auxil-

iary materials to active materials in FET devices, which have the functions of pre-concentration, dielectric layer modification, and/ or catalysts [228-231]. Most of these FET sensors work either in liquid phase or based on the Kelvin probe technique. Just recently, S. Yuvaraja et al. prepared the MOF/polymer bi-layer OFET gas sensors through coating the porphyrin MOF (an additive for gas preconcentration) onto the active polymer layer (Fig. 30a) [232]. Moreover, the [Ni(TPyP)(TiF₆)]_n MOF particles (TPyP, 5,10,15,20-t etra(4-pyridyl)porphyrin) with good NO2 selectivity were dropcasted onto the sensitive channel layer prepared by the diketopyrrolopyrrole (DPP) copolymer with thiophene donor blocks (PDVT-10), so as to form the bi-layer OFET. As discovered, the prepared [Ni(TPyP)(TiF₆)]_n/PDVT-10 FET sensor showed sensitive transfer characteristics upon exposure to NO₂ with concentrations ranging from 0 to 50 ppm (Fig. 30b). The output characteristics exhibited a non-saturated regime of drain current for all biases, when the device was exposed to NO2 at a concentration of 20 ppm or higher (Fig. 30c). This was attributed to the excess charge carriers caused by high concentration of analytes in the channel region. As shown in Fig. 30d, the threshold voltage decreased nearly 3 orders of magnitude when NO₂ concentration increased from 0 to 100 ppm, while the charge carrier mobility increased linearly with the increasing NO2 gas concentration. The sensor also showed good response-recovery properties towards NO_2 when the gas concentration was lower than 5 ppm (Fig. 30e).

Alternatively, conductive MOFs possessing regularly distributed pore size, tunable structure and good electrical properties are extremely desirable as the promising active materials for porous-FET, which may promote the new developments in the field of FET gas sensing. The porous FET, in which the EC-MOF thin film [233–235] or proton conductive Cu-BTC [236] is used as the active material, has been successfully obtained, yet it remains challenging to fabricate the high performance FET gas sensor. V. Rubio-Giménez *et al.* attempted to introduce Cu₃HHTP₂, an EC-MOF with excellent RT chemiresistive gas sensing performance, into the FET devices via a bottom-up approach [237]. The channel current of the as-transferred films increased with the decrease in $V_{\rm g}$ (p-type transport), and changed at different atmospheres, indicating that it might be applied in gas detection. However, Cu₃HHTP₂ FET showed small modulation of source-drain current with back gate

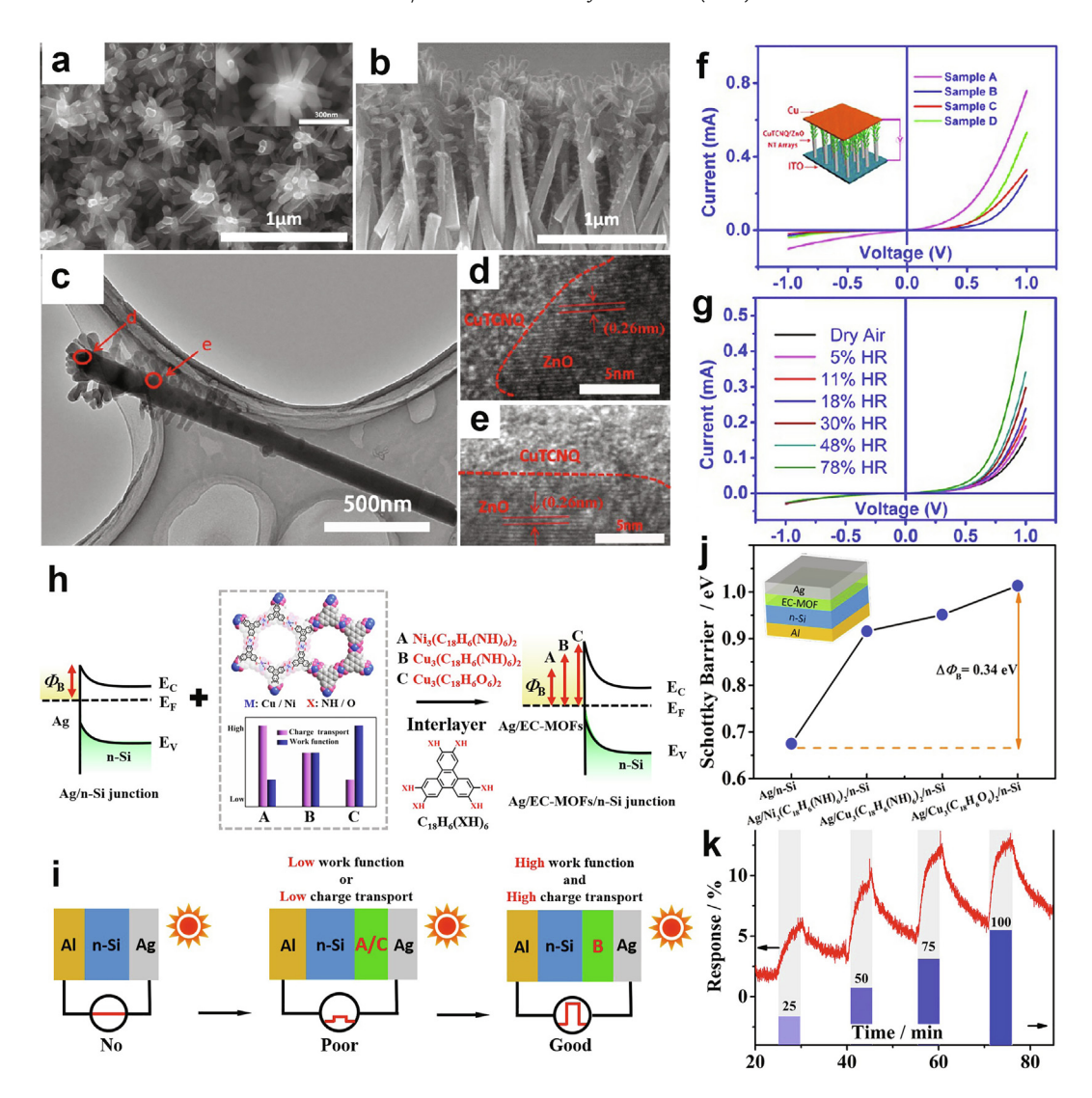


Fig. 31. (a) SEM images of CuTCNQ/ZnO p-n junction arrays (a) top view, inset: the magnified top view; (b) the corresponding cross-section view; (c) TEM image of an individual CuTCNQ/ZnO nanowire; (d and e) HRTEM images of the interface region between CuTCNQ NR and ZnO NR marked in part c; I-V characteristics of (f) different samples of CuTCNQ/ZnO arrays at room temperature (Inset: the schematic illustration of the ITO/CuTCNQ/ZnO p-n junction arrays/Cu device) and (g) sample B measured at 25 °C exposed to different RH. Reproduced with permission [137]. Copyright 2013, American Chemical Society. (h) The energy band structure of Ag/n-Si and Ag/ECMOF/n-Si; (i) Different Schottky diodes device structures with various photoelectric performance; (j) various Schottky barriers height in different diodes and (k) response-recovery curves of Ag/Cu₃(C₁₈H₆(NH)₆)₂/n-Si/Al toward 25–100 ppm NH₃. Reproduced with permission [133]. Copyright 2020, The Royal Society of Chemistry.

voltage, which might be due to the poor contact between the MOF thin film and the octadecyltrichlorosilane (OTS) functionalized layer.

5. MOFs and their derivatives for chemical diodes type gas sensors

As discussed in Section 2, chemical diode, a key resistance-dominated element (Fig. 13a), plays a role as a p-n junction (Fig. 6) or metal–semiconductor Schottky junction (Figs. 7 and 8). The height of potential or Schottky barrier (Φ_B) can be modulated either by changing the energy levels of p/n components or by altering the work functions of metal electrode and the electron affinity of semiconductor, respectively.

5.1. MOFs for chemical diodes type gas sensors

For the p-n junction-based chemical diodes, the semicondcutive MOF can be directly applied as the active materials. TCNQ (7,7,8,8-

tetracyanoquinodimethane), a redox-active ligand first prepared by Dupont researchers in the 1960s [238], can serve as a tetradentate or bidentate bridging ligand to balance the positive charge of center metal and to form the new EC-MOFs [239-241]. In view of this, H. Liu et al. fabricated the CuTCNQ/ZnO p-n junction arrays, in which n-type ZnO nanorods (NRs) were used as the backbones, whereas p-type CuTCNQ NRs as the branches (Fig. 31a-e) [137]. The CuTCNQ/ZnO p-n junction arrays displayed excellent diode nature (Fig. 31f). Besides, the corresponding CuTCNQ/ZnO NT diode-type humidity sensor showed good sensitivity (changes in rectification ratios were used in this work, experimental detection limit, 5 RH%) and quick response properties ($t_{res.80\%}$ = 1 min) at RT (Fig. 31g). Noteworthily, the channels in the CuTCNQ frameworks were too small to show a detectable porosity. Thus, the combination of EC-MOFs with permanent porosity with the inorganic semiconductor may shed more lights on such type of chemical diodes for gas detection.

For semicondcutor-metal Schottky junction-based chemical diodes, $\Phi_{\rm B}$ is insensitive by changing the metal electrodes, which

Table 6Gas-sensing properties toward different gases of various MOF derived materials based chemiresistive gas sensors. (1. Experimental LOD, 2. IUPAC method, 3. 3RMS with simulated equation, 4. 10% response).

Material	MOF	Gas	Conc.	R	t _{res} /min	t _{rec} /min	LOD/ppm	T/°C	$BET/m^2 g^{-1}$	Refs.
Co ₃ O ₄ 300	ZIF-67	ethanol	200 ppm	3.25	<0.17	<0.17	10 ¹	300	120.9	[211]
Co ₃ O ₄ nanocages	ZIF-67	ethanol	5 ppm	99.2	N. A.	N. A.	N. A.	200	53.7	[212]
Co ₃ O ₄ nanocages	ZIF-67	p-xylene	5 ppm	~80	1.05	1.43	5 ¹	225	53.7	[212]
Co ₃ O ₄ polyhedra	ZIF-67	n-butanol	100 ppm	19	2.43	1.5	<5 ¹	100	50.9	[267]
Co ₃ O ₄ core-shell	ZIF-67	Acetone	200 ppm	12	0.07	0.13	10^{1}	190	44.5	[268]
Co ₃ O ₄ spheres-350	$Co_5(\mu 3-OH)_2(1,4-ndc)_4(bix)_2]_n$	formaldehyde	100 ppm	10.7	0.77	1.63	10^{1}	170	30.78	[269]
In2O3 Hollow Nanorod	CPP-3	ethanol	100 ppm	37.6	0.05	0.07	5^{1}	300	38.9	[270]
Cu ₂ O/CuO cages	HKUST-1	ethanol	200 ppm	5.5	N. A.	N. A.	N. A.	150	150.3	[213]
CoZn-NCNTs	CoZn-ZIF	SO_2	100 ppm	53%	1.3	0.53	0.5^{1}	RT	446.35	[226]
ZnO-Co ₃ O ₄ polyhedrons	CoZn-ZIF	ethanol	100 ppm	~9	0.12	3.93	1 ¹	200	53.62	[217]
ZnO-Co3O4 polyhedrons	ZIF8@ZIF-67	trimethylamine	50 ppm	231	0.035	0.20	0.013^{1}	260	N.A.	[220]
$Zn_xCo_{3-x}O_4$	CoZn-ZIF	acetone	200 ppm	34.6	0.72	0.85	0.5^{1}	170	159	[216]
Co_3O_4 - In_2O_3	Co ²⁺ loaded MIL-68(In)	trimethylamine	50 ppm	785.8	0.78	0.33	2^{1}	300	15.01	[218]
$LaFeO_3/\alpha$ - Fe_2O_3	MIL-53/La-Fe LDHs	acetone	100 ppm	19	0.05	0.08	1^{4}	230	62.23	[219]
NiFe ₂ O ₄	Ni-Fe MOF	n-propanol	100 ppm	88.2	0.32	0.70	0.41^4	120	86.2	[221]
PdO-Co ₃ O ₄	Pd@ZIF-67	acetone	5 ppm	1.51	N. A.	N. A.	0.1^{4}	350	20.18	[271]
5% Ag-In ₂ O ₃	Ag ⁺ loaded In-MOF	НСНО	50 ppm	155.8	0.95	0.37	0.003^2	210	21.39	[222]
PdO-Co ₃ O ₄ -SnO ₂	Pd@ZIF-67	acetone	5 ppm	21.8	1.51	1.81	0.05^{4}	450	31.76	[214]
WS ₂ -Co-N-C	WS ₂ -ZIF-67	NO_2	5 ppm	~48.2%	~7	>10	0.1^{2}	RT	24.07	[227]
PdO-Co ₃ O ₄ -SWCNTs-700	Pd@ZIF-67-SWCNTs	NO_2	20 ppm	~27.3%	~1.5	Irrev.	1 ¹	RT	20.96	[272]

irrev. is irreversible.

Table 7Gas-sensing properties toward different gases of various MOF and MOF derived materials based FET, chemical diodes, and electrochemical gas sensors. (1. Experimental LOD, 2. IUPAC method, 3. 3RMS with simulated equation, 4. 10% response).

Material	Sensor type	Gas	Conc.	t _{res} /min	$t_{\rm rec}/{ m min}$	LOD/ppm	T/°C	$\mathrm{BET}/\mathrm{m}^2~\mathrm{g}^{-1}$	Refs.
[Ni(TPyP)(TiF ₆)] _n /PDVT-10	FET	NO_2	0.025-50 ppm	0.72	7.3	0.008	RT	991	[232]
Cu ₃ HHTP ₂	FET	air	saturated	N.A.	N.A.	N.A.	RT	348	[237]
ZnO/CuTCNQ	diodes	RH	5-78 RH%	1	30	5 RH% ¹	RT	N.A.	[137]
Ag/Ni ₃ HITP ₂ /n-Si/Al	diodes	NH_3	25-100 ppm	2.4	7.5	25^{1}	RT	N.A.	[133]
							450 nm light		
Fe-BTC	electrochemical	methanol	0-35 vol%	N.A.	N.A.	N.A.	120	N.A.	[138]
Fe-BTC	electrochemical	ethanol	0-18 vol%	N.A.	N.A.	N.A.	120	N.A.	[138]
$[Cu(p-IPhHIDC)]_n$	electrochemical	NH_3	2-130 ppm	N.A.	N.A.	2^{1}	RT	N.A.	[139]
			• •				68 RH%		
${Na[Cd(MIDC)]}_n$	electrochemical	NH_3	0.05-30 ppm	N.A.	N.A.	0.05^{1}	RT	N.A.	[251]
			• •				98 RH%		
$[Ba(o-CbPhH_2IDC)(H_2O)_4]_n$	electrochemical	NH ₃	1-25 ppm	N.A.	N.A.	1^{1}	30	N.A.	[250]
2 // 2 ///		-					98 RH%		
$[Cu_4(HDMPhIDC)_4(H_2O)_4]_n$	electrochemical	NH ₃	10-60 ppm	N.A.	N.A.	10^{1}	RT	N.A.	[249]
74(2)411		<u> </u>					98 RH%		

Table 8Gas-sensing properties toward different gases of various MOF and MOF derived materials based chemicapacitive gas sensors. (1. Experimental LOD, 2. IUPAC method, 3. 3RMS with simulated equation, 4. 10% response).

Material	Gas	Conc.	R	t _{res} /min	$t_{\rm rec}/{ m min}$	LOD/ppm	T/°C	$BET/m^2 g^{-1}$	Refs.
Cu(BDC)(H ₂ O) _x	Toluene	500 ppm	0.1%	N. A.	N. A.	125 ¹	22	N. A.	[256]
Fum-fcu-MOF	H_2S	100 ppm	~0.45%	N. A.	N. A.	0.0054^4	RT	N. A.	[56]
Cu-BTC (HKUST-1)	Acetone	250 ppm	6.3%	~3	~2.2	61.99^4	RT, 10RH%	1263	[258]
	Isopropanol		35%	~2.3	~2.2	71.05^4			
	Ethanol		48.6%	~1.4	~1.7	77.8^{4}			
	methanol		61%	~1.1	~1.1	100. 18 ⁴			
Cu-BTC (HKUST-1)	Ethanol	250 ppm	~5%	N. A.	N. A.	130^{4}	RT	704.5	[257]
	methanol		~11%			39.1 ⁴			
MFM-300 (In)	SO_2	1 ppm	0.0016%	N. A.	N. A.	0.005^4	RT	N. A.	[259]
Ag2O@UiO-66(Zr)-NO ₂	H_2S	100 ppm	~90%	3.33	Irrev.	1^{1}	RT	359.2	[260]
Cu-BTC (HKUST-1)	Acetone	250 ppm	2.6%	N. A.	~1.7	149^{4}	RT, 10RH%	1263	[273]
	toluene		9%		~2.3	97^{4}			
MIL-96 (Al)	methanol	5000 ppm	~5%	10-15	10-15	N. A.	RT	N. A.	[263]
MOF-74 (Mg)	benzene	100 ppm	~0.15%	N. A.	N. A.	2^{1}	RT	N. A.	[57]
NH2-MIL-53(Al)/Matrimid polyimide	methanol	5000 ppm	~2.5%	>10	>10	N. A.	RT	N. A.	[261]
NDC-Y-fcu-MOF	NH_3	100 ppm	0.0025%	4.17	N. A.	0.092^{4}	22	N. A.	[262]

can be attributed to the Fermi pinning effect [242,243]. Consequently, several materials, including graphene, MO₃, MoS₂, and P₃HT, have been applied as the interlayer materials between metal and semiconductor to increase $\Phi_{\rm B}$ [244–247], thus improving the

diode performances. From the perspective of gas detection, the high porosity and tuable electronic structures of MOFs have rendered them as the promising interlayer materials to optimize the performances of Schottky junction-based gas sensors. For instance,

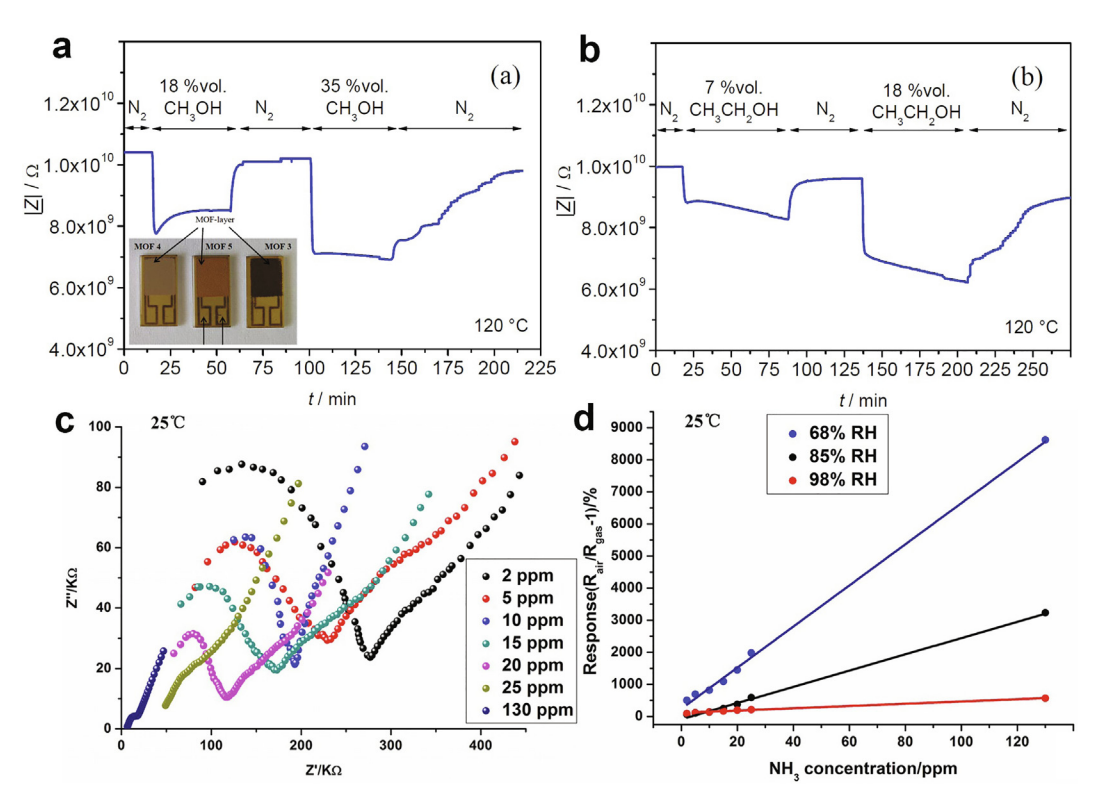


Fig. 32. Impedimetric sensor signal (|Z|) of a thick film Fe-BTC sensor at 1 Hz for (a) 0–35 vol% methanol in the test gas (the inset, top view of MOF paste screen-printed on IDEs to form thick film sensors), and (b) 0–18 vol% ethanol in the test gas. Measurement temperature: T = 120 °C. Reproduced with permission [138]. Copyright 2008, Sabine Achmann. (c) Impedance spectra for MOF 1 based sensor at 25 °C, 68% RH, with 2–130 ppm NH₃ gas; (d) linear plots of responses vs. concentrations toward NH₃ gas at different RH levels at 25 °C. Reproduced with permission [139]. Copyright 2018, Wiley-VCH Verlag GmbH & Co. KGaA, Weinheim.

Cao et al. prepared thin film EC-MOFs with high quality by the LbL spraying method, which were then applied as the effective interlayer materials to modulate the $\Phi_{\rm B}$ of the obtained Ag/EC-MOF/ n-Si (Fig. 31h) [133]. The I-V curves of these diodes showed typical rectifying characteristics of Schottky junctions (Fig. 13b). Using the thermionic emission theory model [248], the $\Phi_{\rm B}$ values of different Ag/EC-MOF-20 nm/n-Si were calculated, which were remarkably higher than those of Ag/n-Si junction diodes (Fig. 31j). Notably, Schottky junction-based diodes can be directly used as the selfpowered devices. Among the diverse Ag/EC-MOF-20 nm/n-Si sensors, Ag/Cu₃HITP₂/n-Si/Al achieved the best self-powered sensing performance. When the gas diffusion facilitated window-like Ag thin film (serve as the electrodes) was used together with the highly oriented porous structure of Cu₃HITP ₂ layer, the Ag/Cu₃(-C₁₈H₆(NH)₆)₂/n-Si/Al sensor showed a response of 13.5% to 100 ppm NH₃, with the response & recovery time of 2.4 and 7.5 min, respectively (Fig. 31k, under a 450 nm light, no bias

MOFs derived materials with p-n junctions or Schottky junctions commonly exist as the basic building units dispersed in the entire sensing films/pellets of chemiresistors or electrochemical gas sensors. To the best of our knowledge, there is no study reporting the direct application of MOFs derived materials as the key components for chemical diodes type gas sensors (see Tables 6–8).

6. MOFs and their derivatives for electrochemical gas sensors

In 2009, S. Achmann *et al.* employed Fe-BTC, a proton conductive MOF that contained the same organic ligand with the famous HKUST-1, as an active material for the electrochemical gas sensors

under 60 RH% at 120 °C (the inset of Fig. 32a). In addition, the impedimetric sensor signal (the absolute value |Z|) of a thick film Fe-BTC sensor at 1 Hz showed significant changes upon exposure to methanol or ethanol, and satisfactory response/recovery speed were acquired (Fig. 32a and b).

Since then, many proton conductive MOFs have been introduced into this area [139,249-253]. For example, G Li et al. prepared a proton conductive 2D MOF, namely, [Cu(p-IPhHIDC)]_n (p-IPhH3IDC = 2-(p-N-imidazol-1-yl)-phenyl-1H-imidazole-4,5dicarboxylic acid, 1.51×10^{-3} S cm⁻¹ at 120 °C and under 98 RH %), and subsequently applied it as an impedance type electrochemical gas sensor at RT and under 68-98 RH% (Fig. 32c) [139]. Notably, the abundant inter-layer uncoordinated carboxylate groups facilitated the excellent proton conductivity. Further, the corresponding sensor showed good sensitivity ($R_{130 \text{ ppm}}$ = 8620%) and noticeable detection limit of 2 ppm towards NH₃ gas at RT and under 68% RH. Unlike log-log linearity of typical chemiresistors, the impedance type electrochemical gas sensor exhibited good linearity of raw plots of responses vs. concentration (Fig. 32d). The differences observed can be explained by the sensing mechanism of the impedance type electrochemical gas sensor. Briefly, NH₃ molecules can not only interact with the coordinating H₂O and carboxylate groups in MOF to generate the hydrogen-bonding nets, but also can react with the exotic water molecules to constitute NH⁴⁺ cations. All these factors have affected the proton conductivity, as directly observed from the remarkably reduced value from 1.79 eV (68 RH%)/0.25 eV (98 RH%) to 0.50 eV (68 RH% containing 25 ppm NH₃ gas)/0.18 eV (98 RH% containing 25 ppm NH₃ gas).

To date, the electrochemical sensors based on MOF derived materials have been limited to molecule detection in liquid phase [252–255].

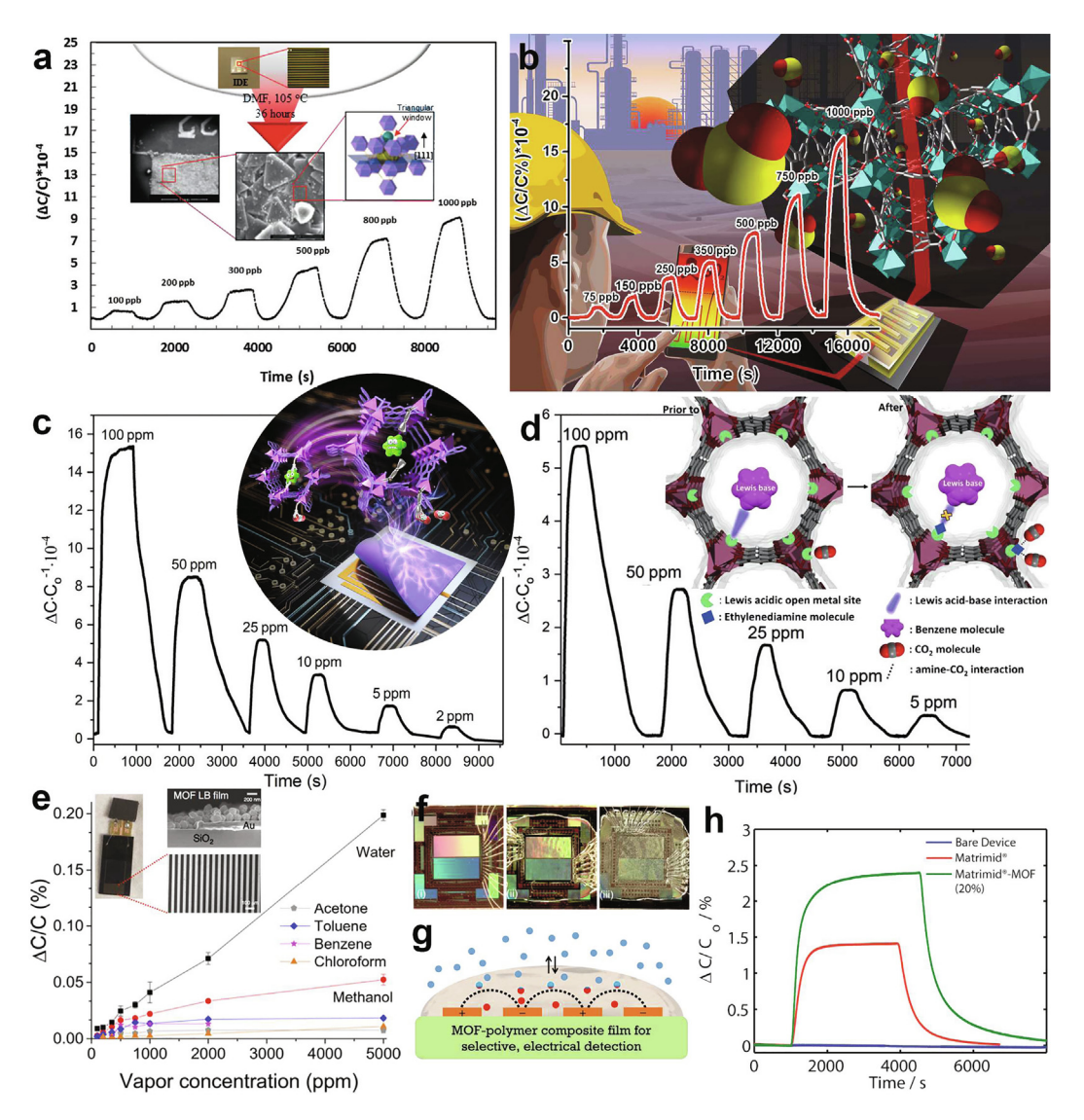


Fig. 33. (a) The capasitive response-recovery curve of the fumarate-based fcu-MOF (fum-fcu-MOF) chemicapasitors toward 100–1000 ppb of H₂S. Insets showed the preparation of thefum-fcu-MOF thin film on IDEs. Reproduced with permission [56]. Copyright 2016, Wiley-VCH Verlag GmbH & Co. KGaA, Weinheim. (b) The capasitive response-recovery curve of MFM-300 (In) MOF-based sensor toward SO₂ varying the concentration range from 75 to 1000 ppb (the background is the schematic representation of the potential practical application). Reproduced with permission [259]. Copyright 2018, The Royal Society of Chemistry. Real-time responses of the capacitive gas sensors based on (c) Mg-MOF-74 and (d) ethylenediamine-functionalized Mg-MOF-74 upon exposure to different concentrations of benzene vapor at RT (the inset of c is the schematic representation of the MOF capacitive sensor structures; the inset of d represents the MOF-analyte interactions before and after ethylenediamine functionalization). Reproduced with permission [57]. Copyright 2019, Wiley-VCH Verlag GmbH & Co. KGaA, Weinheim. (e) Responses comparisons of LB-based MIL-96(AI) capacitive sensors for different vapors. Reproduced with permission [263]. Copyright 2020, American Chemical Society. (f) Optical images of the (i) bare device, and devices coated with (ii) Matrimid polyimide and (iii) Matrimid and MOF (20 wt%); (g) schematic cross section of the MOF-polymer composite film on 4 AI planar electrodes; (h) response-recovery curves to 5000 ppm methanol of bare device and devices coated with Matrimid PI and Matrimid PI-MOF (20 wt%) composite film. Reproduced with permission [261]. Copyright 2016, American Chemical Society.

7. MOFs and their derivatives for capacitive type gas sensors

Advantageously, the pre-concentration and selective adsorption of the analytes of porous MOFs offer great potentials as the active materials of capacitive type gas sensors, also known as chemicapacitors. Unlike chemiresistors, chemicapacitors require the insulating nature of active materials, which is well matched with a majority of reported MOFs.

In 2015, H. Omran confirmed the potential application of MOFs based chemicapacitors by using the $CuBDC(H_2O)_x$ (BDC = benzene-1,4-dicarboxylic acid) [256]. Thereafter, researchers have successfully developed various sensitive MOFs to detect the typically toxic/harmful gases at RT, besides, they have been integrated into small chips in the form of high quality thin films [56,57,257–262].

By the in situ growth of rare-earth metal (RE) and fumarate-based MOF thin films with fcu topology (fum-fcu-MOF) on the IDEs chip, O. Yassine *et al.* fabricated the high-performance capacitive gas sensor, which displayed an outstanding detection sensitivity to H_2S at concentrations down to 100 ppb, which exhibited the detection limit of about 5 ppb at RT (Fig. 33a) [56]. Compared with low sensitivity and poor long-term stability of CuBDC(H_2O)_x and ZIF-8) due to the possible formation of metal sulfides, the RE hexanuclear cluster bridged by fum-fcu-MOF, the shorter and more rigid linker, prohibited the formation of metal sulfide. I addition, the fum-fcu-MOF sensor also exhibited good selectivity towards H_2S vs. CH_4 , NO_2 , H_2 , and C_7H_8 . They also found that, when the active material was changed to MFM-300 (In), the obtained sensor showed good sensitivity toward SO_2 with a low detection limit of

 \sim 5 ppb (Fig. 33b) [259]. In addition, it also showed a high antihumidity property of up to 30 RH% and a good selectivity towards SO₂ vs. CH₄, CO₂, NO₂ and H₂, indicating its great potentials in practical applications.

For common VOCs without strong oxidizing/reducing properties, benzene is one of the most stable molecules that can hardly be detected at RT. Taking advantages of the π -complexation-driven Lewis acid-base interactions between open metal sites and the planar π -cloud entities of benzene molecules, H. Yuan et al. fabricated the homogeneous Mg-MOF-74 thin film sensors (the inset of Fig. 33c) [57], which presented with good sensitivity to benzene at RT, with a significant signal-to-noise to low concentration of down to 2 ppm. In addition, the ethylenediamine-functionlized Mg-MOF-74 films showed decreased sensitivity to benzene whereas increased sensitivity to CO₂, which demonstrated a guest occupying method to modulate the sensing performances of MOFs sensors.

Besides, MOFs based capacitive gas sensors sensitive to other VOCs, such as acetone, toluene, methanol, and ethanol, are also explored [261,263]. For instance, based on the high sorption data of MIL-96(Al) towards water and methanol, M. A. Andres et al. prepared the corresponding sensor on IDE chips based on ordered LB monolayer films constructed by the 200 nm particles (the inset of Fig. 33e) [263]. As expected, the MIL-96(Al) LB films showed high sensitivity towards water and methanol (Fig. 33e). For the case of MOF-polymer composite films, the NH₂-MIL-53(Al) nanoparticles were dispersed within the Matrimid polyimide, which formed a thin film on surface of capacitive sensor chips with planar electrodes (Fig. 33f and g) [261]. As clearly observed from the sensing results, the MOF-polymer had enhanced response relative to those of bare samples, which might be ascribed to the additional changes in local polarity of the composite films brought by MOFs.

8. Conclusions and outlook

According to the above research, despite a late start, great strides have been made in MOFs and MOF derived materials based electrically-transduced gas sensors recently, which depends on the matching of device requirements and materials properties. The major obstacles for specific applications are identified based on extensive studies, and some potential solutions are also proposed to overcome those issues. Consequently, excellent proof-of-concept examples have been successfully developed for MOFs and MOF derived materials based chemiresistive, chemical diodes, impedimetric electrochemical, and chemicapacitive gas sensors. Across these distinct types of electrically-transduced gas sensors, we summarize unifying characteristics among MOFs and MOF derived materials discussed in this work as follows:

- (1) Porosity. The ultrahigh surface areas and tunable channel traffics of MOFs are realized through controlling the metal/ ligand arrangements, functionalization and structural parameters (including distances, angles, and molecular conformations). Moreover, gas diffusion and adsorption are the key steps in the development of novel MOF-based gas sensors, therefore, it is essential that these frameworks should possess properties of diffusion facilitating porosity, selective adsorption or rejection channels, and highly accessible surface areas. Typically, the MOF-derived materials can partially maintain the as-mentioned porosity of MOF precursors.
- (2) Conductivity. Given the distinct conducting mechanisms, EC-MOFs are mainly applied as the active materials for chemiresistive, FET and chemical diode gas sensors, whereas IC/PC-MOFs (ionic/protonic conductivity) are frequently

- used for impedimetric electrochemical and chemicapacitive gas sensors. Thanks to the rapid developments of conductive MOFs on mixed valance motifs and charge transport modulations over the past few decades, the 2D π -conjugated EC-MOFs have exhibited promising sensing performances at RT. MOF-derived materials normally exhibit good electrical conductivity, and thus there is no limitation regarding their conductivity.
- (3) Permittivity (dielectric constant). For FET and chemicapacitive gas sensors, the changes in permittivity (dielectric constant) induced by material-analyte interactions can be directly transformed to the readable electrical signals. At present, a few successful chemicapacitive gas sensors have been reported so far after screening various MOFs.
- (4) Thermal/photo-catalytic effects. Using the thermal/photo-catalytic metal/ligands motifs or hybridizing with secondary catalysts, MOFs or MOF-derived materials have significantly improved the sensing performances, in particular, they possess both high surface areas and regular channels.

However, there are still many worthwhile directions to be pursued in terms of material design and device integration:

- (1) How to precisely control the gas diffusion and adsorption in the MOFs or MOF-on-MOFs. The sensing performances can be modulated by taking advantages of the flexibility, intermediate phase and glassy states of MOFs, together with the functionalized interfaces of MOFs and MOF based composites.
- (2) How to develop novel stable conductive MOFs or MOF-based composites with permanent porosity. The good balance between conductivity and sensing activity (redox activity and porosity) represents a key point for their applications in electrically-transduced gas sensors.
- (3) How to feasibly fabricate the thin film MOFs and well control their interfaces with the secondary hybrid materials, electrodes, and substrates. It is essential that, high performance gas sensor devices should possess cascading functions, including good sensitivity, excellent selectivity and fast speed.
- (4) How to combine *in-situ* characterizations with computational simulations to reveal the exact sensing mechanisms of MOFs based electrical gas sensors.
- (5) How to use data mining technology to screen the existing MOFs and MOF-derived materials or to predict the potential MOFs as the active materials of specific gas sensors.

The aforementioned challenges are the imperative tasks to be solved for the practical gas sensing applications of MOFs and MOF-derived materials. Future works along or beyond these lines will undoubtedly provide new fundamental understandings and practical application experiences concerning MOFs and MOF-derived materials for the electrically-transduced gas sensors.

Declaration of Competing Interest

The authors declare that they have no known competing financial interests or personal relationships that could have appeared to influence the work reported in this paper.

Acknowledgments

This work was supported by National Key R&D Program of China (2017YFA0206802), NSFC (21801243, 21822109, 21773245), Key Research Program of Frontier Science, CAS (QYZDB-SSW-SLH023), International Partnership Program of CAS

(121835KYSB201800), Natural Science Foundation of Fujian Province (2019]01129).

References

- [1] J.T. Fourkas, J. Phys. Chem. Lett. 2 (2011), 2945-2945.
- [2] Z. Meng, R.M. Stolz, L. Mendecki, K.A. Mirica, Chem. Rev. 119 (2019) 478–598.
- [3] W.-T. Koo, I.-S. Jang, I.-D. Kim, Chem 5 (2019) 1938-1963.
- [4] J. Zhang, X. Liu, G. Neri, N. Pinna, Adv. Mater. 28 (2016) 795–831.
- [5] W. Hu, L. Wan, Y. Jian, C. Ren, K. Jin, X. Su, X. Bai, H. Haick, M. Yao, W. Wu, Adv. Mater. Technol. 4 (2019) 1800488.
- [6] V. Schroeder, S. Savagatrup, M. He, S. Lin, T.M. Swager, Chem. Rev. 119 (2019) 599-663.
- [7] T.T. Dung, Y. Oh, S.-J. Choi, I.-D. Kim, M.-K. Oh, M. Kim, Sensors 18 (2018) 103.
- [8] R. Paolesse, S. Nardis, D. Monti, M. Stefanelli, C. Di Natale, Chem. Rev. 117 (2017) 2517–2583.
- [9] H. Li, M. Eddaoudi, M. O'Keeffe, O.M. Yaghi, Nature 402 (1999) 276-279.
- [10] O.M. Yaghi, M. O'Keeffe, N.W. Ockwig, H.K. Chae, M. Eddaoudi, J. Kim, Nature 423 (2003) 705–714.
- [11] S. Kitagawa, R. Kitaura, S.I. Noro, Angew. Chem. Int. Ed. 43 (2004) 2334–2375.
- [12] M. Kurmoo, Chem. Soc. Rev. 38 (2009) 1353–1379.
- [13] G. Férey, Chem. Soc. Rev. 37 (2008) 191-214.
- [14] M. Kondo, T. Yoshitomi, H. Matsuzaka, S. Kitagawa, K. Seki, Angew. Chem. Int. Ed. 36 (1997) 1725-1727.
- [15] H. Li, M. Eddaoudi, T.L. Groy, O. Yaghi, J. Am. Chem. Soc. 120 (1998) 8571-8572
- [16] L.J. Murray, M. Dincă, J.R. Long, Chem. Soc. Rev. 38 (2009) 1294-1314.
- [17] J.C. Tan, A.K. Cheetham, Chem. Soc. Rev. 40 (2011) 1059-1080.
- [18] B. Lebeau, P. Innocenzi, Chem. Soc. Rev. 40 (2011) 886–906.
- [19] D.-D. Zhou, P. Chen, C. Wang, S.-S. Wang, Y. Du, H. Yan, Z.-M. Ye, C.-T. He, R.-K. Huang, Z.-W. Mo, Nat. Mater. 18 (2019) 994-998.
- [20] C. Gu, N. Hosono, J.-J. Zheng, Y. Sato, S. Kusaka, S. Sakaki, S. Kitagawa, Science 363 (2019) 387-391
- [21] L.E. Kreno, K. Leong, O.K. Farha, M. Allendorf, R.P. Van Duyne, J.T. Hupp, Chem. Rev. 112 (2011) 1105-1125.
- [22] M.G. Campbell, D. Sheberla, S.F. Liu, T.M. Swager, M. Dincă, Angew. Chem. Int. Ed. 127 (2015) 4423-4426.
- [23] L. Liu, C. Zhang, L.-X. Zhang, Q. Li, Y.-Y. Yin, H.-Y. Wang, R.-H. Sun, J.-Y. Li, X.-Y. Hou, H. Dong, Inorg. Chem. Commun. 111 (2020) 107636.
- [24] Y. Zhang, Y. Chen, Y. Zhang, H. Cong, B. Fu, S. Wen, S. Ruan, J. Nanopart. Res. 15 $(2013)\ 2014$
- [25] K.N. Chappanda, O. Shekhah, O. Yassine, S.P. Patole, M. Eddaoudi, K.N. Salama,
- Sens. Actuators B, Chem. 257 (2018) 609-619. [26] A. Weiss, N. Reimer, N. Stock, M. Tiemann, T. Wagner, PCCP 17 (2015) 21634-21642
- [27] J. Liu, F. Sun, F. Zhang, Z. Wang, R. Zhang, C. Wang, S. Qiu, J. Mater. Chem. 21 (2011) 3775-3778.
- [28] X.-J. Lv, M.-S. Yao, G.-E. Wang, Y.-Z. Li, G. Xu, Sci. China Chem. 60 (2017) 1197-1204
- [29] J. Lee, O.K. Farha, J. Roberts, K.A. Scheidt, S.T. Nguyen, J.T. Hupp, Chem. Soc. Rev. 38 (2009) 1450-1459.
- [30] W.-H. Li, J. Lv, Q. Li, J. Xie, N. Ogiwara, Y. Huang, H. Jiang, H. Kitagawa, G. Xu, Y. Wang, J. Mater. Chem. A 7 (2019) 10431-10438.
- [31] M. Ding, R.W. Flaig, H.-L. Jiang, O.M. Yaghi, Chem. Soc. Rev. 48 (2019) 2783-2828
- [32] J. An, S.J. Geib, N.L. Rosi, J. Am. Chem. Soc. 131 (2009) 8376–8377.
- [33] E.A. Dolgopolova, A.M. Rice, C.R. Martin, N.B. Shustova, Chem. Soc. Rev. 47 (2018) 4710-4728.
- [34] I. Stassen, N. Burtch, A. Talin, P. Falcaro, M. Allendorf, R. Ameloot, Chem. Soc. Rev. 46 (2017) 3185-3241.
- [35] O. Shekhah, J. Liu, R. Fischer, C. Wöll, Chem. Soc. Rev. 40 (2011) 1081-1106.
- [36] L. Wang, Sens. Actuators, A (2020) 111984.
- [37] H.-N. Wang, X. Meng, L.-Z. Dong, Y. Chen, S.-L. Li, Y.-Q. Lan, J. Mater. Chem. A 7 (2019) 24059-24091.
- [38] J.M. Taylor, K.W. Dawson, G.K. Shimizu, J. Am. Chem. Soc. 135 (2013) 1193-
- [39] J. Su, W. He, X.-M. Li, L. Sun, H.-Y. Wang, Y.-Q. Lan, M. Ding, J.-L. Zuo, Matter 2 (2020) 711-722.
- [40] G.K. Shimizu, J.M. Taylor, S. Kim, Science 341 (2013) 354-355.
- [41] M. Ko, L. Mendecki, K.A. Mirica, Chem. Commun. 54 (2018) 7873–7891.
- [42] W.-H. Li, W.-H. Deng, G.-E. Wang, G. Xu, EnergyChem (2020) 100029.
- [43] G. Xu, G.C. Guo, M.S. Yao, Z.H. Fu, G.E. Wang, Functional linkers for electronconducting MOFs, in: S. Kaskel (Ed.), The Chemistry of Metal-Organic Frameworks: Synthesis, Characterization, and Applications, Wiley-VCH Verlag GmbH & Co. KGaA, Weinheim, 2016, pp. 421-462.
- [44] C.-W. Kung, P.-C. Han, C.-H. Chuang, K.C.-W. Wu, APL Mater. 7 (2019) 110902.
- [45] T. Rodenas, I. Luz, G. Prieto, B. Seoane, H. Miro, A. Corma, F. Kapteijn, F.X.L.I. Xamena, J. Gascon, Nat. Mater. 14 (2015) 48-55
- [46] M. Kalaj, K.C. Bentz, S. Ayala Jr., J.M. Palomba, K.S. Barcus, Y. Katayama, S.M. Cohen, Chem. Rev. (2020), https://doi.org/10.1021/acs.chemrev.1029b00575.
- T. Wu, X. Liu, Y. Liu, M. Cheng, Z. Liu, G. Zeng, B. Shao, Q. Liang, W. Zhang, Q. He, Coord. Chem. Rev. 403 (2020) 213097.
- [48] S. Bi, H. Banda, M. Chen, L. Niu, M. Chen, T. Wu, J. Wang, R. Wang, J. Feng, T. Chen, Nat. Mater. (2020), https://doi.org/10.1038/s41563-41019-40598-

- [49] J. Meng, X. Liu, C. Niu, Q. Pang, J. Li, F. Liu, Z. Liu, L. Mai, Chem. Soc. Rev. (2020), https://doi.org/10.1039/C1039CS00806C
- [50] T.-Y. Huang, C.-W. Kung, Y.-T. Liao, S.-Y. Kao, M. Cheng, T.-H. Chang, J. Henzie, H.R. Alamri, Z.A. Alothman, Y. Yamauchi, K.-C. Ho, K.C.-W. Wu, Adv. Sci. 4 (2017) 1700261.
- [51] N. Hosono, A. Terashima, S. Kusaka, R. Matsuda, S. Kitagawa, Nat. Chem. 11 (2019) 109-116.
- S. Horike, S.S. Nagarkar, T. Ogawa, S. Kitagawa, Angew. Chem. Int. Ed. 59 (2020) 6652-6664.
- [53] N.C. Burtch, J. Heinen, T.D. Bennett, D. Dubbeldam, M.D. Allendorf, Adv. Mater. 30 (2018) 1704124. [54] L. Li, R.-B. Lin, R. Krishna, H. Li, S. Xiang, H. Wu, J. Li, W. Zhou, B. Chen, Science
- 362 (2018) 443-446.
- [55] L.S. Xie, G. Skorupskii, M. Dincă, Chem. Rev. (2020), https://doi.org/10.1021/ acs.chemrev.1029b00766.
- [56] O. Yassine, O. Shekhah, A.H. Assen, Y. Belmabkhout, K.N. Salama, M. Eddaoudi, Angew. Chem. Int. Ed. 55 (2016) 15879–15883.
- [57] H. Yuan, J. Tao, N. Li, A. Karmakar, C. Tang, H. Cai, S.J. Pennycook, N. Singh, D. Zhao, Angew. Chem. Int. Ed. 58 (2019) 14089-14094.
- [58] M.S. Yao, J.W. Xiu, Q.Q. Huang, W.H. Li, W.W. Wu, A.Q. Wu, L.A. Cao, W.H.
- Deng, G.E. Wang, G. Xu, Angew. Chem. Int. Ed. 58 (2019) 14915–14919. [59] Z.-X. Cai, Z.-L. Wang, J. Kim, Y. Yamauchi, Adv. Mater. 31 (2019) 1804903.
- [60] Q. Yang, C.C. Yang, C.H. Lin, H.L. Jiang, Angew. Chem. Int. Ed. 58 (2019) 3511-
- [61] Z. Xiao, J. Meng, Q. Li, X. Wang, M. Huang, Z. Liu, C. Han, L. Mai, Sci. Bull. 63 (2018) 46-53
- [62] J. Hwang, A. Ejsmont, R. Freund, J. Goscianska, B.V. Schmidt, S. Wuttke, Chem. Soc. Rev. (2020), https://doi.org/10.1039/C1039CS00871C.
- S. Dang, Q.-L. Zhu, Q. Xu, Nat. Rev. Mater. 3 (2017) 1-14.
- [64] W. Li, X. Wu, N. Han, J. Chen, X. Qian, Y. Deng, W. Tang, Y. Chen, Sens. Actuators B, Chem. 225 (2016) 158-166.
- S.-J.C. Won-Tae Koo, Sang-Joon Kim, Ji-Soo Jang, Harry L. Tuller, Il-Doo Kim, J. Am. Chem. Soc., 138 (2016) 13431-13437.
- [66] F.Y. Yi, D. Chen, M.K. Wu, L. Han, H.L. Jiang, ChemPlusChem 81 (2016) 675-
- [67] M.G. Campbell, M. Dincă, Sensors 17 (2017), 1108-1108.
- [68] S.R. Batten, N.R. Champness, X.-M. Chen, J. Garcia-Martinez, S. Kitagawa, L. Öhrström, M. O'Keeffe, M.P. Suh, J. Reedijk, Pure Appl. Chem. 85 (2013) 1715-
- [69] C. McDonagh, C.S. Burke, B.D. MacCraith, Chem. Rev. 108 (2008) 400-422.
- [70] O.S. Wolfbeis, Fiber Optic Chemical Sensors and Biosensors, CRC, 1991.
- [71] F.-G. Banica, Chemical Sensors and Biosensors: Fundamentals and Applications, John Wiley & Sons, 2012.
- [72] S. Marco, A. Gutierrez-Galvez, IEEE Sens. J. 12 (2012) 3189-3214.
- [73] G. Sakai, N. Matsunaga, K. Shimanoe, N. Yamazoe, Sens. Actuators B, Chem. 80 (2001) 125-131.
- [74] N. Yamazoe, G. Sakai, K. Shimanoe, Catal. Surv. Asia 7 (2003) 63-75.
- [75] M. Tiemann, Chem.-Eur. J. 13 (2007) 8376-8388.
 [76] B. Hosticka, P. Norris, J. Brenizer, C. Daitch, J. Non-Cryst. Solids 225 (1998) 293-297
- [77] K. Malek, M.-O. Coppens, J. Chem. Phys. 119 (2003) 2801–2811.
- [78] D. Jaguste, S. Bhatia, Chem. Eng. Sci. 50 (1995) 167–182. [79] A. Kahn, Mater. Horiz. 3 (2016) 7–10.
- [80] R.T. Tung, Appl. Phys. Rev. 1 (2014) 011304.
- [81] D.J. Griffiths, C. Inglefield, Introduction to Electrodynamics, fourth ed., Cambridge University Press, 2017.
- [82] J.D. Fowler, M.J. Allen, V.C. Tung, Y. Yang, R.B. Kaner, B.H. Weiller, ACS Nano 3 (2009) 301-306.
- [83] Z. Song, Z. Wei, B. Wang, Z. Luo, S. Xu, W. Zhang, H. Yu, M. Li, Z. Huang, J. Zang, Chem. Mater. 28 (2016).
- [84] Z. Wang, L. Huang, X. Zhu, X. Zhou, L. Chi, Adv. Mater. 29 (2017).
- [85] Y. Jian, W. Hu, Z. Zhao, P. Cheng, H. Haick, M. Yao, W. Wu, Nano-Micro Lett. 12 (2020)71.
- [86] H.-J. Kim, J.-H. Lee, Sens. Actuators B, Chem. 192 (2014) 607–627.
- [87] S.-J. Choi, I.-D. Kim, Electron. Mater. Lett. 14 (2018) 221–260.
- [88] Y. Shimizu, T. Hyodo, M. Egashira, Catal. Surv. Asia 8 (2004) 127-135.
- [89] K. Ihokura, J. Watson, The Stannic Oxide Gas SensorPrinciples and Applications, CRC Press, 2017.
- [90] I. Zemel, Surf. Sci. 86 (1979) 322-334.
- [91] H. Wohltjen, W. Barger, A. Snow, N.L. Jarvis, IEEE Trans. Electron Devices 32 (1985) 1170–1174.
- [92] W. Barger, J. Giuliana, N. Jarvis, A. Snow, H. Wohltjen, J. Environ. Sci. Health Part B 20 (1985) 359-371.
- [93] R. Gutierrez-Osuna, A. Gutierrez-Galvez, N. Powar, Sens. Actuators B, Chem. 93 (2003) 57-66.
- [94] E. Zampetti, S. Pantalei, A. Bearzotti, C. Bongiorno, F. De Cesare, C. Spinella, A. Macagnano, Procedia Eng. 47 (2012) 937-940.
- [95] T. Iwaki, J. Covington, F. Udrea, J. Gardner, Sens. Actuators B, Chem. 141 $(2009)\ 370-380.$ [96] P.J. Hands, P.J. Laughlin, D. Bloor, Sens. Actuators B, Chem. 162 (2012) 400-
- 408. [97] J. Tang, E. Skotadis, S. Stathopoulos, V. Roussi, V. Tsouti, D. Tsoukalas, Sens. Actuators B, Chem. 170 (2012) 129-136.
- [98] X. Gao, F. Li, R. Wang, T. Zhang, Sens. Actuators B, Chem. 258 (2018) 1230-1241.

- [99] M. Blaschke, T. Tille, P. Robertson, S. Mair, U. Weimar, H. Ulmer, IEEE Sens J. 6 (2006) 1298-1308.
- [100] M. Yao, Q. Li, G. Hou, C. Lu, B. Cheng, K. Wu, G. Xu, F. Yuan, F. Ding, Y. Chen, ACS Appl. Mater. Interfaces 7 (2015) 2856-2866.
- [101] I.-S. Hwang, J.-K. Choi, H.-S. Woo, S.-J. Kim, S.-Y. Jung, T.-Y. Seong, I.-D. Kim, J.-H. Lee, ACS Appl. Mater. Interfaces 3 (2011) 3140-3145.
- [102] J.-S. Jang, S.-J. Choi, S.-J. Kim, M. Hakim, I.-D. Kim, Adv. Funct. Mater. 26 (2016) 4740-4748.
- [103] S.-J. Kim, S.-J. Choi, J.-S. Jang, H.-J. Cho, W.-T. Koo, H.L. Tuller, I.-D. Kim, Adv. Mater. 29 (2017) 1700737.
- [104] Y. Xiao, L. Lu, A. Zhang, Y. Zhang, L. Sun, L. Huo, F. Li, ACS Appl. Mater. Interfaces 4 (2012) 3797-3804.
- [105] S.-Y. Cho, H.-J. Koh, H.-W. Yoo, H.-T. Jung, Chem. Mater. 29 (2017) 7197-7205.
- [106] J. Ma, Y. Ren, X. Zhou, L. Liu, Y. Zhu, X. Cheng, P. Xu, X. Li, Y. Deng, D. Zhao, Adv. Funct. Mater. 28 (2018) 1705268.
- [107] Y.J. Hong, J.-W. Yoon, J.-H. Lee, Y.C. Kang, Chem.-Eur. J. 20 (2014) 2737–2741.
- [108] X. Chen, Z. Guo, W.-H. Xu, H.-B. Yao, M.-Q. Li, J.-H. Liu, X.-J. Huang, S.-H. Yu, Adv. Funct. Mater. 21 (2011) 2049-2056.
- [109] G. Lu, L.E. Ocola, J. Chen, Adv. Mater. 21 (2009) 2487-2491.
- [110] L. Guan, S. Wang, W. Gu, J. Zhuang, H. Jin, W. Zhang, T. Zhang, J. Wang, Sens. Actuators B, Chem. 196 (2014) 321-327.
- [111] H. Long, A. Harley-Trochimczyk, T. Pham, Z. Tang, T. Shi, A. Zettl, C. Carraro, M.A. Worsley, R. Maboudian, Adv. Funct. Mater. 26 (2016) 5158-5165.
- [112] S. Deng, V. Tjoa, H.M. Fan, H.R. Tan, D.C. Sayle, M. Olivo, S. Mhaisalkar, J. Wei, C.H. Sow, J. Am. Chem. Soc. 134 (2012) 4905-4917.
- [113] Y. Guo, T. Wang, F. Chen, X. Sun, X. Li, Z. Yu, P. Wan, X. Chen, Nanoscale 8 2016) 12073-12080.
- [114] Z. Wang, L. Huang, X. Zhu, X. Zhou, L. Chi, Adv. Mater. 29 (2017) 1703192.
- [115] A.R. Jalil, H. Chang, V.K. Bandari, P. Robaschik, J. Zhang, P.F. Siles, G. Li, D. Bürger, D. Grimm, X. Liu, G. Salvan, D.R.T. Zahn, F. Zhu, H. Wang, D. Yan, O.G. Schmidt, Adv. Mater. 28 (2016) 2971-2977.
- [116] S. Ji, H. Wang, T. Wang, D. Yan, Adv. Mater. 25 (2013) 1755-1760.
- [117] D.R. Miller, S.A. Akbar, P.A. Morris, Sens. Actuators B, Chem. 204 (2014) 250-272
- [118] F. Shao, M.W.G. Hoffmann, J.D. Prades, R. Zamani, J. Arbiol, J.R. Morante, E. Varechkina, M. Rumyantseva, A. Gaskov, I. Giebelhaus, T. Fischer, S. Mathur, F. Hernández-Ramírez, Sens. Actuators B, Chem. 181 (2013) 130-135.
- [119] J. Wu, K. Tao, Y. Guo, Z. Li, X. Wang, Z. Luo, S. Feng, C. Du, D. Chen, J. Miao, L.K. Norford, Adv. Sci. 4 (2017) 1600319.
- [120] H. Jin, T.-P. Huynh, H. Haick, Nano Lett. 16 (2016) 4194-4202.
- [121] M.W.G. Hoffmann, J. Daniel Prades, L. Mayrhofer, F. Hernandez-Ramirez, T.T. Jaervi, M. Moseler, A. Waag, H. Shen, Adv. Funct. Mater. 24 (2014) 595-602.
- [122] W. Liu, L. Xu, K. Sheng, C. Chen, X. Zhou, B. Dong, X. Bai, S. Zhang, G. Lu, H. Song, J. Mater. Chem. A 6 (2018) 10976–10989.
- [123] Y. Jiang, N. Tang, C. Zhou, Z. Han, H. Qu, X. Duan, Nanoscale 10 (2018) 20578-20586
- [124] B. Esser, J.M. Schnorr, T.M. Swager, Angew. Chem. Int. Ed. 51 (2012) 5752-5756.
- [125] C.O. Park, S.A. Akbar, J. Mater. Sci. 38 (2003) 4611-4637.
- [126] K.D. Schierbaum, U. Weimar, W. Göpel, R. Kowalkowski, Sens. Actuators B, Chem. 3 (1991) 205-214.
- [127] R.W.J. Scott, S.M. Yang, G. Chabanis, N. Coombs, D.E. Williams, G.A. Ozin, Adv. Mater, 13 (2001) 1468-1472.
- [128] R.W.J. Scott, S.M. Yang, N. Coombs, G.A. Ozin, D.E. Williams, Adv. Funct. Mater. 13 (2003) 225-231.
- [129] M. D'Arienzo, L. Ármelao, C.M. Mari, S. Polizzi, R. Ruffo, R. Scotti, F. Morazzoni, I. Am. Chem. Soc. 133 (2011) 5296-5304.
- [130] M. D'Arienzo, L. Armelao, A. Cacciamani, C.M. Mari, S. Polizzi, R. Ruffo, R. Scotti, A. Testino, L. Wahba, F. Morazzoni, Chem. Mater. 22 (2010) 4083-4089.
- [131] J.F. Fennell, S.F. Liu, J.M. Azzarelli, J.G. Weis, S. Rochat, K.A. Mirica, J.B. Ravnsbæk, T.M. Swager, Angew. Chem. Int. Ed. 55 (2016) 1266–1281.
- [132] Y.H. Lee, M. Jang, M.Y. Lee, O.Y. Kweon, J.H. Oh, Chem 3 (2017) 724–763.
- [133] L. Cao, M. Yao, H. Jiang, S. Kitagawa, X. Ye, W.-H. Li, G. Xu, J. Mater. Chem. A (2020), https://doi.org/10.1039/D1030TA01379J.
- [134] W. Ke, X. Qian, Z. Liang, Y. Li, H. Liu, ACS Appl. Mater. Interfaces 5 (2013) 5825-5831.
- [135] C.J. Novotny, E.T. Yu, P.K.L. Yu, Nano Lett. 8 (2008) 775-779.
- [136] L. Guo, Z. Yang, X. Dou, Adv. Mater. 29 (2017) 1604528.
- [137] K. Wang, X. Qian, L. Zhang, Y. Li, H. Liu, ACS Appl. Mater. Interfaces 5 (2013) 5825-5831
- [138] S. Achmann, G. Hagen, J. Kita, I.M. Malkowsky, C. Kiener, R. Moos, Sensors 9 (2009) 1574-1589.
- [139] Z. Sun, S. Yu, L. Zhao, J. Wang, Z. Li, G. Li, Chem.-A, Euro. J. 24 (2018) 10829-10839.
- [140] H.Y. Tan, W.K. Loke, N.-T. Nguyen, S.N. Tan, N.B. Tay, W. Wang, S.H. Ng, Biomed. Microdevices 16 (2014) 269-275.
- [141] C.-Y. Lee, G.-B. Lee, Sens. Lett. 3 (2005) 1-15.
- [142] J. Feng, X. Kang, Q. Zuo, C. Yuan, W. Wang, Y. Zhao, L. Zhu, H. Lu, J. Chen, Sensors 16 (2016) 314.
- [143] P. Davydovskaya, R. Pohle, A. Tawil, M. Fleischer, Sens. Actuators B, Chem. 187 (2013) 142-146.
- [144] E.-X. Chen, H. Yang, J. Zhang, Inorg. Chem. (2014).
- [145] E.-X. Chen, H.-R. Fu, R. Lin, Y.-X. Tan, J. Zhang, ACS Appl. Mater. Interfaces 6 (2014) 22871-22875.

- [146] J.H. Cavka, S. Jakobsen, U. Olsbye, N. Guillou, C. Lamberti, S. Bordiga, K.P. Lillerud, J. Am. Chem. Soc. 130 (2008) 13850-13851.
- [147] M.E. DMello, N.G. Sundaram, A. Singh, A.K. Singh, S.B. Kalidindi, Chem. Commun. 55 (2019) 349-352.
- [148] S. Takaishi, M. Hosoda, T. Kajiwara, H. Miyasaka, M. Yamashita, Y. Nakanishi, Y. Kitagawa, K. Yamaguchi, A. Kobayashi, H. Kitagawa, Inorg. Chem. 48 (2009) 9048-9050.
- [149] M.G. Campbell, S.F. Liu, T.M. Swager, M. Dincă, J. Am. Chem. Soc. 137 (2015) 13780-13783.
- [150] M.K. Smith, K.E. Jensen, P.A. Pivak, K.A. Mirica, Chem. Mater. 28 (2016) 5264-5268
- [151] M.K. Smith, K.A. Mirica, J. Am. Chem. Soc. 139 (2017) 16759-16767.
- [152] K.J. Erickson, F. Leonard, V. Stavila, M.E. Foster, C.D. Spataru, R.E. Jones, B.M. Foley, P.E. Hopkins, M.D. Allendorf, A.A. Talin, Adv. Mater. 27 (2015) 3453-3459
- [153] S. Wang, Q. Wang, X. Feng, B. Wang, L. Yang, Adv. Mater. 29 (2017) 1701898.
- [154] V. Stavila, C. Schneider, C. Mowry, T.R. Zeitler, J.A. Greathouse, A.L. Robinson, J.M. Denning, J. Volponi, K. Leong, W. Quan, M. Tu, R.A. Fischer, M.D. Allendorf, Adv. Funct. Mater. 26 (2016) 1699-1707.
- [155] J.J. Richardson, M. Björnmalm, F. Caruso, Science 348 (2015), aaa2491.
- [156] F.X. Xiao, M. Pagliaro, Y.J. Xu, B. Liu, Chem. Soc. Rev. 45 (2016) 3088-3121.
- [157] A. Betard, R.A. Fischer, Chem. Rev. 112 (2012) 1055-1083.
- [158] B. Hoppe, K.D. Hindricks, D.P. Warwas, H.A. Schulze, A. Mohmeyer, T.J. Pinkvos, S. Zailskas, M.R. Krey, C. Belke, S. König, CrystEngComm 20 (2018) 6458-6471.
- [159] A. Mähringer, A.C. Jakowetz, J.M. Rotter, B.J. Bohn, J.K. Stolarczyk, J. Feldmann, T. Bein, D.D. Medina, ACS Nano 13 (2019) 6711-6719.
- [160] X. Song, X. Wang, Y. Li, C. Zheng, B. Zhang, C.A. Di, F. Li, C. Jin, W. Mi, L. Chen, Angew. Chem. Int. Ed. 59 (2020) 1118-1123.
- [161] L. Heinke, C. Wöll, Adv. Mater. 31 (2019) 1806324.
- [162] M.-S. Yao, X.-J. Lv, Z.-H. Fu, W.-H. Li, W.-H. Deng, G.-D. Wu, G. Xu, Angew. Chem. Int. Ed. 56 (2017) 16510-16514.
- [163] H. Jia, Y. Yao, J. Zhao, Y. Gao, Z. Luo, P. Du, J. Mater. Chem. A 6 (2018) 1188-
- [164] H. Zhong, K.H. Ly, M. Wang, Y. Krupskaya, X. Han, J. Zhang, J. Zhang, V. Kataev, B. Büchner, I.M. Weidinger, Angew. Chem. 131 (2019) 10787-10792.
- [165] J. Liu, Y. Zhou, Z. Xie, Y. Li, Y. Liu, J. Sun, Y. Ma, O. Terasaki, L. Chen, Angew. Chem. Int. Ed. 59 (2019) 1081-1086.
- [166] Z. Meng, A. Aykanat, K.A. Mirica, J. Am. Chem. Soc. 141 (2018) 2046–2053.
- [167] M.L. Aubrey, M.T. Kapelewski, J.F. Melville, J. Oktawiec, D. Presti, L. Gagliardi, J.R. Long, J. Am. Chem. Soc. 141 (2019) 5005-5013.
- [168] M.S. Yao, J.J. Zheng, A.Q. Wu, G. Xu, S.S. Nagarkar, G. Zhang, M. Tsujimoto, S. Sakaki, S. Horike, K. Otake, Angew. Chem. Int. Ed. 59 (2020) 172–176.
- [169] S. Furukawa, K. Hirai, Y. Takashima, K. Nakagawa, M. Kondo, T. Tsuruoka, O. Sakata, S. Kitagawa, Chem. Commun. (2009) 5097–5099.
- [170] S. Furukawa, K. Hirai, K. Nakagawa, Y. Takashima, R. Matsuda, T. Tsuruoka, M. Kondo, R. Haruki, D. Tanaka, H. Sakamoto, Angew, Chem. Int. Ed. 48 (2009) 1766-1770.
- [171] O. Shekhah, H. Wang, D. Zacher, R.A. Fischer, C. Wöll, Angew. Chem. Int. Ed. 48 (2009) 5038-5041.
- [172] D. Zacher, K. Yusenko, A. Bétard, S. Henke, M. Molon, T. Ladnorg, O. Shekhah, B. Schüpbach, M. de los Arcos, M. Krasnopolski, Chem.-A, Euro. J. 17 (2011) 1448-1455
- [173] O. Shekhah, K. Hirai, H. Wang, H. Uehara, M. Kondo, S. Diring, D. Zacher, R.A. Fischer, O. Sakata, S. Kitagawa, S. Furukawa, C. Woll, Dalton Trans. 40 (2011) 4954-4958.
- [174] K. Ikigaki, K. Okada, Y. Tokudome, T. Toyao, P. Falcaro, C.J. Doonan, M. Takahashi, Angew. Chem. Int. Ed. 58 (2019) 6886-6890.
- [175] B. Liu, M. Ma, D. Zacher, A. Bétard, K. Yusenko, N. Metzler-Nolte, C. Wöll, R.A. Fischer, J. Am. Chem. Soc. 133 (2011) 1734–1737. [176] B. Liu, M. Tu, D. Zacher, R.A. Fischer, Adv. Funct. Mater. 23 (2013) 3790–3798.
- [177] V. Chernikova, O. Shekhah, I. Spanopoulos, P.N. Trikalitis, M. Eddaoudi, Chem. Commun. 53 (2017) 6191-6194.
- [178] B. Le Ouay, M. Boudot, T. Kitao, T. Yanagida, S. Kitagawa, T. Uemura, J. Am. Chem. Soc. 138 (2016) 10088-10091.
- [179] G. Férey, C. Mellot-Draznieks, C. Serre, F. Millange, J. Dutour, S. Surblé, I. Margiolaki, Science 309 (2005) 2040-2042.
- [180] I. Strauss, A. Mundstock, M. Treger, K. Lange, S. Hwang, C. Chmelik, P. Rusch, N.C. Bigall, T. Pichler, H. Shiozawa, ACS Appl.Mater. Interfaces 11 (2019) 14175-14181.
- [181] I. Strauss, A. Mundstock, D. Hinrichs, R. Himstedt, A. Knebel, C. Reinhardt, D. Dorfs, J. Caro, Angew. Chem. Int. Ed. 57 (2018) 7434-7439.
- [182] W.-T. Koo, S. Qiao, A.F. Ogata, G. Jha, J.-S. Jang, V.T. Chen, I.-D. Kim, R.M. Penner, ACS Nano 11 (2017) 9276-9285.
- [183] R.C. Hughes, W.K. Schubert, J. Appl. Phys. 71 (1992) 542-544.
- [184] T. Xu, M.P. Zach, Z.L. Xiao, D. Rosenmann, U. Welp, W.K. Kwok, G.W. Crabtree, Appl. Phys. Lett. 86 (2005) 203104.
- [185] L.G. Villanueva, F. Fargier, T. Kiefer, M. Ramonda, J. Brugger, F. Favier, Nanoscale 4 (2012) 1964-1967.
- [186] F. Favier, E.C. Walter, M.P. Zach, T. Benter, R.M. Penner, Science 293 (2001) 2227-2231.
- [187] M.A. Lim, D.H. Kim, C.-O. Park, Y.W. Lee, S.W. Han, Z. Li, R.S. Williams, I. Park, ACS Nano 6 (2012) 598-608.
- [188] Q. Zhao, J. Shao, H. Tian, X. Li, C. Wang, J. Liu, Sens. Actuators B, Chem. 270 (2018) 475-481.
- [189] R.A. Potyrailo, Chem. Rev. 116 (2016) (1923) 11877-11923.

- [190] K.S. Park, Z. Ni, A.P. Côté, J.Y. Choi, R. Huang, F.J. Uribe-Romo, H.K. Chae, M. O'Keeffe, O.M. Yaghi, Proc. Natl. Acad. Sci. 103 (2006) 10186–10191.
- [191] X.C. Huang, Y.Y. Lin, J.P. Zhang, X.M. Chen, Angew. Chem. Int. Ed. 45 (2006) 1557–1559.
- [192] M.S. Yao, W.X. Tang, G.E. Wang, B. Nath, G. Xu, Adv. Mater. 28 (2016) 5229–5234.
- [193] K. Zhang, R.P. Lively, C. Zhang, R.R. Chance, W.J. Koros, D.S. Sholl, S. Nair, J. Phys. Chem. Lett. 4 (2013) 3618–3622.
- [194] W.T. Koo, S.J. Kim, J.S. Jang, D.H. Kim, I.D. Kim, Adv. Sci. 6 (2019) 1900250.
- [195] D. Wang, Z. Li, J. Zhou, H. Fang, X. He, P. Jena, J.-B. Zeng, W.-N. Wang, Nano-Micro Lett. 10 (2018) 4.
- [196] P. Li, H. Zhan, S. Tian, J. Wang, X. Wang, Z. Zhu, J. Dai, Y. Dai, Z. Wang, C. Zhang, ACS Appl. Mater. Interfaces 11 (2019) 13624–13631.
- [197] N. Jafari, S. Zeinali, J. Shadmehr, J. Mater. Sci.: Mater. Electron. 30 (2019) 12339–12350.
- [198] S.S.-Y. Chui, S.M.-F. Lo, J.P. Charmant, A.G. Orpen, I.D. Williams, Science 283 (1999) 1148–1150.
- [199] N.A. Travlou, K. Singh, E. Rodríguez-Castellón, T.J. Bandosz, J. Mater. Chem. A 3 (2015) 11417–11429.
- [200] J. Wu, J. Chen, C. Wang, Y. Zhou, K. Ba, H. Xu, W. Bao, X. Xu, A. Carlsson, S. Lazar, A. Meingast, Z. Sun, H. Deng, Adv. Sci. (2020), https://doi.org/10.1002/advs.201903003.
- [201] H. Tian, H. Fan, M. Li, L. Ma, ACS Sens. 1 (2016) 243-250.
- [202] M. Drobek, J.-H. Kim, M. Bechelany, C. Vallicari, A. Julbe, S.S. Kim, ACS Appl. Mater. Interfaces 8 (2016) 8323–8328.
- [203] X. Wu, S. Xiong, Z. Mao, S. Hu, X. Long, Chem.-Eur. J. 23 (2017) 7969-7975.
- [204] T. Zhou, Y. Sang, Y. Sun, C. Wu, X. Wang, X. Tang, T. Zhang, H. Wang, C. Xie, D. Zeng, Langmuir 35 (2019) 3248–3255.
- [205] M.-S. Yao, L.-A. Cao, Y.-X. Tang, G.-E. Wang, R.-H. Liu, P.N. Kumar, G.-D. Wu, W.-H. Deng, W.-J. Hong, G. Xu, J. Mater. Chem. A 7 (2019) 18397–18403.
- [206] T. Zhou, Y. Sang, X. Wang, C. Wu, D. Zeng, C. Xie, Sens. Actuators B, Chem. 258 (2018) 1099–1106.
- [207] S.S. Nair, N. Illyaskutty, B. Tam, A.O. Yazaydin, K. Emmerich, A. Steudel, T. Hashem, L. Schöttner, C. Wöll, H. Kohler, Sens. Actuators B, Chem. 304 (2020).
- [208] X. Wu, S. Xiong, Y. Gong, Y. Gong, W. Wu, Z. Mao, Q. Liu, S. Hu, X. Long, Sens. Actuators B, Chem. 292 (2019) 32–39.
- [209] L. Zhang, P. Cui, H. Yang, J. Chen, F. Xiao, Y. Guo, Y. Liu, W. Zhang, F. Huo, B. Liu, Adv. Sci. 3 (2016) 1500243.
- [210] P. Wang, X. Zou, H. Tan, S. Wu, L. Jiang, G. Zhu, J. Mater. Chem. C 6 (2018) 5412–5419.
- [211] Y. Lu, W. Zhan, Y. He, Y. Wang, X. Kong, Q. Kuang, Z. Xie, L. Zheng, ACS Appl. Mater. Interfaces 6 (2014) 4186–4195.
- [212] Y.-M. Jo, T.-H. Kim, C.-S. Lee, K. Lim, C.W. Na, F. Abdel-Hady, A.A. Wazzan, J.-H. Lee, ACS Appl. Mater. Interfaces 10 (2018) 8860–8868.
- [213] Y. Wang, Y. Lü, W. Zhan, Z. Xie, Q. Kuang, L. Zheng, J. Mater. Chem. A 3 (2015) 12796–12803.
- [214] J.-S. Jang, W.-T. Koo, S.-J. Choi, I.-D. Kim, J. Am. Chem. Soc. 139 (2017) 11868–11876.
- [215] H. Yuan, S.A.A. Aljneibi, J. Yuan, Y. Wang, H. Liu, J. Fang, C. Tang, X. Yan, H. Cai, Y. Gu, S.J. Pennycook, J. Tao, D. Zhao, Adv. Mater. 31 (2019) 1807161.
- [216] T. Zhou, S. Cao, R. Zhang, T. Fei, T. Zhang, Inorg. Chem. Front. 6 (2019) 3177–3183.
- [217] Y. Xiong, W. Xu, Z. Zhu, Q. Xue, W. Lu, D. Ding, L. Zhu, Sens. Actuators B, Chem. 253 (2017) 523–532.
- [218] S. Shi, F. Zhang, H. Lin, Q. Wang, E. Shi, F. Qu, Sens. Actuators B, Chem. 262 (2018) 739–749.
- [219] N. Zhang, S. Ruan, Y. Yin, F. Li, S. Wen, Y. Chen, ACS Appl. Nano Mater. 1 (2018) 4671–4681.
- [220] Y. Li, K. Li, Y. Luo, B. Liu, H. Wang, L. Gao, G. Duan, Sens. Actuators B, Chem. (2020) 127657.
- [221] X.F. Wang, K.M. Sun, S.J. Li, X.Z. Song, L. Cheng, W. Ma, ChemistrySelect 3 (2018) 12871–12877.
- [222] Y.-Y. Xue, J.-L. Wang, S.-N. Li, Y.-C. Jiang, M.-C. Hu, Q.-G. Zhai, J. Solid State
- Chem. 251 (2017) 170–175. [223] H.-F. Wang, L. Chen, H. Pang, S. Kaskel, Q. Xu, Chem. Soc. Rev. 49 (2020) 1414–1448.
- [224] C. Wang, J. Kim, J. Tang, M. Kim, H. Lim, V. Malgras, J. You, Q. Xu, J. Li, Y. Yamauchi, Chem 6 (2020) 19–40.
- [225] Q. Wang, D. Astruc, Chem. Rev. 120 (2020) 1438–1511.
- [226] Q. Li, J. Wu, L. Huang, J. Gao, H. Zhou, Y. Shi, Q. Pan, G. Zhang, Y. Du, W. Liang, J. Mater. Chem. A 6 (2018) 12115–12124.
- [227] W.T. Koo, J.H. Cha, J.W. Jung, S.J. Choi, J.S. Jang, D.H. Kim, I.D. Kim, Adv. Funct. Mater. 28 (2018) 1802575.
- [228] I. Stassen, B. Bueken, H. Reinsch, J. Oudenhoven, D. Wouters, J. Hajek, V. Van Speybroeck, N. Stock, P. Vereecken, R. Van Schaijk, Chem. Sci. 7 (2016) 5827– 5832.
- [229] Z.-G. Gu, S.-C. Chen, W.-Q. Fu, Q. Zheng, J. Zhang, ACS Appl. Mater. Interfaces 9 (2017) 7259–7264.
- [230] Z. Iskierko, P.S. Sharma, D. Prochowicz, K. Fronc, F. D'Souza, D. Toczydłowska, F. Stefaniak, K. Noworyta, ACS Appl. Mater. Interfaces 8 (2016) 19860–19865.
- [231] S.G. Surya, S.S. Nagarkar, S.K. Ghosh, P. Sonar, V.R. Rao, Sens. Actuators B, Chem. 223 (2016) 114–122.

- [232] S. Yuvaraja, S.G. Surya, V. Chernikova, M.T. Vijjapu, O. Shekhah, P.M. Bhatt, S. Chandra, M. Eddaoudi, K.N. Salama, ACS Appl. Mater. Interfaces (2020), https://doi.org/10.1021/acsami.1020c00803.
- [233] G. Wu, J. Huang, Y. Zang, J. He, G. Xu, J. Am. Chem. Soc. 139 (2016) 1360–1363.
- [234] M.L. Aubrey, B.M. Wiers, S.C. Andrews, T. Sakurai, S.E. Reyes-Lillo, S.M. Hamed, C.-J. Yu, L.E. Darago, J.A. Mason, J.-O. Baeg, Nat. Mater. 17 (2018) 625–632.
- [235] B. Wang, Y. Luo, B. Liu, G. Duan, ACS Appl. Mater. Interfaces 11 (2019) 35935–35940.
- [236] S. Roopak, A. Ji, P.K. Parashar, R. Sharma, J. Phys. D Appl. Phys. 50 (2017) 335105.
- [237] V. Rubio-Giménez, M. Galbiati, J. Castells-Gil, N. Almora-Barrios, J. Navarro-Sánchez, G. Escorcia-Ariza, M. Mattera, T. Arnold, J. Rawle, S. Tatay, Adv. Mater. 30 (2018) 1704291.
- [238] D. Acker, R. Harder, W. Hertler, W. Mahler, L. Melby, R.E. Benson, W. Mochel, J. Am. Chem. Soc. 82 (1960) 6408-6409.
- [239] L. Melby, R. Harder, W. Hertler, W. Mahler, R. Benson, W. Mochel, J. Am. Chem. Soc. 84 (1962) 3374–3387.
- [240] L. Shields, J. Chem. Soc., Faraday Trans. 2 81 (1985) 1-9.
- [241] F. Hoshyargar, M. Shafiei, C. Piloto, N. Motta, A.P. O'Mullane, J. Mater. Chem. C 4 (2016) 11173–11179.
- [242] D. Chadi, P. Citrin, C. Park, D. Adler, M. Marcus, H.-J. Gossmann, Phys. Rev. Lett. 79 (1997) 4834.
- [243] A. Dimoulas, P. Tsipas, A. Sotiropoulos, E. Evangelou, Appl. Phys. Lett. 89 (2006) 252110.
- [244] H. Yu, M. Schaekers, T. Schram, S. Demuynck, N. Horiguchi, K. Barla, N. Collaert, A.V.-Y. Thean, K. De Meyer, IEEE Trans. Electron. Devices 63 (2016) 2671–2676.
- [245] D. Xiang, C. Han, Z. Hu, B. Lei, Y. Liu, L. Wang, W.P. Hu, W. Chen, Small 11 (2015) 4829–4836.
- [246] C. Xie, X. Zhang, Y. Wu, X. Zhang, X. Zhang, Y. Wang, W. Zhang, P. Gao, Y. Han, J. Jie, J. Mater. Chem. A 1 (2013) 8567–8574.
- [247] K. Ding, X. Zhang, F. Xia, R. Wang, Y. Kuang, S. Duhm, J. Jie, X. Zhang, J. Mater. Chem. A 5 (2017) 285–291.
- [248] X. Li, H. Zhu, K. Wang, A. Cao, J. Wei, C. Li, Y. Jia, Z. Li, X. Li, D. Wu, Adv. Mater. 22 (2010) 2743–2748.
- [249] W. Chen, C. Yang, S. Yu, Z. Li, G. Li, Polyhedron 158 (2019) 377-385.
- [250] K. Guo, L. Zhao, S. Yu, W. Zhou, Z. Li, G. Li, Inorg. Chem. 57 (2018) 7104–7112.
- [251] R. Liu, Y. Liu, S. Yu, C. Yang, Z. Li, G. Li, ACS Appl. Mater. Interfaces 11 (2018) 1713–1722.
- [252] J.J. Gassensmith, J.Y. Kim, J.M. Holcroft, O.K. Farha, J.F. Stoddart, J.T. Hupp, N.C. Jeong, J. Am. Chem. Soc. 136 (2014) 8277–8282.
- [253] Y. Lu, S. Zhang, S. Dai, D. Liu, X. Wang, W. Tang, X. Guo, J. Duan, W. Luo, B. Yang, J. Zou, Y. Huang, H.E. Katz, J. Huang, Matter (2020), https://doi.org/10.1016/j.matt.2020.05.021.
- [254] L. Xiao, R. Xu, Q. Yuan, F. Wang, Talanta 167 (2017) 39-43.
- [255] M. Wang, Y. Liu, L. Yang, K. Tian, L. He, Z. Zhang, Q. Jia, Y. Song, S. Fang, Sens. Actuators B, Chem. 281 (2019) 1063–1072.
- [256] C. Sapsanis, H. Omran, V. Chernikova, O. Shekhah, Y. Belmabkhout, U. Buttner, M. Eddaoudi, K.N. Salama, Sensors 15 (2015) 18153–18166.
- [257] M. Hosseini, S. Zeinali, M. Sheikhi, Sens. Actuators B, Chem. 230 (2016) 9–16.
- [258] S. Homayoonnia, S. Zeinali, Sens. Actuators B, Chem. 237 (2016) 776–786. [259] V. Chernikova, O. Yassine, O. Shekhah, M. Eddaoudi, K.N. Salama, J. Mater.
- [259] V. Chernikova, O. Yassine, O. Shekhah, M. Eddaoudi, K.N. Salama, J. Mater Chem. A 6 (2018) 5550–5554.
- [260] S.G. Surya, S. Bhanoth, S.M. Majhi, Y.D. More, V.M. Teja, K.N. Chappanda, CrystEngComm 21 (2019) 7303–7312.
- [261] S. Sachdeva, D. Soccol, D.J. Gravesteijn, F. Kapteijn, E.J. Sudhölter, J. Gascon, L. C. de Smet, ACS Sens. 1 (2016) 1188–1192.
- [262] A.H. Assen, O. Yassine, O. Shekhah, M. Eddaoudi, K.N. Salama, ACS Sens. 2 (2017) 1294–1301.
- [263] M.A. Andrés, M.T. Vijjapu, S.G. Surya, O. Shekhah, K.N. Salama, C. Serre, M. Eddaoudi, O. Roubeau, I. Gascón, ACS Appl. Mater. Interfaces 12 (2020) 4155–4162.
- [264] M. Shafiei, F. Hoshyargar, J. Lipton-Duffin, C. Piloto, N. Motta, A.P. O'Mullane, J. Phys. Chem. C 119 (2015) 22208–22216.
- [265] M. Hmadeh, Z. Lu, Z. Liu, F. Gándara, H. Furukawa, S. Wan, V. Augustyn, R. Chang, L. Liao, F. Zhou, E. Perre, V. Ozolins, K. Suenaga, X. Duan, B. Dunn, Y. Yamamto, O. Terasaki, O.M. Yaghi, Chem. Mater. 24 (2012) 3511–3513.
- [266] M. Ko, A. Aykanat, M.K. Smith, K.A. Mirica, Sensors 17 (2017) 2192.
- [267] M. Wang, Z. Shen, X. Zhao, F. Duanmu, H. Yu, H. Ji, J. Hazard. Mater. 371 (2019) 352–361.
- [268] R. Zhang, T. Zhou, L. Wang, T. Zhang, ACS Appl. Mater. Interfaces 10 (2018) 9765–9773.
- [269] W. Zhou, Y.-P. Wu, J. Zhao, W.-W. Dong, X.-Q. Qiao, D.-F. Hou, X. Bu, D.-S. Li, Inorg. Chem. 56 (2017) 14111–14117.
- [270] K. Tao, X. Han, Q. Yin, D. Wang, L. Han, L. Chen, ChemistrySelect 2 (2017) 10918–10925.
- [271] W.-T. Koo, S. Yu, S.-J. Choi, J.-S. Jang, J.Y. Cheong, I.-D. Kim, ACS Appl. Mater. Interfaces 9 (2017) 8201–8210.
- [272] S.-J. Choi, H.-J. Choi, W.-T. Koo, D. Huh, H. Lee, I.-D. Kim, ACS Appl. Mater. Interfaces 9 (2017) 40593–40603.

[273] S. Zeinali, S. Homayoonnia, G. Homayoonnia, Sens. Actuators B, Chem. 278 (2019) 153–164.



Ming-Shui Yao received his Ph.D. in Materials Science (2014) supervised by Prof. Fangli Yuan from Institute of Process Engineering, CAS. Then he worked in Prof. Gang Xu's group (2014-2018) at Fujian Institute of Research on the Structure of Matter, CAS. He is now a Japan Society for the Promotion of Science (JSPS) fellow in WPI-iCeMS, Kyoto University supervised by Prof. Susumu Kitagawa. His major field is low temperature and highly selective gas sensors based on porous crystalline materials.



Gang Xu received his Ph.D. in 2008 at FJIRSM, CAS. Then he worked as postdoctoral fellows at COSDAF in City University of Hong Kong (Hong Kong), University of Regensburg (Alexander von Humboldt fellowship, Germany) and Kyoto University (JSPS fellowship, Japan) in sequence. In 2013, he joined FJIRSM and undertook his independent research as a Pl. His research interests focus on the conductive coordination polymers and their related electrical devices.



Wen-Hua Li earned his Ph.D. in 2019 from Fujian Institute of Research on the Structure of Matter (FJIRSM), Chinese Academy of Sciences, University of Chinese Academy of Sciences, Beijing. He is currently a postdoc under the guidance of Prof. Gang Xu at FJIRSM. His research work is focused on the development of conductive MOF-based multifunctional materials.